METAMATERIAL ANTENNA DESIGN
FOR 5.8 GHz DOPPLER RADAR

A Thesis Submitted to
the Graduate School of Engineering and Sciences of
İzmir Institute of Technology
in Partial Fulfillment of the Requirements for the Degree of

MASTER OF SCIENCE

in Electronics and Communication Engineering

by
Hasan Önder YILMAZ

December 2018
İZMİR

We approve the thesis of **Hasan Önder YILMAZ**

Examining Committee Members:

_____
Assist. Prof. Dr. Fatih YAMAN
Department of Electrical and Electronics Engineering
İzmir Institute of Technology

_____
Prof. Dr. Alp KUŞTEPELİ
Department of Electrical and Electronics Engineering
İzmir Institute of Technology

_____
Assoc. Prof. Dr. Mustafa SEÇMEN
Department of Electrical and Electronics Engineering
Yaşar University

20 December 2018

_____
Assist. Prof. Dr. Fatih YAMAN
Supervisor, Department of Electrical and Electronics Engineering
İzmir Institute of Technology

_____   _____
Prof. Dr. Enver TATLICIOĞLU   **Prof. Dr. Aysun SOFUOĞLU**
Head of the Department of   Dean of the Graduate School of
Electrical and Electronics Engineering   Engineering and Sciences

ACKNOWLEDGMENTS

ABSTRACT

METAMATERIAL ANTENNA DESIGN
FOR 5.8 GHz DOPPLER RADAR

This thesis presents mainly simulation and measurement results of metamaterial based transmitter and receiver antennas for a Doppler radar system operating at 5.8 GHz and indoor, outdoor and through-wall performances of the Doppler radar system after the integration of field and the realized transmitter and receiver antennas. Firstly, the antennas are modeled via 3D electromagnetic simulation program CST:Microwave Studio and related parameters are calculated. Afterwards, in order to observe antenna performances, radiation pattern and gain characteristics of realized antennas are measured in laboratory environment including anechoic chamber. Another essential objective of this thesis is to examine and analyze applicability and effectiveness of the metamaterial based antennas for a 5.8 GHz Doppler radar system. For this reason, a double negative index metamaterial structure is integrated to a patch antenna for the transmitter. For the receiver antenna, a near-zero index medium is designed to locate over patch antenna. Accordingly, significant improvements in size and bandwidth for the transmitter and in gain and directivity for the receiver in addition to improvement of its psychical size are obtained. It is shown that return loss, radiation pattern and gain measurement results of the designed antennas agree well with the simulations for a desired frequency band. According to the experimental data, the realized transmitter antenna has a higher directivity value as compared to the simulated one, therefore it radiates most of the power into narrower area. Additionally, the measured one has a wider bandwidth. The measurement results of receiver antenna are consistent with simulation in terms of bandwidth, return-loss, radiation pattern of horizontal direction and gain value.

The last part of the thesis is devoted to expressing the application of the designed antennas to the low-power, short-range Doppler radar system, which is designed to detect the speed of the human or moving target in the indoor/outdoor environment or behind the wall. Improvements on the performance of the radar system integrated with metamaterial antennas are discussed and performances results are commented.

ÖZET

5.8 GHz DOPPLER RADARI İÇİN META-MALZEME ANTEN TASARIMI

Bu tez çalışması esas olarak 5.8 GHz Doppler radar sistemi için tasarlanmış metamalzeme tabanlı verici ve alıcı antenlerin simülasyon ve ölçüm sonuçları ile üretilmiş antenlerin sisteme entegre edilmiş haliyle, iç/dış ortam ve duvar arkası radar performans analizlerini içermektedir. Öncelikle antenler üç boyutlu elektromagnetik benzetim programı olan CST:Microwave Studio ile modellenmiş ve ilgili alan ve parametreler hesaplanmıştır. Ardından, gerçeklenen antenlerin, performanslarını gözlemlemek amacıyla kullanılan yankısız odada ışıma paterni ve kazanç ölçümleri yapılmıştır. Bu tezin hedeflerinden bir diğeri ise metamalzeme tabanlı antenlerin 5.8 GHz Doppler radar sistemine uygulanabilirliğini ve verimliliğini araştırmaktır. Bu nedenle, verici anten için çift negatif indeksli metamalzeme yapısı yama antene entegre edilmiştir. Alıcı anten için ise, yama anten üzerine yerleştirilmek üzere sıfıra yakın indeksli metamalzeme plaka tasarlanmıştır. Bu sayede, verici anten için fiziksel boyut kısmında ve verimliliğinde, alıcı anten için ise fiziksel boyutunun yanı sıra anten kazancında ve yönelticilik değerinde kayda değer gelişmeler sağlanmıştır. Yenilikle tasarlanan antenlerin hedeflenen frekanslardaki, yansıma kaybı, ışıma paterni ve kazanç ölçüm sonuçlara göre, simülasyon ile ölçüm verileri arasında iyi bir uyum olduğu gözlemlenmektedir. Elde edilen deneysel bulgulara göre, gerçeklenen verici anten benzetim ortamında tasarlanan yapıya göre daha fazla yönelticilik değerine sahiptir, dolayısıyla gücünün çoğunu daha dar bir açıda ortama yayar. Ayrıca daha büyük bir bant genişliğine sahiptir. Alıcı anten için ise bant genişliği, yansıma kaybı, yatay polarizasyon yayılım grafiği ve anten kazancı değerleri benzetim sonuçları ile uyumludur.

Tezin son kısmı tasarlanan antenlerin, insan veya hareketli herhangi bir hedefin iç/dış çevredeki veya duvarın arkasındaki hızını tespit etmek amacıyla oluşturulan düşük güçlü, kısa mesafe Doppler radar sistemine uygulanmasını ifade etmek için ayrılmıştır. Metamalzeme antenlerle entegre edilmiş radar sisteminin performans iyileştirmeleri tartışılmış ve performans sonuçları yorumlanmıştır.

TABLE OF CONTENTS

LIST OF FIGURES

x

LIST OF TABLES

LIST OF ABBREVIATIONS

SRR . . . . Split Ring Resonator

CSRR . . . . Complemantary Split Ring Resonator

VSWR . . . . Voltage Standing Wave Ratio

CST-MWS . . . . Computer Simulation Technology Microwave Studio

VNA . . . . Vector Network Analyzer

SMA . . . . Sub-miniature Version A

CW . . . . Continious Wave

FMCW . . . . Frequency Modulated Continious Wave

SNG . . . . single Negative Material

DNG . . . . Double Megative Medium

LHM . . . . Left-Handed Medium

RHM . . . . Right-Handed Medium

CRLM . . . . Composite of Right and Left Handed Medium

ENG . . . . Epsilon Negative Material

MNG . . . . Mu Negative Material

ENZ . . . . Epsilon Near-Zero

ZIM . . . . Zero-Index Material

ISM . . . . Industrial Scientific Medical

CHAPTER 1

INTRODUCTION

Metamaterials can be described as artificially designed structures, which provide preternatural values of constitutive parameters such as negative effective permeability and permittivity. This novel concept of physic is raised attention for optical, tera-hertz and microwave engineering applications in the last decade. Namely "metamaterial" describes the medium properties, those can not be observed in nature, for electromagnetic field and wave theory. Although first experimental studies were presented at the beginning of 20th century such as geometrically twisted structures media by Jagadis Chunder Bose and randomly oriented small wire helices in a host medium by Lindman those can be considered as examples of chiral medium (Nader Engheta, 2006). The existence of left-handed or in other name simultaneously double negative medium is explained by Veselago in theoretically his guiding study, (Veselago, 1968). Almost thirty years later, it has been proven that arranging metallic wires along the propagation of wave can provide negative effective permittivity (J. B. Pendry and Youngs, 1996). After a short time, another fascinating study demonstrated that properly designed highly conducting split rings with its lateral plane along the direction of propagation show negative effective permeability (J. B. Pendry and Stewart, 1999). It should be noted that even though negative permittivity exists in nature (ferro-electrics material and plasma), it is assumed that the negative permeability is very seldomly seen in nature such as ferro-magnetic materials. A remarkable study, see (D. R. Smith and Schultz, 2000), on metamaterials clarifies the attitude of double negative (left-handed) medium where effective permittivity and permeability are negative at a specific spectrum, give rise to lots of metamaterials related applied survey and progress of novel sensors, filters, resonators, guiding structures and antennas in microwave region, see (Lijuan Su and Martin, 2016, Ali and Hu, 2008, Withayachumnankul and Abbott, 2009, Amir Ebrahimi and Abbott, 2014). In recent years, the researchers of this area are widely spread to different types of applications in various fields from microwaves, tera-hertz engineering up to optical spectrum and even mechanics. This thesis mainly focused on microwave antenna designs which are topics of double negative material and near-zero index/epsilon metamaterial. Particularly, novel antenna designs based on metamaterials hold important roles in practice due to unexpected significant enchantments in the antenna parameters. Adjustable very low plasma frequency in the restricted region

of dielectric-conductor boundary, presented in study by Pendry et al. see, (J. B. Pendry and Youngs, 1996), can give a start to break some limitations which leads a wide area to investigate for engineers and physicists. After the year of 2000, when metamaterial concept is introduced, many antenna studies have been presented so far. For example, Enoch et al. obtained a medium owning near-zero refractive index having a very-low plasma frequency, such that it can reshape the radiated beam from source, see (Stefan Enoch and Vincent, 2002). Studies (Stefan Enoch and Vincent, 2002 - Turpin and et al., 2012 and Davide Ramaccia and Daly, 2013) use metamaterial epsilon near-zero (ENZ) structure to concentrate the radiated energy into a narrow angle under certain necessary conditions. Moreover, Liu et al. (Yahong Liu and Zhao, 2013) showed that when zero-index material (ZIM) is placed over typical patch antennas, it makes antenna's beam-width highly narrower and herewith its directivity much higher. The study by Lie et al. demonstrated left-handed (double-negative medium) characteristics on planar surface, (Le-Wei Li and Martin, 2010), and it is shown that such a left-handed medium has significant effects on the improvements of antenna performance in terms of wide bandwidth, high efficiency, low-losses and low voltage standing wave ratio (VSWR). Studies related bandwidth enhancement, see (Zhu and Eleftheriades, 2009) and (Merih Palandoken and Henke, 2009), use the left-handed metamaterials for two dimensional planar antennas. Sungjoon Lim et al. composed right-handed and left-handed (CRLH) microstrip structure to construct novel leaky-wave antenna with metamaterial based transmission line and electronically tunable radiation angle. (Sungjoon Lim and Itoh, 2005). Another study by Ziolkowski et al. presented inexpensive compact two-dimensional and three-dimensional electrically small antennas includes electrically small parasitic object suitable type of metamaterial, (Erentok and Ziolkowski, 2008). It is should be noted that, initial results of this thesis are presented in conference, see (Önder Yılmaz and Yaman, 2018b), and also submitted to scientific journal, see (Önder Yılmaz and Yaman, 2018a). In addition to these, in the Turkish literature, there are a few published theses about metamaterial and its applications. In (Sondaş, 2011), tunable single band microstrip antenna supported by split ring resonator is presented. In another thesis, see (Karaaslan, 2009), omega shape resonator structures are used to obtain near-zero index layers which are placed over microstrip antenna with enhanced bandwidth by using slotted technique. Realization of negative refractive index metamaterials is investigated in (Mali, 2012).

Another fascinating concept, photonic band gap structures which are recently have been come up, now are classified under the broad terminology of "electromagnetic band gap (EBG)" structures. These artificial periodic structures prohibit or support the propa-

gation of electromagnetic waves in specified band of frequency for all incident angle and all polarization states, (Yang and Rahmat-Samii, 2009). Electromagnetic band gap structures can be considered as a particular type of metamaterial excluding dimension ratio between unit cell and wavelength of excitation wave. Novel properties of these structures widens the application areas of engineers and scientist from optical and terahertz regions research to microwave, solid-state and plasma physics. Properly designed photonic crystals can prohibit the propagation of electromagnetic wave, or allow it to propagate only in certain direction. They can be designed in one, two and three dimensions with either dielectric or/and metallic materials, see (Nader Engheta, 2006) This unique feature allow us to design highly directive small antennas in microwave range on a two dimensional plane efficiently.

Development of radar systems is a well-known application area of electromagnetic field and wave theories for RF and microwave engineers. Among different types of radars systems according to their aims, small and lightweight short-range Doppler radar systems are capable of detect targets in motion with low power consumption in many different environments such as outdoor, indoor and through-wall applications, see (Charvat, 2014). Small and short range radar systems are used in traffic, military, through-wall vital sign recognition, missile guidance and autonomous devices, see Figure-1.1, (Shanyue Guan and Gu, 2014, Munoz-Ferreras and et al., 2016, Hosseini and Amindavar, 2017, Zhao and Su, 2018).
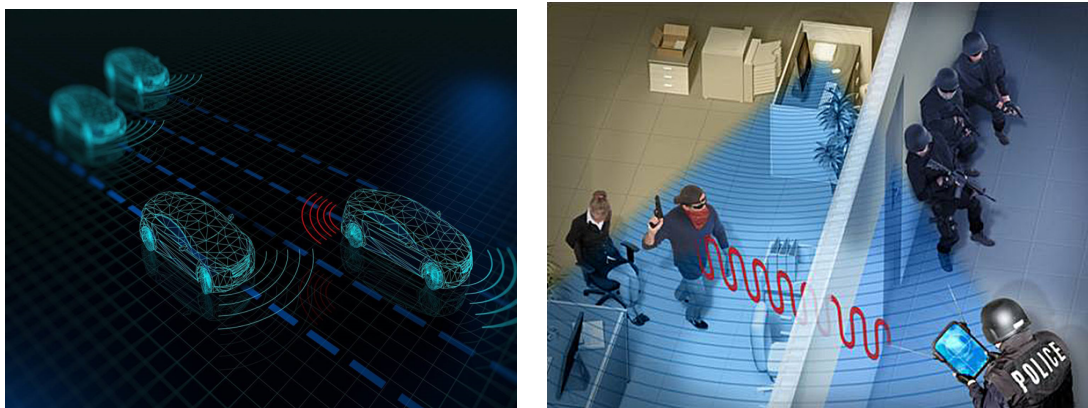
Figure 1.1. Examples for short-range Doppler radar engineering application. Autonomus car (left) and through-wall scenario (right) (Source: spectrum.ieee.org, 2018 and thedrive.com, 2018)

Herewith, in this thesis metamaterial based antennas integrated to a bi-static compact radar system in order to improve radar system size, weight, range and efficiency

at 5.8 GHz, is proposed. Maximum radar range such that the information carrier signal and the background noise can not be distinguished anymore, can be calculated by using Friis transmission equation. Accordingly, maximum range can be increased by improving gains and efficiency of both transmitter and receiver antennas. (Balanis, 2005). In this way, improvements on antennas should be taken into account. However, well-known and generally preferred microstrip antennas for such a small and compact systems, have particular disadvantages. First examples come to mind might be those, to enhance the directivity, one has to increase the number of patches in the microstrip array antenna or, to acquire high gain one has to increase the height of the dielectric substrate (R.Garg and A.Ittipiboon, 2001). These necessities cause unwieldy of the system and give rise to extra power losses on antenna, in particular case of microstrip arrays.

In the following section, small and short range Doppler radar systems are introduced as an application platform for metamaterial antennas, which are proposed in this thesis. Then, some improvements on the system are discussed. Proposed radar system design and signal processing briefly are given in next sections. Main motivation and objectives of thesis are mentioned and listed in last section of the first chapter.

1.1. Short Range Radar Systems

Radar namely means to "radio direction and ranging" is a World War II acronym, (Watson, 2009). A radar system mainly includes transmitter and receiver sections where the electromagnetic wave is radiated from transmitter antenna, then scattered wave from target is collected by receiver with the information of medium and electromagnetic wave properties affected by target, such as speed of wave, shifted frequency components and the delayed round-trip time, etc. These parameters carry informations about target, range, velocity, size, material property and other various demanded parameters. So that, while designing the whole system, these desired parameters are considered. In this thesis, small, low powered, short-range Doppler radar system is studied and formed as well as considering the performing parameters of environment and target are specified. The most important components of the transmitter and receiver stages in our system are expected to be the antennas which basically classify the radar system . One type of classification method is listed according to the placement of antennas or their usage, see (Jenn, 2018);

- **Bi-static:** The transmitter and receiver antennas are positioned at distinct locations when it is viewed from the target. For example; ground transmitter and air-bone

receiver.

- **Mono-static:** The transmitter and receiver are at the same location when it is viewed from the target. Same antennas usage for transmitter and receiver sequentially with pulsed signal is the example for mono-static type.

- **Quasi-Mono-static:** The transmitter and receiver antennas are slightly isolated from each other but still appear to be at same environment when it is observed from the target location. Simple illustration given in Figure-1.2 where the target is positioned at far enough to the system.
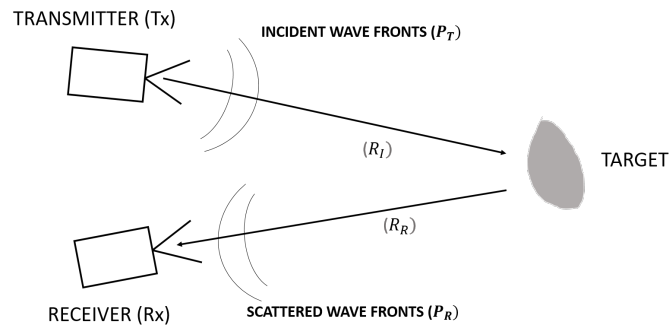
Figure 1.2. Simple quasi-mono-static radar illustration

Two different types of metamaterial based antennas are designed based on knowledge of the recent studies on double negative index transmitter (Tx) and near-zero index receiver (Rx) concepts by considering system restrictions and requirements for the transmitter and receiver stages. Thereafter, they put into practice as a quasi-monostatic radar system which means two antennas are required for each transmitter and receiver part and system is constructed on same board regarding enough decoupling spacing between transmitter and receiver antennas. In addition to antenna placements, supplying and measuring read-out circuitries are also very important for classification of radar systems. Another classification method is thought to be as waveform of radiated signal types. Those are listed in Figure-1.3 and they primarily determine the circuit components.

It is shown that, radar system studies include large research and development area for engineers. According to the scope of thesis, certain applications of short and small radar systems for microwave and higher frequencies are listed;

- Short Range Surveillance

- Route Traffic Control

5

- Short Range Weather Detection

- Mobility Detection

- Short Range Tracking

- Missile Guidance

- High Resolution mapping
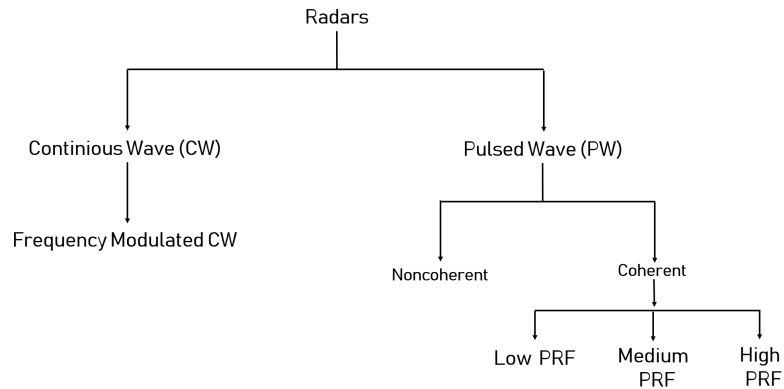
Figure 1.3. Classification of radar system by waveforms. PRF means pulse repetition frequency. Low and medium PRF mostly are used in moving target indication radars and high PRF for pulse Doppler radar. (Source: revised from theteamasterix.wordpress.com, 2018)

Among different types and sizes of radar systems, in this thesis, we are interested in quasi mono-static, continuous wave short range Doppler radar operates at 5.8 GHz, which is a very convenient platform in the ISM for avoiding complexity and expensive microwave components. The system is suitable for testing and observing performances of metamaterial antennas in practice that is the primary objective of the thesis. Similar compact radar system is proposed and realized in (Teng, 2013). However, in that thesis, simple coffee can is modified to obtain aperture antenna so that system is somewhat larger and bulky compared to ours.

When the target is in motion with the respect to the radar, the return signal frequency is shifted and this shift is called Doppler shift, see Figure-1.4. With the help of Doppler phenomena used in continuous wave radar, it is possible to detect velocity of the target by omitting relativistic effects and considering low speeds. A Doppler shift only occurs when the relative velocity vector has a radial component. (Doviak and Zrnic, 1993), as shown in Figure-1.4.
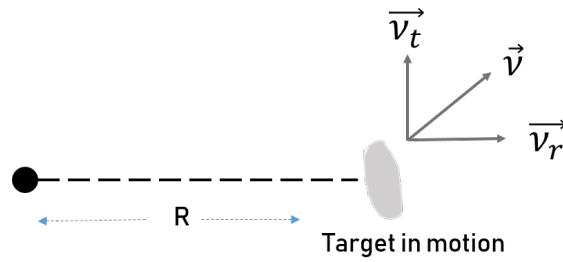
Figure 1.4. Illustration of Doppler shift of moving target with radial and tangential velocities

The relation between wavelength (λ) and frequency (f) is given as;

$$f = \frac{c}{\lambda} \tag{1.1}$$

and the frequency shift (f_d) in Hz is calculated as;

$$f_d = \frac{2 \, | \, \vec{\nu}_r \, |}{\lambda} \tag{1.2}$$

Here,

- if $f_d > 0$, target is coming close to the radar location.

- if $f_d < 0$, target is receding from the radar location.
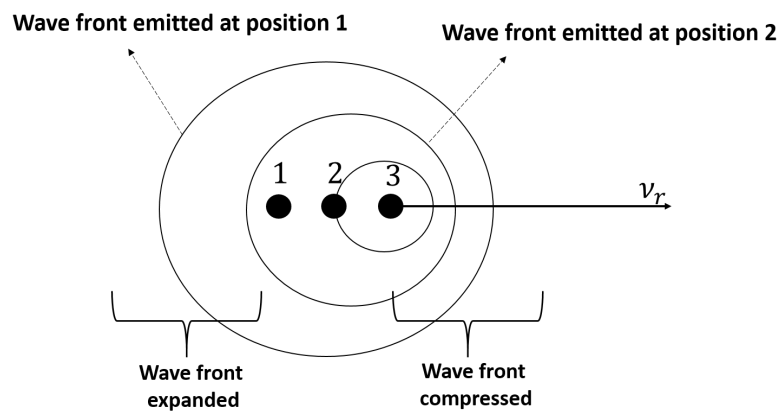
Figure 1.5. Doppler effect illustration as moving target with velocity ν_r and emits waves, (Source: revised from Jenn, 2018)

1.1.1. Short Range Radar System Design and Improvements

Block diagram given in Figure-1.6 shows operational steps of the Doppler radar system which is used for a test bench for the proposed metamaterial antennas. System mainly consist of Voltage-Controlled Oscillator (VCO), amplifiers, mixer and attenuators which are ready-to-use components with SMA connectors. All these components belong to Mini-Circuits Inc.. Therefore, detailed specifications about them can be accessed in related company documents. Exceptionally, 3 dB power divider operating at 5.8 GHz is designed according to Wilkinson type, see related chapter in (Pozar, 2012) and it is realized as well.
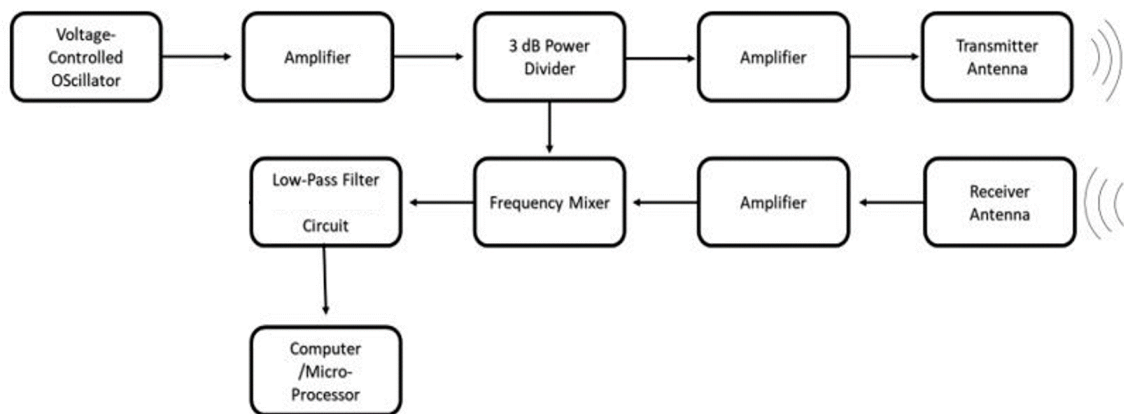
Figure 1.6. Block diagram of proposed radar system

While the radar processing, voltage-controlled oscillator generates a continuous wave (CW) signal. First the CW is amplified, and then the wave is divided and applied to the transmitter stage. At the same time, other portion of the signal is sent to the mixer which multiplies the received scattered wave including the Doppler shift and reference signal from the source stage. As a result of mixer operation, only the frequency shifted portion of the signal is obtained. Afterwards, the resultant signal is filtered by low-pass filter with high gain and processed via computer. For the filter circuit, a typical Sallen-Key fourth-order circuit having 10 KHz cut-off frequency and adjustable gain is designed, (Floyd, 2012). It should be mentioned that, second amplifier before the transmitter antenna is placed in order to radiate maximum power as much as possible products supply. Usage of second amplifier might decrease power efficiency of system, however in this way, losses due to connections, divider and cables can be eliminated.

Improvements of short-range radar systems are restricted due to low profile com-

ponents and always consideration of power efficiency issue. Additionally, cost must be taken into account such a compact system. Typical radar functions expected to be improved might be listed as;

- Range

- Velocity

- Angular direction position

- Minimum target size

Resolution and sensitivity of these measurements are also very important regarding the enhancements. Higher frequency provides wider bandwidth, so that 5.8 GHz operating frequency satisfies system demands as well. In order to get higher range accuracy and resolution which are aimed to be improved on transmitter antenna in our system. Certainly, receiver antenna must operate in same frequency band, but transmitter antenna is designed to have broad bandwidth in order to apply any other system, in case of pulsed Doppler radar where broad bandwidth is very important. Narrower beam antenna provides angle accuracy and maximum range due to its very high gain characteristic. In our case, very narrow 3-dB beam-width and high gain are considered mostly on receiver antenna.

The range equation for CW Doppler radar can be extended as Eq.-1.3; (Charvat, 2014)

$$R_{max} = \big(\frac{P_{ave}G_t A_r \rho_r \sigma \exp(2\alpha R_{max})}{(4\pi)^2 k T_0 F_n B_n \tau F_r (SNR)_1 L_s}\big)^{\frac{1}{4}} \tag{1.3}$$

- R_{max}= maximum range of radar system (m)

- P_{ave}= average transmit power (W)

- G_t= transmitter antenna gain

- A_r= receiver antenna effective aperture (m^2)

- ρ=receiver antenna efficiency

- σ= radar cross section (m^2)

- L_s=miscellaneous system losses

- α=attenuation constant of propagation medium

- F_n=receiver noise form

- k=1.38 $\times 10^{-23}$(joul/deg) Boltzmann's constant

9

- $T_0 = 290°$ K normal temperature

- B_n = system noise bandwidth (Hz)

- τF_r = 1, duty cycle for CW radar

- $(SNR)_1$ = single-pulse signal-to-noise ratio

additionally , minimum detectable signal power is given as;

$$S_{min} = 10\log(\frac{kT}{1mW}) + (NoiseFigure) + 10\log(Bandwidth) \qquad (1.4)$$

Angular resolution concerned with exact positioning of the target is one of the primary parameter which have to be improved. It might be defined as minimum distance between two equal large targets at the same range which a radar is able to distinguish and separate to each other.

$$S_A \geq 2R\sin(\frac{\theta}{2}) \qquad (1.5)$$

where θ is antenna beam-width which is half power of maximum transmitted power. (3dB beam-width), S_A is angular resolution and R is the range from antenna (m).
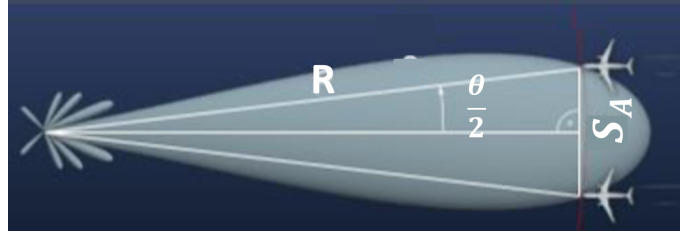
Figure 1.7. Angular beam-width illustration including targets (Source: radartutorial.eu, 2018)

1.1.2. Signal Processing

In the proposed system, the discrete Fourier transform (DFT) is applied to the received signal to analyze the Doppler spectrum generated by the moving target. DFT transforms a discretely sampled time domain signal into a frequency domain and provides the amplitude and phase according to frequencies. The frequency domain representation S_ω of a discretely sampled signal s_n is taken as the output of the Doppler radar, see Eq.-1.6. Overall number (N) of samples are computed by using Discrete-time Fourier transform, (Charvat, 2014),

$$S_\omega = \frac{1}{N} \sum_{n=-\frac{N}{2}+1}^{\frac{N}{2}} \left(s_n e^{(-j\omega n/N)} \right) \tag{1.6}$$

The DFT is a function which is implemented in MATLAB where additionally faster versions of DFT in terms of computation efficiency, that is known as Fast Fourier Transform is provided as a function of FFT. FFT is a commonly employed algorithm when the sampled data set number is chosen to power of 2. In the proposed practical radar system, Doppler signal is recorded with the help of microphone connected to a computer. The input signal is then digitalized by sound card and free software "Audacity". Hereafter, recorded signal is processed and the output is displayed using a radar interface, via open source code published by MIT. (MIT:OpenCourseWare, 2011)

1.2. Motivation and Thesis Objective

Within this framework, the main motivation of this thesis is to make use of mentioned advantages of metamaterials for antenna performance to improve the short-range Doppler radar features. Along this line, a double negative index metamaterial antenna is implemented due for providing large bandwidth and low level of side and back lobes in the radiation pattern for the transmitter. For the receiver part, near-zero epsilon metamaterial layers which support the microstrip antenna having a high gain and a narrow beam-width is designed to improve the radar range and the resolution of targets in the angular detection. The investigated radar system additionally comprises of a microstrip power divider and coaxial SMA containerized components such as a voltage-controlled oscillator, a mixer, microwave power amplifiers and attenuators so that we could build a small size and a low cost radar system.

As a summary, motivations and objective of thesis are listed as;

- **Aim**: Design of metamaterial based transmitter and receiver antennas and implement them for 5.8GHz short-range Doppler radar system.

- **Application**: Simulations and optimizations of antennas according to specific desired properties of transmitter and receiver are achieved . Then, they are fabricated, antenna performances are measured and short-range radar system with these antennas results are performed in fields.

- **Process**: To investigate metamaterial based antenna concept in engineering application and to identify the behavior of the antennas in theory, simulation and practice.

and methodology flow might be arranged as,

- Determine transmitter/receiver antenna properties of 5.8GHz short-range radar system and specify their particular design parameters

- Literature research for metamaterial based antennas in microwave band.

- Use double negative index metamaterial on patch antenna to enchance performance of transmitter such as efficiency, broad bandwidth, smaller size and gain.

- Use near-zero index metamaterial slabs over patch antenna to increase gain and decrease 3dB beam-width, significantly

- Experiments for short-range radar system with the manufactured antennas

The organization of the thesis is as in the following. The next chapter is devoted to theoretical and analytical background of metamaterial. After theory, the design of double negative index transmitter antenna and the near-zero index receiver antenna are explained according to the related literature and results for both proposed antennas are given. Afterwards, Doppler radar system performance results are illustrated in the next section. In the conclusion chapter, results and findings are summarized and commented.

CHAPTER 2

THEORETICAL BACKGROUND FOR METAMATERIAL STRUCTURES

Media which is including negative constitutive parameters have been known and studied in electromagnetism. Those constitutive parameters are negative dielectric constant ϵ_r, or negative magnetic permeability μ_r. Medium having negative-ϵ exists in nature, such as low-loss plasmas, metals and semiconductors at optical and infrared frequencies, (Ricardo Marques and Sorolla, 2008). Whereas medium having negative-μ is rare in nature due to the weak magnetic interactions. Ferromagnetic materials can be an example due to their strong magnetic interactions if losses are small enough. In order to use their "non-reciprocity properties", these ferromagnetic materials are commonly used in microwave applications.(J. B. Pendry and Stewart, 1999).
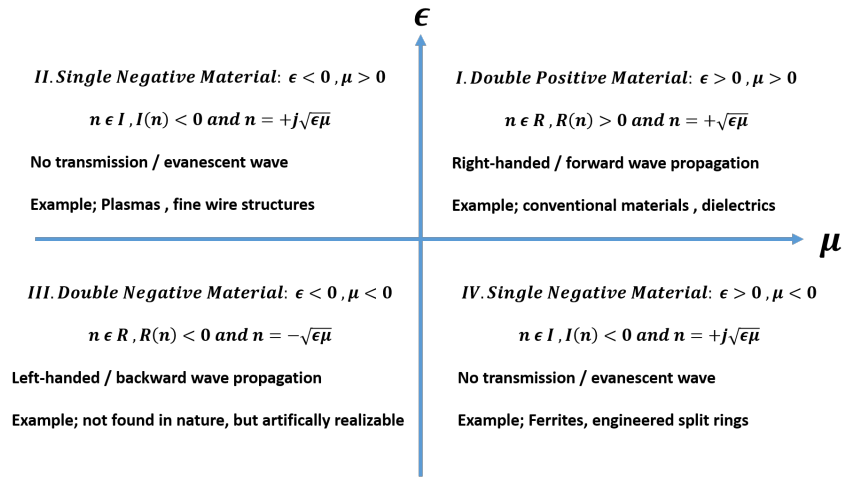
Figure 2.1. Medium classification according to signs of constitutive parameters (ϵ and μ) (Source: revised from Ricardo Marques and Sorolla, 2008)

Electromagnetic properties and wave propagation in media with simultaneously negative ϵ and μ which also called terminology of "double negative medium (DNG)" or "left-handed medium (LHM)" was analyzed by Veselago.(Veselago, 1968). The wave propagation in DNG medium and negative refraction are discussed in next section (section 2.1). The media having either single negative epsilon (ϵ) or mu (μ) is called single negative material (SNG). The whole chart given in Figure-2.1 according to signs of ϵ and

μ gives a clear view about these materials. This chapter includes review of the studies about theory and analytical solutions of metamaterials.

2.1. Double Negative Metamaterial

Well-known equation series is called as "Maxwell's equations" were written by James Clerk Maxwell in 1860's, presents relation of electric and magnetic field quantities, (Cheng, 1983),

$$\nabla \times \overrightarrow{E} = -\frac{\partial \overrightarrow{B}}{\partial t} - \overrightarrow{M} \tag{2.1}$$

$$\nabla \times \overrightarrow{H} = \overrightarrow{J} + \frac{\partial \overrightarrow{D}}{\partial t} \tag{2.2}$$

$$\nabla \cdot \overrightarrow{D} = \rho_e \tag{2.3}$$

$$\nabla \cdot \overrightarrow{B} = \rho_m \tag{2.4}$$

- $\overrightarrow{E}$ = the electric field vector (V/m) ,

- $\overrightarrow{H}$ = the magnetic field vector (A/m) ,

- $\overrightarrow{D}$ = electric flux density vector (C/m^2) ,

- $\overrightarrow{B}$ = magnetic flux density vector (Wb/m^2) ,

- $\overrightarrow{J}$ = the electric current density vector (A/m^2) ,

- $\overrightarrow{M}$ = the magnetic current density vector (V/m^2)

- ρ_e = scalar electric charge density (C/m^3) ,

- ρ_m = scalar magnetic charge density (Wb/m^3) .

∇ and $\frac{\partial}{\partial t}$ are the respectively spatial and temporal differentiations.

Constitutive relations in a medium are given as,

$$\overrightarrow{D} = \epsilon \overrightarrow{E} \tag{2.5}$$

$$\overrightarrow{B} = \mu \overrightarrow{H} \tag{2.6}$$

The wave equation can be obtained from Maxwell's equations as,

$$\nabla^2 \psi - \epsilon\mu \frac{\partial^2 \psi}{\partial t^2} = 0 \tag{2.7}$$

Here, ψ corresponds either $\overrightarrow{E}$ or $\overrightarrow{H}$. The term $\epsilon\mu$ is not effected by changes of signs of ϵ and μ at the same time due to squared of refractive index ($\frac{n^2}{c^2} = \epsilon\mu$). However;

$$\nabla \times \overrightarrow{E} = -j\omega\mu\overrightarrow{H} \tag{2.8}$$

$$\nabla \times \overrightarrow{H} = j\omega\epsilon\overrightarrow{E} \tag{2.9}$$

where $j = \sqrt{-1}$ and plane wave with space and time dependence is ; $\overrightarrow{E} = \Re\left(\overrightarrow{E}_0 e^{(-j\overrightarrow{k}.\overrightarrow{r}+j\omega t)}\right)$ and $\overrightarrow{H} = \Re\left(\overrightarrow{H}_0 e^{(-j\overrightarrow{k}.\overrightarrow{r}+j\omega t)}\right)$, where $\overrightarrow{k}$ is the propagation vector. In complex domain $\nabla = -j\overrightarrow{k}$, which is came from,

$$\nabla\overrightarrow{E} = -j\overrightarrow{k}\,\Re\left(\overrightarrow{E}_0 e^{(-j\overrightarrow{k}.\overrightarrow{r}+j\omega t)}\right) \tag{2.10}$$

Therefore relation between $\overrightarrow{E}$ and $\overrightarrow{H}$ can be written as,

$$\overrightarrow{k} \times \overrightarrow{E} = \omega\mu\overrightarrow{H} \tag{2.11}$$

$$\overrightarrow{k} \times \overrightarrow{H} = -\omega\epsilon\overrightarrow{E} \tag{2.12}$$

It is obvious that these solutions are different in DNG medium, see (Ziolkowski and Heyman, 2001 and Ricardo Marques and Sorolla, 2008). If ϵ and μ are positive, it is called "right-handed" vector system. But, if $\epsilon < 0$ and $\mu < 0$, equation are now written as;

$$\overrightarrow{k} \times \overrightarrow{E} = -\omega \mid \mu \mid \overrightarrow{H} \tag{2.13}$$

$$\overrightarrow{k} \times \overrightarrow{H} = \omega \mid \epsilon \mid \overrightarrow{E} \tag{2.14}$$

this vector system is called "left-handed" or another name is "backward media" due to existing the backward wave propagation.

The real part of Poynting vector is not affected by a simultaneous change of signs of ϵ and μ as given eq. 2.15, specifies the direction of time averaged flux of energy and in such a left-handed medium, energy and wavefronts propagate in opposite direction.

$$\vec{S} = \frac{1}{2}\vec{E} \times \vec{H}^* \qquad (2.15)$$

Here ($*$) is the complex conjugate of $\vec{H}$.
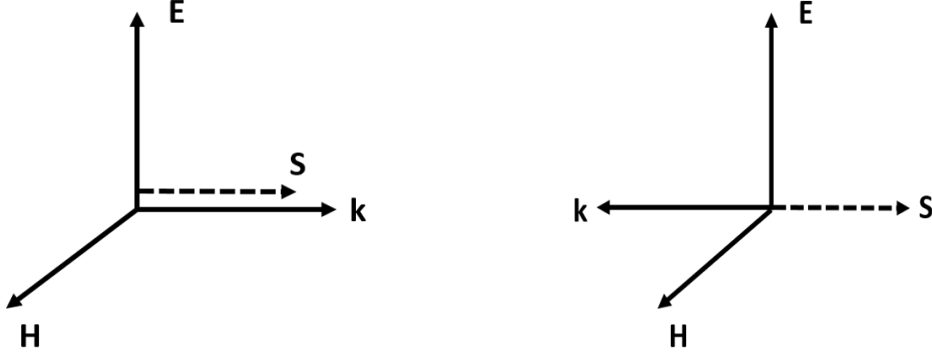
Figure 2.2. Right-handed (left) and left-handed (right) vectors system

If losses are considered, in such finite region left-handed medium without sources, there must be a portion power flow into the region so that losses can be retrieved. Complex domain Poynting equation ;

$$\nabla \cdot \{\vec{E} \times \vec{H}^*\} = j\omega(\vec{E} \cdot \vec{D}^* - \vec{B} \cdot \vec{H}^*), \qquad (2.16)$$

it follows the integral form;

$$Re\{ \oint \vec{E} \times \vec{H}^* \cdot \hat{n} \, dS \} = \omega Im\{ \int (\mu \mid \vec{H} \mid^2 - \epsilon^* \mid \vec{E} \mid^2 dV) \} < 0, \qquad (2.17)$$

which implies,

$$Im(\epsilon) < 0 \qquad \text{and} \qquad Im(\mu) < 0. \qquad (2.18)$$

A plane wave propagating in lossy left-handed medium having $Re(\epsilon < 0)$ and $Re(\mu < 0)$ with propagating constant square is $k^2 = \omega^2\mu\epsilon$, and the Eq.-2.18 means $Im(k^2) > 0$, so that;

$$\{Re(k) > 0 \text{ and } Im(k) > 0\} \quad \text{or} \quad \{Re(k) < 0 \text{ and } Im(k) < 0\}, \qquad (2.19)$$

Considering transparent non-dispersive medium, time averaged energy density written as;

16

$$U_{nd} = \frac{1}{4}\{\epsilon \mid \overrightarrow{E} \mid^2\} + \mu \mid \overrightarrow{H} \mid^2\}, \tag{2.20}$$

if ϵ and μ are negative in such a medium, the Eq.-2.20 gives negative density of energy which is non-physical. Let us consider new medium which is very weak dispersive. As we know that any real physical medium must be dispersive excluding vacuum. If energy density is written for dispersive medium,

$$U = \frac{1}{4}\{\frac{\partial(\omega\epsilon)}{\partial\omega} \mid \overrightarrow{E} \mid^2 + \frac{\partial(\omega\mu)}{\partial\omega} \mid \overrightarrow{H} \mid^2 \}, \tag{2.21}$$

If positive energy is considered, it must follows that,

$$\frac{\partial(\omega\epsilon)}{\partial\omega} > 0 \qquad \text{and} \qquad \frac{\partial(\omega\mu)}{\partial\omega} > 0, \tag{2.22}$$

which is in agreement with,

$\epsilon < 0$ and $\mu < 0$ with $\partial\epsilon/\partial\omega > \mid \epsilon \mid /\omega$ and $\partial\mu/\partial\omega > \mid \mu \mid /\omega$, as low-loss Drude-Lorentz model for ϵ and μ says that in the highly dispersive medium, just above the resonance frequency , ϵ and/or μ can be negative which is compatible with that left-handed medium must be highly dispersive, see (Ricardo Marques and Sorolla, 2008). The propagation in backward media came out with opposite signs of phase and group velocities,

$$\frac{\partial k^2}{\partial\omega} = 2k\frac{\partial k}{\partial\omega} \equiv 2\frac{\omega}{\nu_p\nu_g}, \tag{2.23}$$

where $\nu_p = \omega/k$ and $\nu_g = \partial\omega/\partial k$, respectively. As aforementioned squared propagation constant $k^2 = \omega^2\epsilon\mu$ and from expression 2.22,

$$\frac{\partial k^2}{\partial\omega} = \omega\epsilon\frac{\partial(\omega\mu)}{\partial\omega} + \omega\mu\frac{\partial(\omega\epsilon)}{\partial\omega} < 0, \tag{2.24}$$

and considering Eq.-2.23 and Eq.-2.24,

$$\nu_p\nu_g < 0. \tag{2.25}$$

propagation in reverse direction of phase and group velocities can be an evidence of backward wave propagation for ϵ and μ are negative medium.

Let us consider the refraction at the interface of left-handed medium, when optical ray cames from ordinary right-handed medium; (Nader Engheta, 2006)

$$\frac{\sin(\theta_i)}{\sin(\theta_r)} = \frac{- \mid \overrightarrow{k}_2 \mid}{\mid \overrightarrow{k}_1 \mid} \equiv \frac{n_2}{n_1} < 0, \tag{2.26}$$

17

that is the Snell's law and n_1 is the refraction indice of right-handed medium and n_2 is the indice of left-handed medium, so that it yields opposite sign of angles between refraction and incidence as given in Figure-2.3. Square root of refractive index should be chosen as negative;

$$n \equiv -c\sqrt{\epsilon\mu} \; < \; 0. \tag{2.27}$$
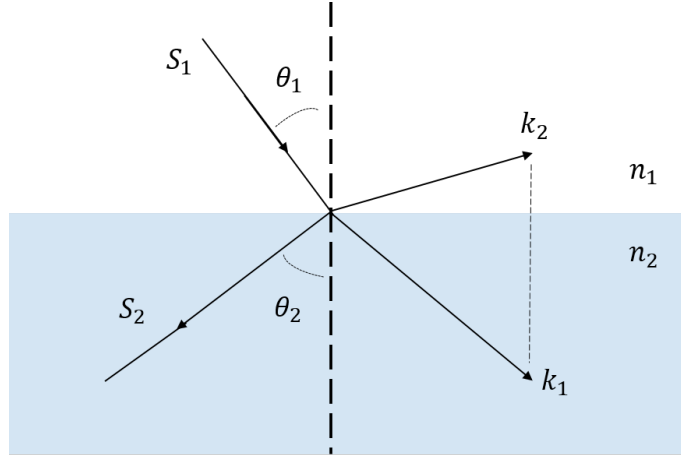
Figure 2.3. Negative refraction between right-handed (n_1) and left-handed (n_2) medium. S and k are Poynting and propagation vectors, respectively.

2.1.1. Negative-Epsilon (ϵ) Media

Pendry et. al. proposed a technique for degradation of the plasma frequency into the far infrared or even microwave band by using periodic structures which are built by very thin wires adulterate the average concentration of electrons so that boost the effective electron mass through self-inductance, see (J. B. Pendry and Youngs, 1996). Plasmon is defined as a collective oscillation of electron density and frequency of plasmon can be written as,

$$\omega_p^2 = \frac{ne^2}{\epsilon_0 m_{eff}} \tag{2.28}$$

where ω_p is plasma frequency, n is density of electron and e is electron charge. For, dielectric function interacted with electromagnetic wave,

$$\epsilon(\omega) = 1 - \frac{\omega_p^2}{\omega(\omega + i\gamma)}, \tag{2.29}$$

18

is given. Now considering a simple wire structure as given Figure-2.4, where r and a indicated as well. Effective density of electron mass is given as in Eq.-2.30,
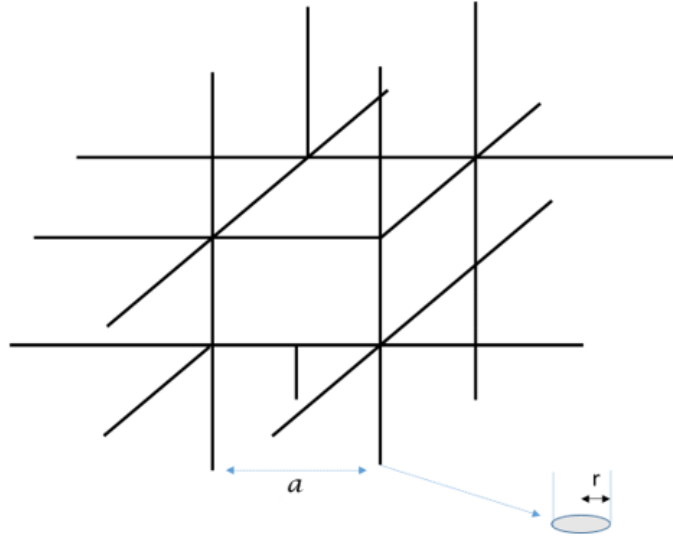
Figure 2.4. A periodic structure of simple cubic infinitely arranged thin wire

$$n_{eff} = n\frac{\pi r^2}{a^2} \tag{2.30}$$

Current I flows on the thin wire excites magnetic field $\overrightarrow{H}$ turning around the thin wire,

For only radial component of magnetic field vector,

$$H(R) = \frac{\pi r^2 nve}{2\pi R} \tag{2.31}$$

where R is radial distance to the center of wire and v is the electron velocity. Vector potential ($\overrightarrow{A}$) of magnetic field is defined as,

$$\overrightarrow{H}(R) = \mu_0^{-1}\nabla \times \overrightarrow{A}(R) \tag{2.32}$$

Therefore, radial component of vector potential is defined as,

$$A(R) = \frac{\mu_0 \pi r^2 nve}{2\pi}\ln(a/R), \tag{2.33}$$

where a is the lattice constant and $\mu_0 = 4\pi \times 10^{-7}\ H/m$.

Physics of classical mechanics say that, electrons are affected by magnetic field have an extra additive to their momentum of $e\overrightarrow{A}$. So that momentum per unit length of the wire is given as,

$$\pi r^2 e n A(r) = \frac{\mu_0 \pi^2 r^4 e^2 n^2 v}{2\pi} \ln(a/r) = m_{eff} \pi r^2 n v \qquad (2.34)$$

at the last part of Eq.-2.34, newly m_{eff} is defined as effective mass of the electrons and equals that,

$$m_{eff} = \frac{\mu_0 \pi r^2 e^2 n}{2\pi} \ln(a/r). \qquad (2.35)$$

Electrons which are restricted in bounded thin wires enhance the magnitude of their masses significantly. An example for this enhancement is given in as a conclusion of Pendry et. al. study (J. B. Pendry and Youngs, 1996), for a plasma frequency of such a artificially designed meta-structure is given as,

$$\omega_p^2 = \frac{n_{eff} e^2}{\epsilon_0 \mu_{eff}} = \frac{2\pi c_0^2}{a^2 \ln(a/r)}, \qquad (2.36)$$

where ω_p is the plasma frequency and ω is the frequency of excitation electromagnetic wave. So that, according to Drude model for conductors, effective permittivity such a conductor material is given as,

$$\epsilon_{eff} = 1 - \frac{\omega_p^2}{\omega(\omega + j\epsilon_0 a^2 \omega_p^2 / \pi r^2 \sigma)}, \qquad (2.37)$$

where the σ is the conductivity of metal. Negative or even near-zero epsilon ϵ can be realized just above the resonant frequency or very close to resonant frequency.

2.1.2. Negative-Mu (μ) Media

J.B. Pendry et. al., in (J. B. Pendry and Stewart, 1999) shows that micro-structures formed by non-magnetic conducting thin sheets of metal shape can provide tunable an effective permeability μ_{eff}, and medium including periodicity of these micro-structures can exhibits negative permeability medium ($\mu_{eff} < 0$). This section reviews that how to calculate μ_{eff} by proposed some model structures which are mentioned one by one, and shows how electrostatic energy can be strongly concentrated in these structures. It also demonstrates the potential for enhancing non-linear effects by magnetic activity. In order to satisfy effective permeability definition, micro-structures must be much less in size than the wavelength of the excitation wave. Periodic structures are defined by a unit cell characteristic dimension "a",

$$a << \lambda = 2\pi c_0 \omega^{-1} \qquad (2.38)$$

This condition must be satisfied to avoid possible diffraction and refraction at micro-structures. If we write magnetic and electric flux density in terms of effective ϵ and μ,

$$\overrightarrow{B}_{ave} = \mu_{eff}\mu_0 \overrightarrow{H}_{ave}, \tag{2.39}$$

$$\overrightarrow{D}_{ave} = \epsilon_{eff}\epsilon_0 \overrightarrow{E}_{ave}. \tag{2.40}$$

Analysis begins with simple periodic aligned array of cylinders as given in Figure-2.5
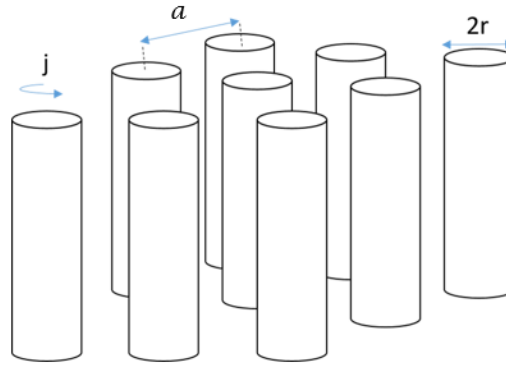
Figure 2.5. Array of metalic cylinders in direction of parallel magnetic field to their axes

Parallel magnetic field to their axes, $\overrightarrow{H}_0$ is applied externally to the perfect conducting cylinders and the current density $\overrightarrow{J}$ flows as given in 2.5. The total field (H) inside cylinder is,

$$\overrightarrow{H} = \overrightarrow{H}_0 + \overrightarrow{J} - \frac{\pi r^2}{a^2}\overrightarrow{J} \tag{2.41}$$

The current yields directly the second term of right side, and de-polarizing fields at the far edges of cylinders yield third term of right side. If we write total electromotive force (emf) rotating the surroundings of cylinder is,

$$emf = -\pi r^2 \mu_0 \frac{\delta}{\delta t}[\overrightarrow{H}_0 + \overrightarrow{J} - \frac{\pi r^2}{a^2}\overrightarrow{J}] - 2\pi r R \overrightarrow{J} \tag{2.42}$$

$$emf = +\omega\pi r^2 \mu_0 [\overrightarrow{H}_0 + \overrightarrow{J} - \frac{\pi r^2}{a^2}\overrightarrow{J}] - 2\pi r R \overrightarrow{J} \tag{2.43}$$

Surface per unit area resistance of cylinder is indicated by R. Units are voltages for both first and second term, $2\pi r R \overrightarrow{J}$, is voltage drop due to resistance loss of cylinder. In order to find the current density j, the net electromotive force (emf) must be balanced to zero,

$$j\omega\pi r^2 \mu_0 [\overrightarrow{H}_0 + \overrightarrow{J} - \frac{\pi r^2}{a^2}\overrightarrow{J}] - 2\pi rR = 0 \qquad (2.44)$$

$$\overrightarrow{J} = \frac{-\overrightarrow{H}_0}{[1 - \frac{\pi r^2}{a^2}] + j[\frac{2rR}{\omega r \mu_0}]} \qquad (2.45)$$

By using flux densities for such resonant structures which are assumed to be much smaller in size than wavelength;

$$\overrightarrow{B} = \mu_0 \mu_r \overrightarrow{H} \qquad (2.46)$$

$$\overrightarrow{D} = \epsilon_0 \epsilon_r \overrightarrow{E} \qquad (2.47)$$

$\overrightarrow{H}$ will be used as average H-field outside of the cylinders where having no rotating current,

$$\overrightarrow{H} = H_0 - \frac{\pi r^2}{a}\overrightarrow{J} \qquad (2.48)$$

Substituting the current density Eq.-2.45 into the equation of average H-field Eq-2.48,

$$\overrightarrow{H} = \overrightarrow{H}_0 - \frac{\pi r^2}{a}\frac{-\overrightarrow{H}_0}{[1 - \frac{\pi r^2}{a^2}] + j[\frac{2rR}{\omega r \mu_0}]}, \qquad (2.49)$$

$$\overrightarrow{H} = \overrightarrow{H}_0 \frac{1 + i\frac{2R}{\omega r \mu_0}}{[1 - \frac{\pi r^2}{a^2}] + j[\frac{2rR}{\omega r \mu_0}]}, \qquad (2.50)$$

Here, we define effective permeability as,

$$\mu_{eff} = \frac{\overrightarrow{B}_{ave}}{\mu_0 \overrightarrow{H}_{ave}} = \frac{1 - \frac{\pi r^2}{a^2} + j\frac{2R}{\omega r \mu_0}}{1 + \frac{2R}{\omega r \mu_0}}, \qquad (2.51)$$

$$\mu_{eff} = 1 - \frac{\pi r^2}{a^2}[1 + j\frac{2R}{\omega r \mu_0}]^{-1}. \qquad (2.52)$$

2.1.2.1. Capacitive Array of Sheets Wound on Cylinders

In first section, the magnetic property of array of cylinder is analyzed when parallel external magnetic excitation exist. Now, structure like "split-ring" at the wounded
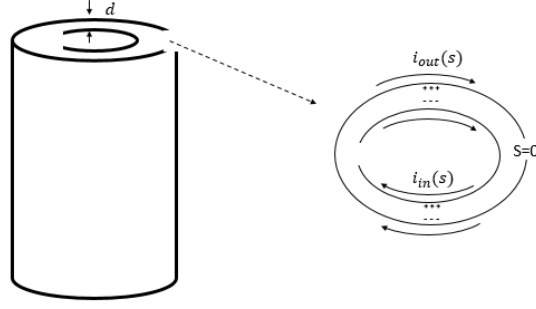
Figure 2.6. Wounded sheets as split ring way

top ends plane which is perpendicular to longitudinal axis of cylinder is derived, as given in Figure-2.6. Externally applied magnetic field creates currents in the split-rings which have internal gap allowing current flow from one ring to another, and this magnitude of the current proportional to capacitance (C) between two rings. If the same calculation process is applied to array of wounded sheets as done for array of cylinder, effective permeability can be written as;

$$\mu_{eff} = 1 - \frac{\pi r^2}{a^2} [1 + j\frac{2R}{\omega r \mu_0} - \frac{3}{\pi^2 \mu_0 \omega^2 C r^3}]^{-1}, \tag{2.53}$$

and capacitance;

$$C = \frac{\epsilon_0}{d} = \frac{1}{dc_0^2 \mu_0}, \tag{2.54}$$

where d is the spacing between conducting plates. Substituting the capacitance Eq.-2.54 into effective permeability Eq.-2.53;

$$\mu_{eff} = 1 - \frac{\frac{\pi r^2}{a^2}}{1 + \frac{2Rj}{\omega r \mu_0} - \frac{3dc_0^2}{\pi^2 \omega^2 r^3}}, \tag{2.55}$$

J.B. Pendry et. al. define resonance frequency ω_0 and magnetic plasma frequency ω_{mp} which is result of enhancing thermal movement of electrons creates displacement that yields a momentary formation of an electric field due to a small charge isolation whereas Coulomb force creates reconditioning of electron's position and repeating following in oscillations, (for further detailed analyses, see (J. B. Pendry and Stewart, 1999).

$$\omega_0 = \sqrt{\frac{3}{\pi^2 \mu_0 C r^3}} = \sqrt{\frac{3dc_0^2}{\pi^2 r^3}}, \tag{2.56}$$

$$\omega_{mp} = \sqrt{\frac{3}{\pi^2 \mu_0 C r^3 (1 - \frac{\pi r^2}{a^2})}} = \sqrt{\frac{3dc_0^2}{\pi^2 r^3 (1 - \frac{\pi r^2}{a^2})}}. \tag{2.57}$$

23

For negative effective permeability μ_{eff} frequencies that is just above the magnetic plasma frequency (ω_{mp}), electromagnetic waves cannot propagate and evanescent waves occurs as long as effective permittivity is positive, $\epsilon_r > 0$.

2.1.2.2. Split Ring Resonator
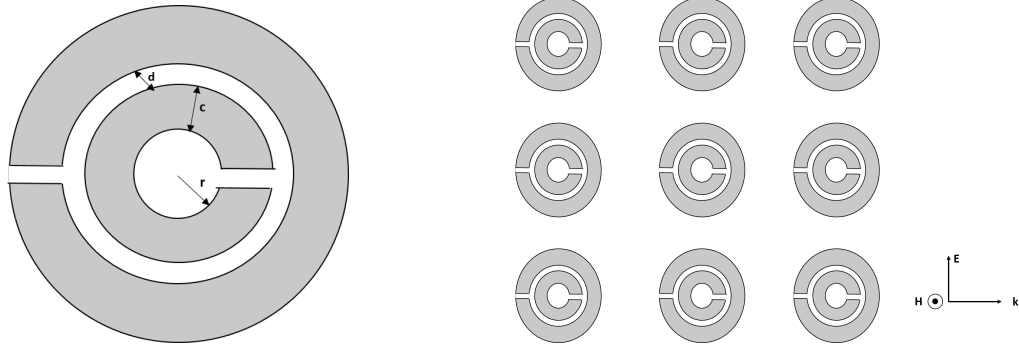
Figure 2.7. Single split ring resonator and its corresponding array. Gray area is conductor and white is dielectric

Disk shaped split ring design is developed to overcome poor magnetic response of former wounded metal sheets. Array of disk shaped structures is more responsive to polarization of magnetic field. If one analytically derives the capacitance between two thick rings, effective permeability μ_{eff} can be calculated. Before designing split ring resonator, following notes by J.B. Pendry et. al. must be kept in view, (J. B. Pendry and Stewart, 1999),

- $r >> c$, r is inner ring radial distance to the center and c is width of rings.

- $\ln(\frac{c}{d}) >> \pi$, d is gap distance between two rings

- $l < r$, here l is defined as separation between two structure.

Obeying these rules, capacitance between two strips is calculated as,

$$C' = \frac{\epsilon_0}{\pi} \ln(\frac{2c}{d}) = \frac{1}{\pi \mu_0 c_0^2} \ln(\frac{2c}{d}) \qquad (2.58)$$

where the two parallel sections here are in unit length. By using the permeability relation of the capacitive array of sheets wound on cylinders (Eq.-2.55), μ_{eff} and resonance frequency ω_0 for disk shaped design now can be found by;

24

$$\mu_{eff} = 1 - \frac{\frac{\pi r^2}{a^2}}{1 + \frac{2Rj}{\omega r \mu_0} - \frac{3dc_0^2}{\pi^2 \omega^2 r^3}}$$ (2.59)

$$\omega_0 = \sqrt{\frac{3lc_0^2}{\pi \ln(\frac{2c}{d}r^3)}}$$ (2.60)

2.1.2.3. Complementary Split Ring Resonator
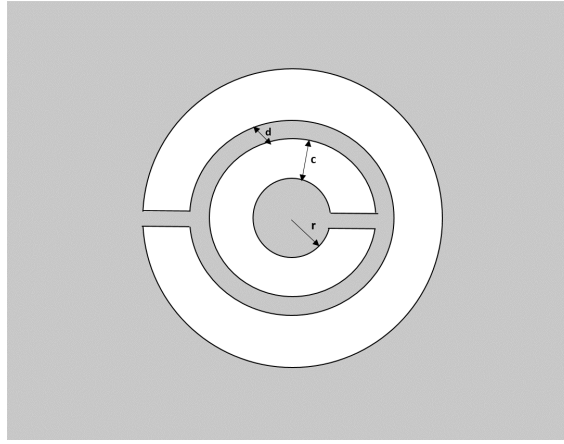
Figure 2.8. Complementary split-ring resonator. Gray area is conductor, white is dielectric.

As mentioned it is in the previous section, split-ring resonator are easily designable resonant structures in microwave frequencies. By excitation of external magnetic field parallel to their ring axis, an emf around the rings is produced which induces a circulating current in the rings and that current is restricted along the distributed capacitance between disc rings. In addition to that, Split rings shows an equivalent model of LC circuit driven by externally with resonant frequency which can be easily tuned by given structure dimensions. Resonant frequency calculation equations are given in Eq.-2.58 - 2.60. By remanding the concepts of duality and complementarity theorem (Falcone and et al., 2004 and Baena and et al., 2005), complementary split ring resonator (CSRR) can be evaluated directly from split ring resonator (SRR) structure easily. This new structure (CSRR), which in planar technology can be defined as the negative (complementary) of SRR, shows an electromagnetic property which is almost dual of SRR. Specifically, a negative-ϵ effective permittivity can be expected for any CSRR-based medium, whereas a negative-μ behavior arises in an equivalent SRRs medium. (Baena and et al., 2005)

Duality theorem implies that, if one has a solutions of one set (i.e. $\overrightarrow{J} \neq 0, \overrightarrow{M} = 0$), the solutions for other set (i.e. $\overrightarrow{J} = 0, \overrightarrow{M} \neq 0$) can be evaluated a suitable interchange of quantities. The dual quantities are listed in Table-2.1 for electric and magnetic sources, (Balanis, 2005),

Table 2.1. Duality Theorem

Electric Sources($J \neq 0, M = 0$)	Magnetic Sources($J = 0, M \neq 0$)
$\overrightarrow{E}_A$	$\overrightarrow{H}_F$
$\overrightarrow{H}_A$	$-\overrightarrow{E}_F$
$\overrightarrow{J}$	$\overrightarrow{M}$
$\overrightarrow{A}$	$\overrightarrow{F}$
ϵ	μ
k	k
η	$\frac{1}{\eta}$
$\frac{1}{\eta}$	η

In order to create strong electric dipole which affects the CSRRs resonant frequency and gives an opportunity to obtain negative permittivity, CSRRs must be excited by parallel electric field to their axes. Both SRRs and CSRRs have approximately the same resonance frequencies due to their oppositely dual shared dimensions. (Pasakawee, 2012). In the beginning of proceeding chapter, designed and optimized in simulation software CST:Microwave Studio, complementary split-ring resonator (CSRR) is presented.

CHAPTER 3

METAMATERIAL ANTENNA DESIGN

In this chapter, double negative index metamaterial based transmitter antenna and near-zero index metamaterial supplied receiver antenna designs and their simulation and measurement results are given.

3.1. Transmitter Antenna Design: Double Negative Metamaterial Antenna

Microstrip patch antennas are commonly preferred in case of practical and low power applications, since they offer low cost, lightweight and easy fabrication techniques on planar surfaces. However, there are trade off between antenna performance and physical parameters. A thicker substrate is able to broaden bandwidth, on the other hand it might raise the power loss as well, see (R.Garg and A.Ittipiboon, 2001). Additionally, microstrip patch antennas usually have some undesired radiation in lateral directions through the patch plane such as surface waves and leaky waves while the main lobe is vertical to patch plane. In order to dope out for unwanted conditions, double negative metamaterial based patch antenna for transmitter is proposed considering mainly the reference study by Lie et al. (Le-Wei Li and Martin, 2010). In this way radiation efficiency is improved in the horizontal direction and significant size reduction is achieved. Another important achievement is acquired on broader bandwidth contrary to very narrow bandwidth of typical patch. A typical patch antenna consists of uniform conductor shape such as rectangular, circular or etc. over the dielectric substrate with covered ground plane at the bottom and fed by microstrip line or connector via hole from directly ground side to the patch. In proposed antennas, microstrip line feeding way is chosen due to the simplicity of the design. Dimensions of microstrip line are calculated by Eq.-3.1-3.2, (Pozar, 2012),

$$\epsilon_{eff} = \frac{\epsilon_R + 1}{2} + \Big[\frac{\epsilon_R - 1}{2\sqrt{1 + 12(\frac{H}{W})}}\Big], \tag{3.1}$$

$$Z_0 = \frac{120\pi}{\sqrt{\epsilon_{eff}}\big[\frac{W}{H} + 1.393 + \frac{2}{3}\ln(\frac{W}{H} + 1.444)\big]}, \tag{3.2}$$
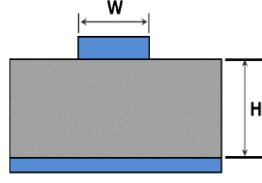
Figure 3.1. Cross-section of microstrip line, (Source: pasternack.com, 2018)

For transmitter and also receiver antenna, metamaterial behaviors are created on rectangular form patch antenna due to providing regularity and easy implementation with certain edges which are suitable for resonator structures. Rectangular patch antenna dimensions can be calculated by Eq.-3.3-3.4, (Balanis, 2005),
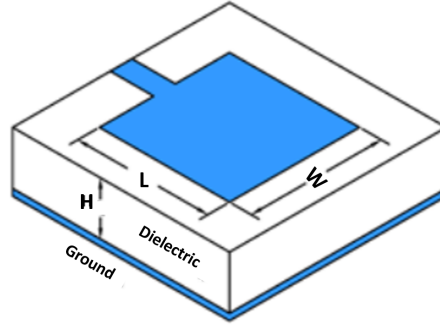
Figure 3.2. Typical rectangular patch antenna, (Source: pasternack.com, 2018)

$$W = \frac{c}{2f_0\sqrt{\dfrac{\epsilon_R + 1}{2}}}, \tag{3.3}$$

$$L = \frac{c}{2f_0\sqrt{\epsilon_{eff}}} - 0.824h\left(\frac{(\epsilon_{eff} + 0.3)(\frac{W}{H} + 0.264)}{(\epsilon_{eff} - 0.258)(\frac{W}{H} + 0.8)}\right). \tag{3.4}$$

where W and H are indicated in Figure-3.2, and f_0 is demanded radiation frequency.

With the help of the equations given above, microstrip patch which is used as base radiating element, is designed. Further, final design of the patch consists of two different resonator structures. Periodically arrayed cross-strip line etched on ground structures provide negative permeability μ, in the same way, periodically arrayed CSRRs etched on conducting surface provide negative permittivity ϵ, as mentioned in theoretical background in

chapter 2: negative epsilon ϵ and negative μ sections. Like dual relation between SRR and CSRR, according to complementary and duality theorem also discussed in section 2.2.3 (Falcone and et al., 2004), if one takes complementary of the mesh-like conducting thin wires structure which is related to obtain negative ϵ, the new one is expected to provide negative μ and new structure looks like conducting square patches separated with etched cross-strip lines. These two resonator structures are particularly investigated and sim-
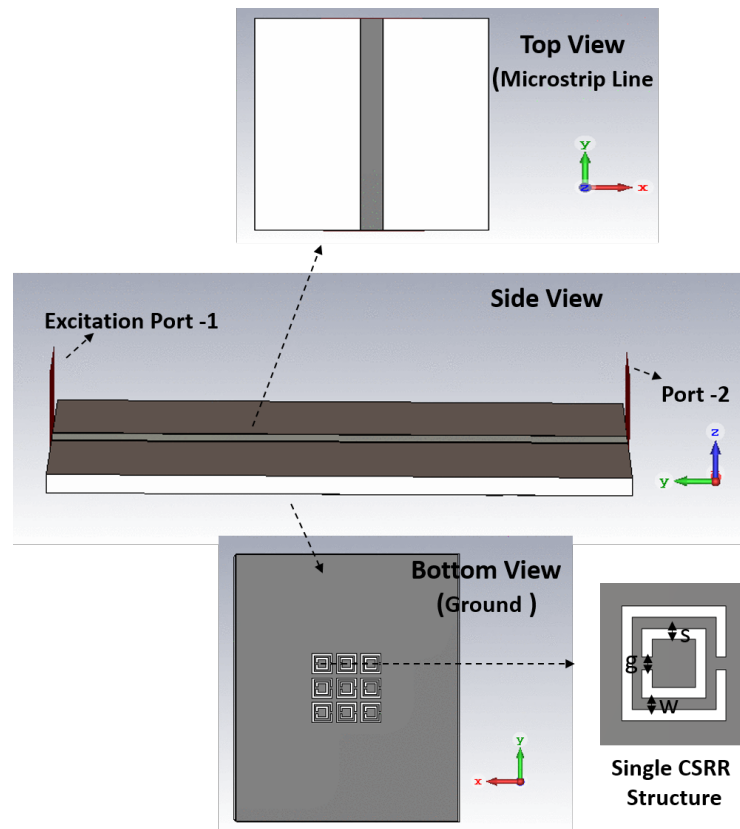
Figure 3.3. Coupled CSRRs with excitation microstrip line. Substrate is Roger 4730 with ϵ_r=3.00, loss-tangent=0.0027 and thickness is 1.52 mm. Microstrip line width is 3.87 mm and its length is 48 mm, for CSRR structure w=s=0.35 mm, g=0.4 mm and separation between two CSRR is 0.8 mm.

ulated one by one in excitation setup to find proper design parameters. Detailed images from simulation for top and bottom layers of the excitation setup are given in Figure-3.3 and Figure-3.5. In the similar study by Lie et al., micro-triangle resonators are used in order to obtain negative effective permittivity, (Le-Wei Li and Martin, 2010). However, CSRR is a well-known structure and many studies show the behaviors by analytically and experimentally so that proposing CSRR to create such a medium, makes design phase more shorter and consistent. Likewise, it is required relatively easier design and imple-mentation. In order to obtain double negative medium through typical rectangular patch

antenna, resonance frequency and dimensions of CSRRs etched on ground are determined and calculated with the help of related study where resonance frequencies corresponding to design parameters for CSRR are listed, see (Baena and et al., 2005). Additionally, reference studies show that CSRR can provide effective negative permittivity in certain frequency band around the resonance. For calculating the dimensions of ground etched by cross-strip, Eq.-2.36 is used. However final design parameters have been reached by the help of parametric solution and optimization tool of simulation software of CST:MW. Firstly, single CSRR is examined in order to find appropriate dimensions, then 9 CSRRs are coupled to see coupling effect on resonance characteristic. Figure-3.3 shows coupled CSRRs etched on ground and excited by microstrip line. As a substrate low-loss Roger 4730 with $\epsilon_r = 3.00$ is chosen. Figure-3.4 gives the S21 curves for a single CSRR structure and coupled of CSRRs. S21 or transmitted power means that ratio of transferred power from port-1 to port-2, to incident power at port-1. So that, for both, resonance frequency is observed between 5.4 and 5.5 GHz. It should be noted here, this results belong to the structures having same dimensions as final design.
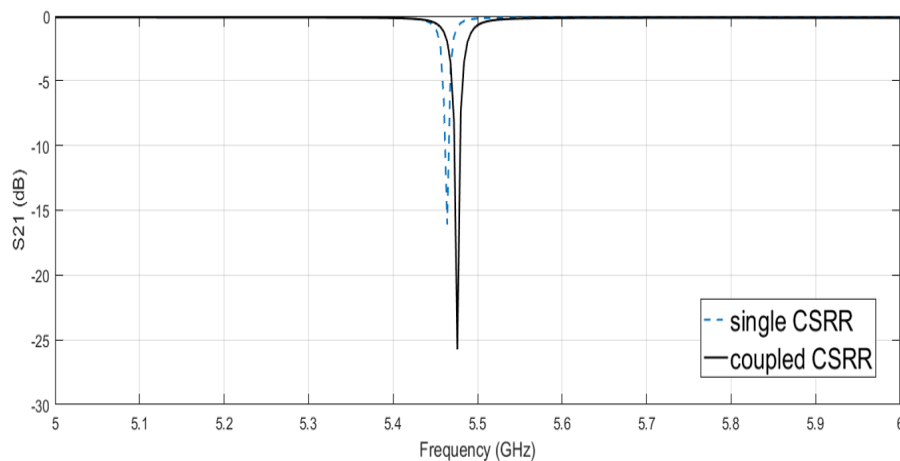
Figure 3.4. S21 for single CSRR and coupled CSRRs

In the same way, cross-strip lines etched on ground is excited by microstrip line given in Figure-3.5, and S21 curve is shown in Figure-3.6. To satisfy criteria of double negative medium, two resonance structures composition (CSRRs and mesh-grid ground) must resonate in same band or overlap as given in Figure-3.6.

These two designed resonance structures are integrated onto typical patch antenna and fed by microstrip transmission line. Final design for antenna given in Figure-3.7 includes 12 CSRR and also on the bottom layer, 30 partial square grounds formed by etched cross-strip lines, are placed. Details for single CSRR and four small square ground can be
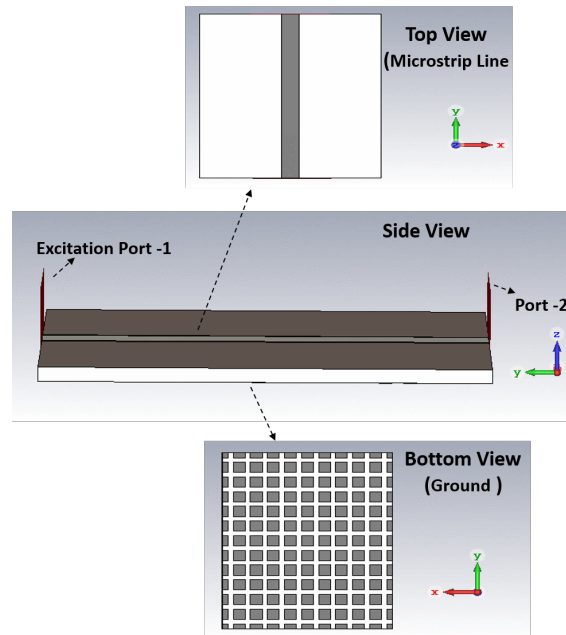
Figure 3.5. Mesh-grid ground with excitation microstrip line. Substrate is Roger 4730 with ϵ_r=3.00, loss-tangent=0.0027 and thickness is 1.542 mm. Microstrip line width is 3.87 and its length is 48 mm, for mesh-grid structure; separation of two etched lines a=2.8 mm and etched single line width r=1.2 mm

seen in the figure. Roger 4730 having relative permittivity of $\epsilon_r = 3.00 \pm 0.05$, thickness 1.52 mm with low-losses is preferred as a substrate. The patch size is 12x16 mm^2 and other dimensions related with stated geometrical forms in the shapes is explained in the figure. All dimensions are optimized by using electromagnetic simulator (CST:MW). It should be noted that, on the bottom, etching of cross-strip lines start at end of the micro strip line for the purpose of avoiding impedance miss-match along the transmission and feeding.

As discussed in theory, CSRRs on top have a dominant capacitive (C) element, whereas array of partial grounds on bottom have a dominant inductance (L) element so that coupling between upper patch and bottom ground which is assumed as form of capacitive-inductive (C-L) in equivalent circuit model, can induce backward wave propagating along the patch of plane. In this case, array of CSRRs hold the dominant electric field in resonance, whereas the partially ground configuration is related with the resonance behavior of the magnetic field. Therefore, two frequency bands must occur along the radiating characteristic of the antenna. Supposing only one of the layers is implemented on the structure then a stop-band behavior is expected at the operating frequency due to a single negative medium. To adjust pass-band for the desired spectrum, parameters of
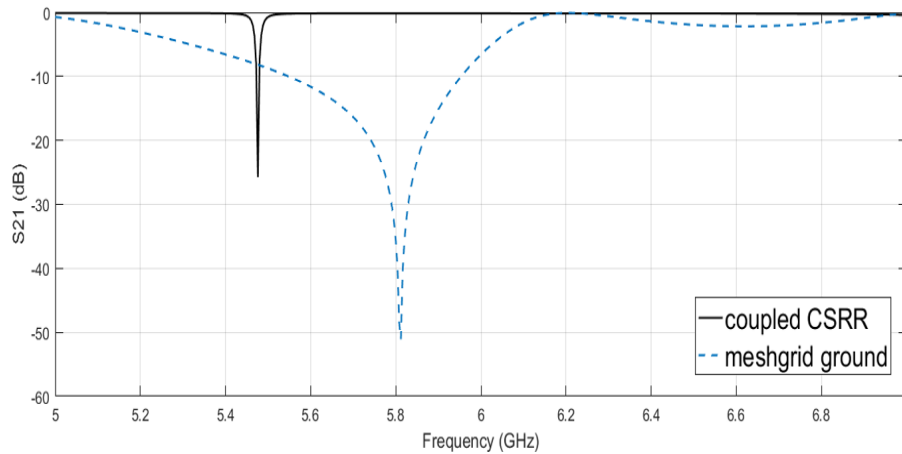
Figure 3.6. S21 for single cross-strip lines etched on ground and comparison with coupled CSRRs

both resonators such that two different pass-bands encounter at 5.8 GHz, are optimized regarding to patch part of the antenna. Further information on the electromagnetic properties and equivalent circuits of left-handed CSRR and cross strip-line structures can be found in (Falcone and et al., 2004; Baena and et al., 2005; George V. Eleftheriades and Kremer, 2002).

For classical antenna part, after several parametric simulations, rectangular patch sizes are determined considering integer numbers which define two-dimensional CSRR arrays. Each CSRR cell has dimensions of $4 \times 4 \ mm^2$ and 3×4 rectangular array is suitable so that total size of rectangular patch becomes $12 \times 16 \ mm^2$. According to patch antenna dimension equations (Eq.-3.3 and Eq.-3.4), this sizes correspond approximately ≈ 6.6 GHz and satisfy the criteria by staying in estimated radiation bandwidth.

From s-parameters, S11 or return-loss defines the ratio of reflected wave power to the incident power for same excitation point. Return-loss (S11) (Figure-3.7) and voltage standing wave ratio (Figure-3.9) characteristics for simulated antenna show radiation bandwidth (accepted as below than -10 dB) is start from 4 GHz up to the 7.6 GHz where broad bandwidth characteristic is achieved as expected for such a small planar patch antenna. Return-loss values also are very satisfying along the entire band and especially for around the desired operating frequency (5.8 GHz). It can reach value of below than -20 dB.

It should be noted that, if only one of resonance structures implemented to patch antenna, single negative medium can be existed and than it shows stop-band characteristic. Therefore, providing that first resonance frequency regions by bottom and second
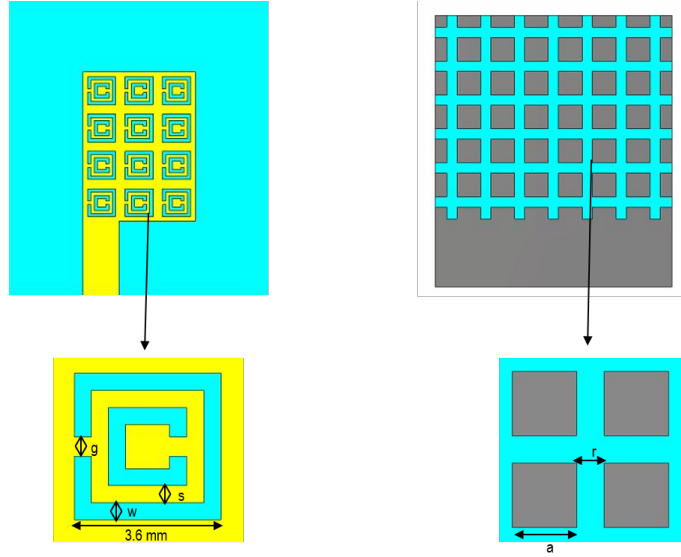
Figure 3.7. Design of double negative index metamaterial based patch antenna. Substrate is Roger 4730 with $\epsilon_r = 3.00$ and thickness is $1.52\ mm$. Total size $28 \times 32\ mm^2$, area of upper patch is copper (yellow) and its size $12 \times 16\ mm^2$. $w = s = 0.35\ mm$, $g = 0.4\ mm$, $a = 2.8\ mm$, $r = 1.2\ mm$. For ground, PEC (gray) is used.

resonance by upper patch fall with same bandwidth or there is a big overlap between first resonance curve and second, double negative medium can be existed and it produce passband characteristic. Therefore, energy can be radiated along patch plane and frequency independence succeed in that frequency range, while impedance matching at the feeding always being regarded. This horizontal radiation can be noticeable very well in 3D radiation pattern in Figure-3.10.

Simulations were performed in HP-Z820 work-station (for properties, see related company documents). Figure-3.11 show convergence of graph of S parameters and meshcells, respectively, according to number of pass which is related with "adaptive mesh refinement" algorithm tool of CST software. Here, "Delta-s" (ΔS) refers to the numerical difference between S11 value of current pass and the previous one, and meshcells are "tetrahedron" cells which are used in frequency domain solver.

Before presenting results of radiation characteristic, basic definitions from antenna terminology are given to be reminded. According to IEEE standard definition, directivity is "the ratio of the radiation intensity in a given direction from antenna to the radiation intensity averaged over all directions", see (Balanis, 2005).

$$D = \frac{U}{U_0} = \frac{4\pi U}{P_{rad}} \qquad (3.5)$$
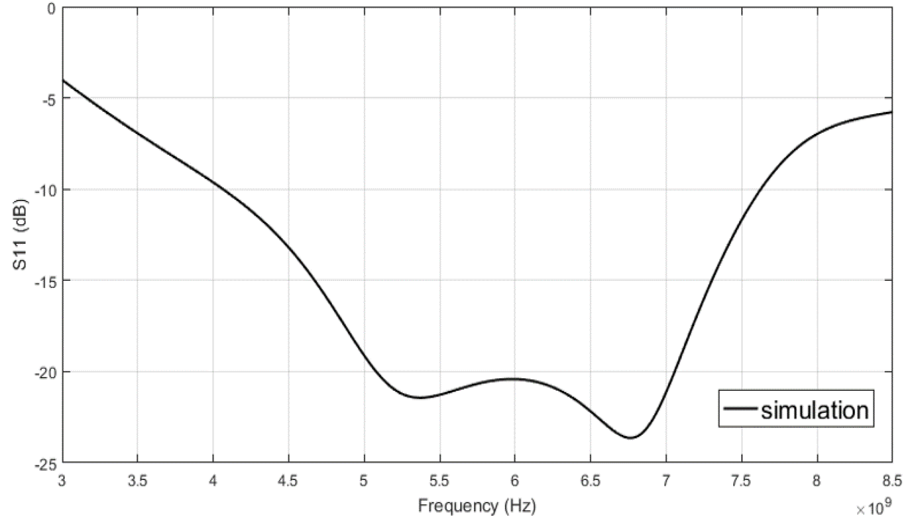
Figure 3.8. Simulation result of transmitter return-loss
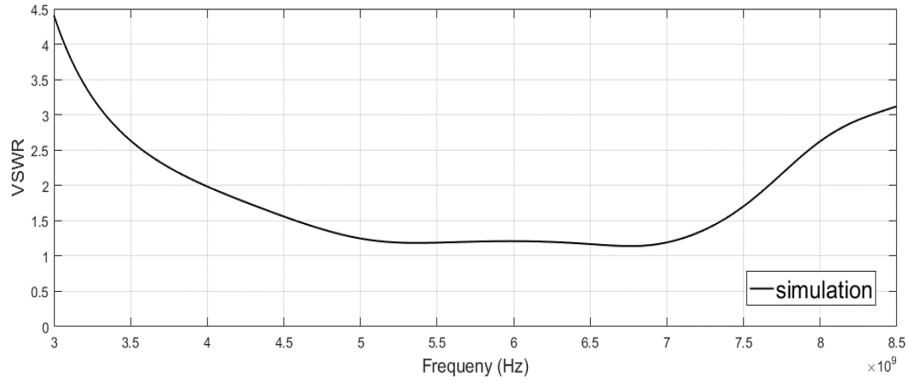
Figure 3.9. Simulation result of transmitter VSWR

$$D_{max} = D_0 = \frac{4\pi U_{max}}{P_{rad}} \tag{3.6}$$

where D is directivity (dimensionless), D_0 is maximum directivity , U is radiation intensity (W/unit solid angle), U_{max} is maximum radiation intensity, U_0 is radiation intensity of isotropic source and P_{rad} is the total radiated power (W). Additionally, gain is defined as "the ratio of the intensity, in a given direction, to the radiation intensity which is obtained if the power accepted by antenna were radiated isotropically." (Balanis, 2005).

$$Gain = 4\pi \frac{U(\theta, \phi)}{P_{in}} \left(dimensionless\right) \tag{3.7}$$

$$P_{rad} = e_{cd} P_{in} \left(dimensionless\right) \tag{3.8}$$

where P_{in} is total input power, e_{cd} is antenna radiation efficiency. Another definition for gain is absolute gain , that "takes into account the reflection/mismatch losses." For results

34
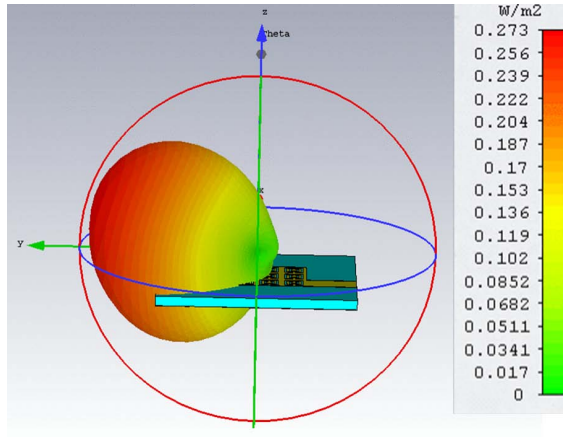
Figure 3.10. 3D power radiation pattern of Tx antenna.(Source: Önder Yılmaz and Yaman, 2018a)

(a)   (b)
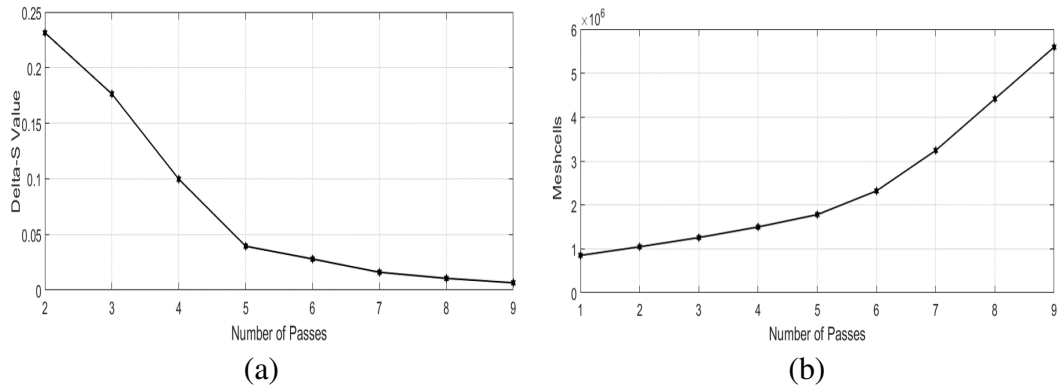
Figure 3.11. (a)Delta s value (b)Total number of meshcells

of the thesis, gain refers to absolute gain.

$$G_{abs}(\theta, \pi) = (1 - \mid \Gamma \mid^2 G(\theta, \phi)) = e_0 D(\theta, \phi) \tag{3.9}$$

where e_0 is the overall antenna efficiency;

$$e_0 = e_r e_{cd} = e_{cd}(1 - \mid \Gamma \mid^2) \tag{3.10}$$

Besides, absolute maximum gain related to maximum directivity;

$$G_{oabs} = e_0 D_0 \tag{3.11}$$

Realized absolute gain patterns for horizontal and vertical polarizations (Figure-3.12) clearly verify the expected patch plane axis radiation and minimized back and side lobes so that efficiency of proposed antenna is a bit higher than classical patch antenna as assumed, (R.Garg and A.Ittipiboon, 2001).

35
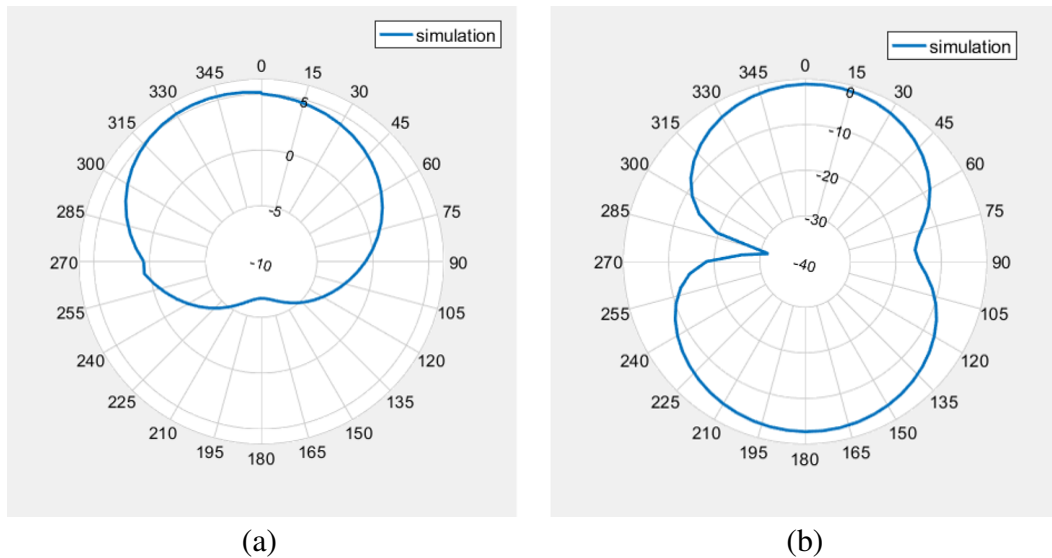
Figure 3.12. 5.8 GHz gain radiation pattern (a) Horizontal (b) Vertical

The main lobe of beam is the zone around direction of maximum radiation occurred. Further, usually the main-lobe area is bounded where within -3dB from the peak of main-beam. However, the side-lobes are "smaller beams that are outlying the main-beam and those are generally unwanted radiation is not aimed directions and never able to be completely exterminated". For horizontal result, gain can exceed value of 5.5 dB with wide beam-width and have just insignificant back and side lobes. Whereas, vertical result has two main lobes and the larger one cause unwanted radiation in reverse direction. Fortunately, vertical polarization has very weak gain values which is below than zero. Therefore, it can have just a slight effect on efficiency of antenna.

For both horizontal and vertical polarizations, normalized power radiation patterns for some frequencies from radiation spectrum (for simulation result, it is between 4 GHz and 7.6 GHz) are given in Figures-3.15-3.16. Normalized radiation patterns expose that expected radiation parallel to patch plane is provided around the 5.8 GHz, and further frequencies have radiation in different directions. Different main lobe directions depending on frequency might be suitable for specific applications. Realized gain and 3dB beam-width depending on the frequency curves are given in Figure-3.13 and Figure-3.14, respectively. Although gain of proposed antenna is similar to typical patch antennas, when 3 dB beam-width is taken into account, the difference is revealed for simulated antenna that is very wide radiation provided mostly around $100°$ at 5.8 GHz with smaller size.
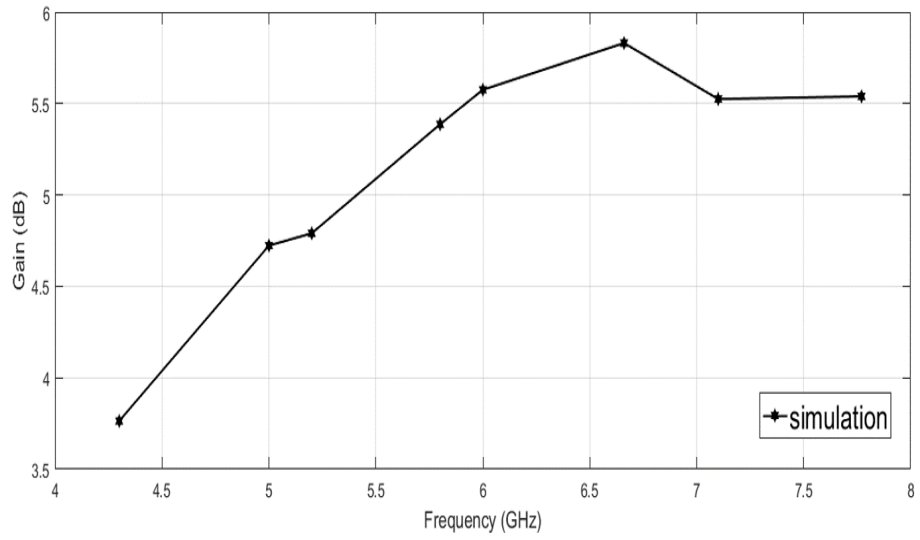
Figure 3.13. Maximum gain versus frequency for simulated transmitter antenna
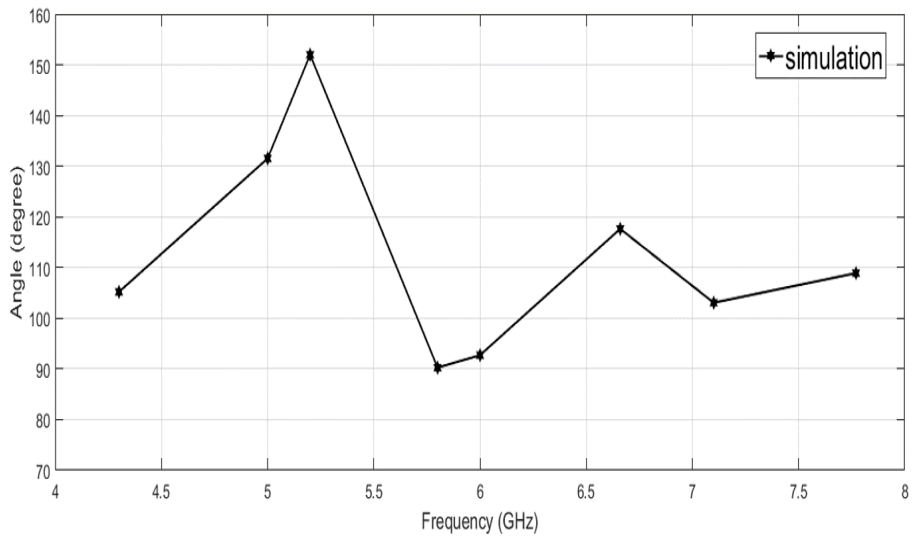
Figure 3.14. 3 dB beam-width versus frequency for simulated transmitter antenna
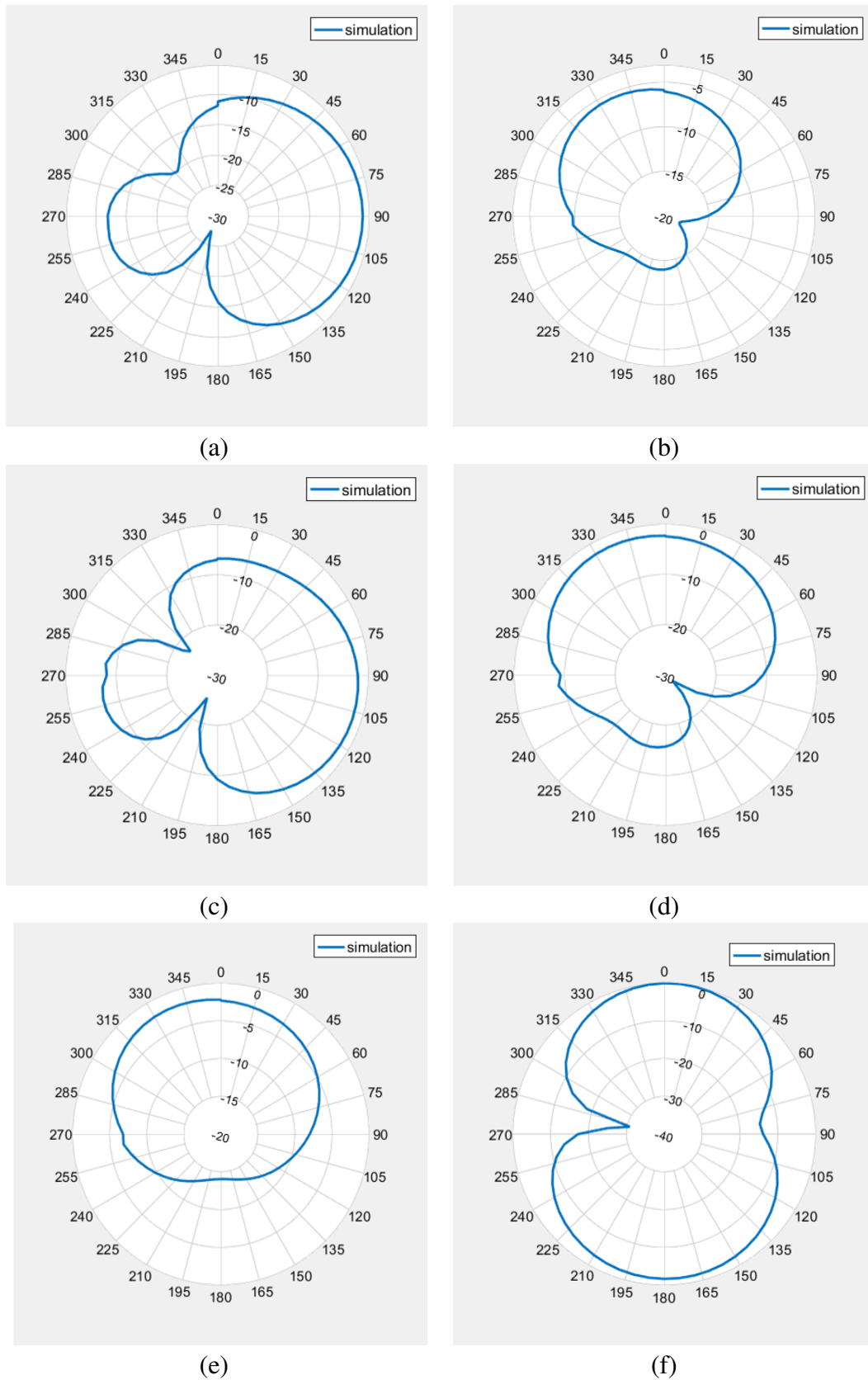
Figure 3.15. Normalized radiation patterns (a) 4.3 GHz Horizontal (b) 4.3 GHz Vertical (c) 5.0 GHz Horizontal (d) 5.0 GHz Vertical (e) 5.8 GHz Horizontal (f) 5.8 GHz Vertical
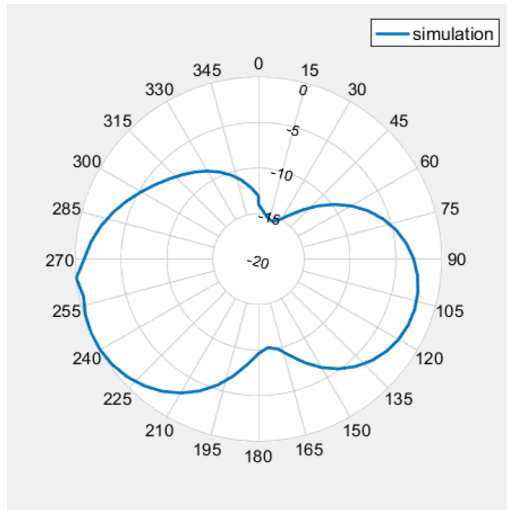
(a)
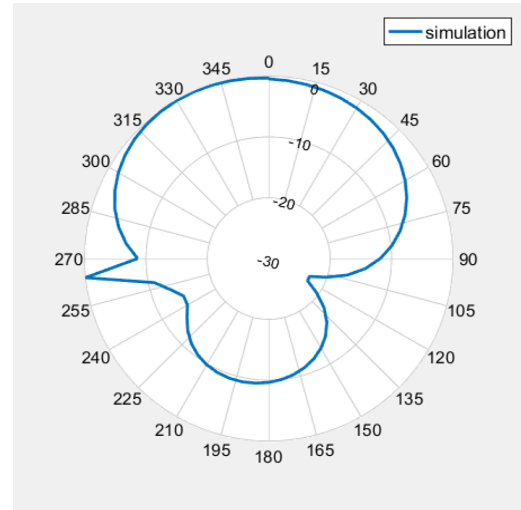
(b)
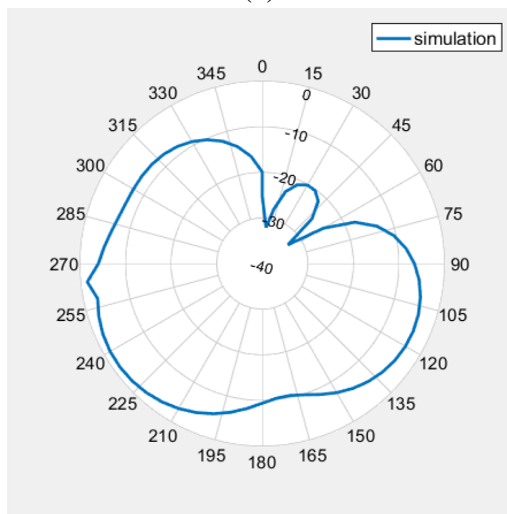
(c)
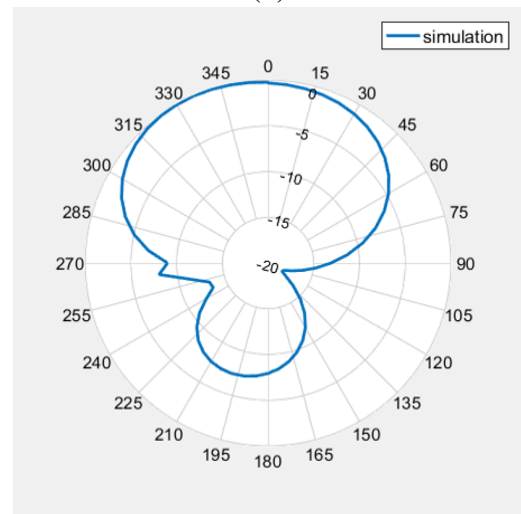
(d)

Figure 3.16. Normalized radiation patterns (a) 6.6 GHz Horizontal (b) 6.6 GHz Vertical (c) 7.1 GHz Horizontal (d) 7.1 GHz Vertical

3.1.1. Anechoic Chamber Measurements

Before starting a measurement in anechoic chamber, return loss and voltage standing wave ratio of both Tx/Rx antennas are measured via Agilent 8720D Vector Network Analyzer (VNA) which sweeps frequencies from 50 MHz to 20 GHz with ± 0.1 dB accuracy. Picture of VNA is given in Figure-3.17.

Figure 3.17. Agilent 8720D vector network analyzer

Radiation pattern and gain measurements of printed antennas are taken in the anechoic chamber laboratory of Izmir Institute of Technology in Turkey. Anechoic chamber is a room designed to completely absorb reflections of electromagnetic waves and its outer wall are covered by steel sheets and its inside surfaces have special lining with RF absorbing material such as ferrite and pyramidal Styrofoam. Instruments used during the measurement in anechoic chamber, are listed in Table-3.1.

Table 3.1. Instruments of anechoic chamber

Device Model	Explanation
HP 83620B	Swept Signal Generator
HP 8565E	Spectrum Analyzer
SAS-571	Reference Horn Antenna (2)
Innco DS-1200	Turntable
Innco CO 1000	Controller
Asus K50In Series	Computer (LabView Software installed)

Figure 3.18. Anechoic chamber in IZTECH Laboratories

Horizontal (XY) and vertical (XZ) polarization measurements are done by using reference horn antenna supplied by signal generator at the transmitter side. Realized antennas are placed on turntable and received signal are measured by spectrum analyzer under control of turn table and controller. Necessary data were recorded in computer at the each angle degree so that received signal versus angle vector is obtained, and then radiation pattern plot is displayed via MATLAB software. Anechoic chamber picture is shown in Figure-3.18 Antenna absolute or realized gain is a key performance value which combines the antenna's directivity and efficiency. In a transmitting antenna, the gain describes how well the antenna converts input power into radio waves headed in a specified direction. In a receiving antenna, the gain describes how well the antenna converts radio waves arriving from a specified direction into electrical power. In order to measure gains of realized antennas, firstly two reference antenna already having gain versus frequency information, are performed in same setup, then realized antennas are replaced instead of receiver reference antenna and measurement are taken again. Realized gain can be found by using given equations, see (Balanis, 2005),

$$G_{AUT} + G_0 = 20 \log_{10}(\frac{4\pi R}{\lambda}) + 10 \log_{10}(\frac{P_{AUT}}{P_0}) \tag{3.12}$$

$$G_{REF} + G_0 = 20 \log_{10}(\frac{4\pi R}{\lambda}) + 10 \log_{10}(\frac{P_{REF}}{P_0}) \tag{3.13}$$

$$G_{AUT} = G_{REF} + 10\log_{10}(\frac{P_{AUT}}{P_{REF}}) \tag{3.14}$$

where G_{AUT} is gain of antenna under test in dB, G_{REF} is gain of reference antenna in dB and G_0 is gain of transmitting antenna in dB.
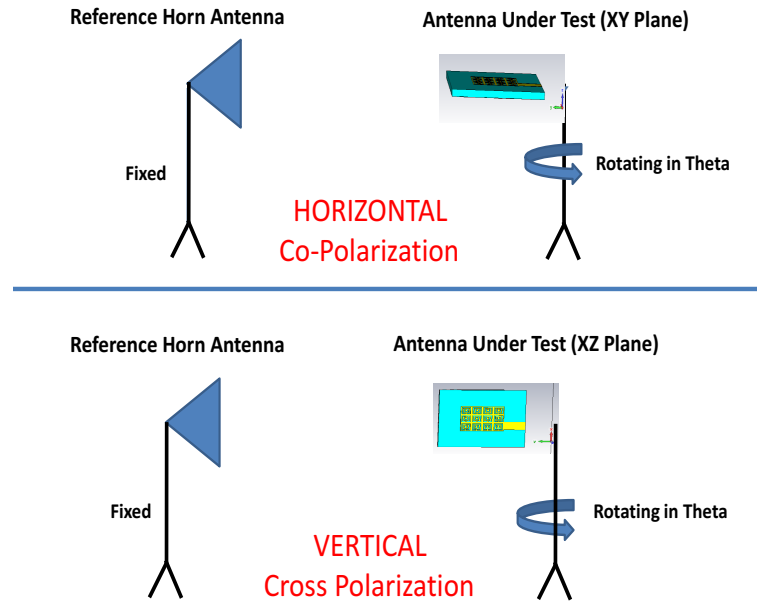
Figure 3.19. Horizontal and Vertical Measurement Setups

In radiation pattern results, horizontal (XY-Plane) and vertical (XZ-Plane) polarizations refer to co-polarization and cross polarization, respectively. Figure-3.19 illustrate these two different polarizations measurement setups.

3.1.2. Measurement Results of the Realized Transmitter Antenna

Realized transmitter antenna with SMA connector and closer view for single CSRR and meshgrid ground are given in Figure-3.20 and Figure-3.21.

Due to fabrication process, dimension of etched gap in CSRRs structures might differ slightly from the simulated one and it may cause some differences in measurement results comparing to simulations.

Return-loss curve of realized antenna (Figure-3.22) shows very broadband radiation characteristic where the -10 dB cut-off frequency starts from ≈ 3.7 GHz up to 7.8 GHz. It can be also seen from voltage standing-wave ratio (VSWR) result (Figure-3.23).
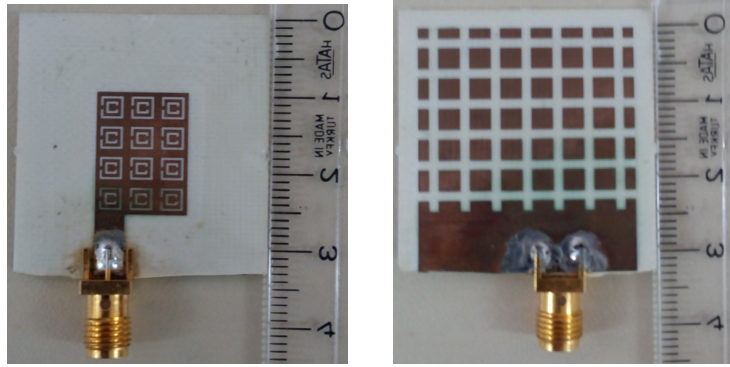
Figure 3.20. Pictures of realized transmitter antenna, top view (left) and bottom view (right).
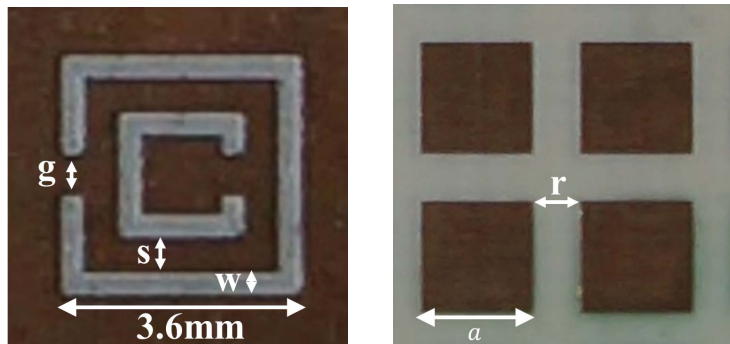
Figure 3.21. Pictures of single CSRR (left) and meshgrid ground (right). Dimensions; ($w = s = 0.35 \ mm$, $g = 0.4 \ mm$, $a = 2.8 \ mm$, $r = 1.2 \ mm$)

Additionally, along the entire band, return loss is held in very low level that is mostly below than -20 dB. Realized gain patterns for horizontal and vertical polarizations which are given in Figure-3.24) emphasize that maximum gain can reach 6.5 dB whereas 3db beam-width is $\approx 60°$. Maximum gain at 5.8 GHz is somewhat higher when comparing to typical patch antenna it is approximately about to 5 dB, (R.Garg and A.Ittipiboon, 2001). Although higher maximum gain is achieved when it is compared to typical patch and even simulation result of proposed transmitter, quite level of unwanted side and back lobes decrease the efficiency of the realized antenna.Normalized radiation patterns for the same frequencies which are selected for simulation results, are illustrated in Figures-3.25-3.26. Normalized power radiation patterns reveal that as frequency of radiation changes, direction of the main lobes also change and at lower frequencies, side and back lobes are more suppressed so that radiation efficiency is highly increased.

Comparison between measurement and simulation results are given in Figures-
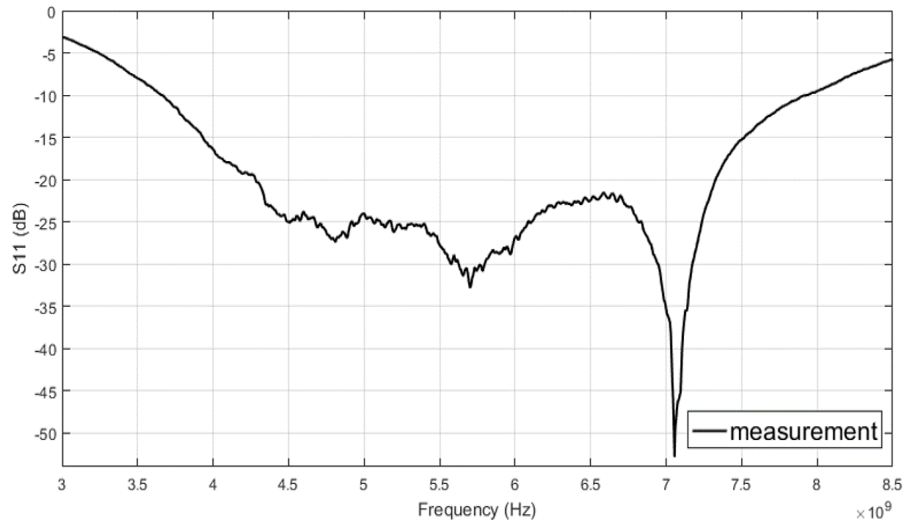
Figure 3.22. Measurement result of transmitter return-loss (S11) characteristic

3.27-3.30. It can be seen from return-loss characteristics (Figure-3.27) that the bandwidth below -10 dB cut-off is slightly larger for measurement compared to the simulation. Difference may be related to the fabrication tolerance for the complicated CSRR patterns or some missing parts in simulated design. However, that acceptable difference decreases especially for around desired 5.8 GHz frequency where the return-loss is very low for both. Consistency also can be seen in VSWR curve given in Figure-3.28. Comparative gain patterns which are given in Figure-3.29 show that simulated one is less directive and have higher 3-dB beam-width which is $\approx 90°$, whereas the measured one is more directive and its 3-dB beam width is $\approx 60°$. Furthermore, gain of the transmitter is obtained as 6.5 dB at 5.8 GHz. Interestingly a more consistent variations of simulations and measurements for the vertical polarization are observed. These patterns also show that the designed structure behaves as a traveling wave antenna due to backward wave propagation along the horizontal plane as a consequence of using left-handed medium. Hence the radiation occurs in horizontal direction plays the main role in our radar application. Comparative normalized radiation patterns are given in Figures-3.30-3.31-3.32. As a conclusion, it can be said that measured radiation patterns tendency are barely matched to simulated ones, whereas maximum gains differs especially when frequency difference to the desired frequency (5.8 GHz) increases. The reason might be fabrication tolerances as we discussed before.
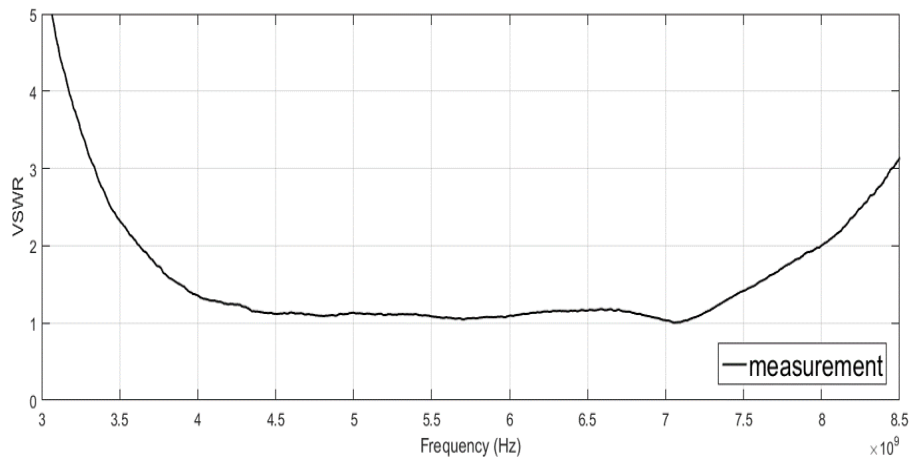
Figure 3.23. Measurement result of transmitter VSWR characteristic

(a)

(b)
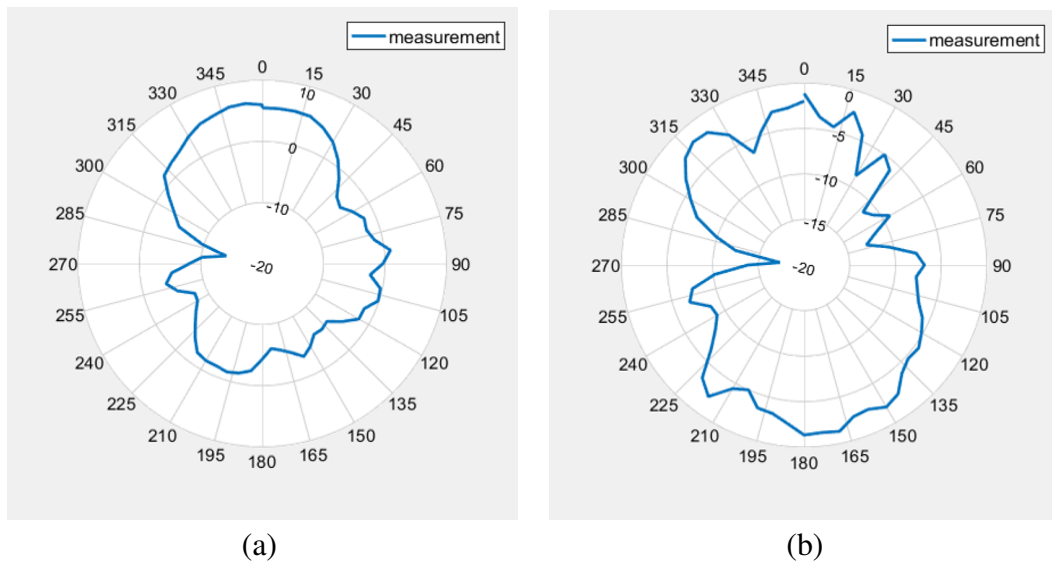
Figure 3.24. 5.8 GHz gain radiation pattern (a) Horizontal (b) Vertical
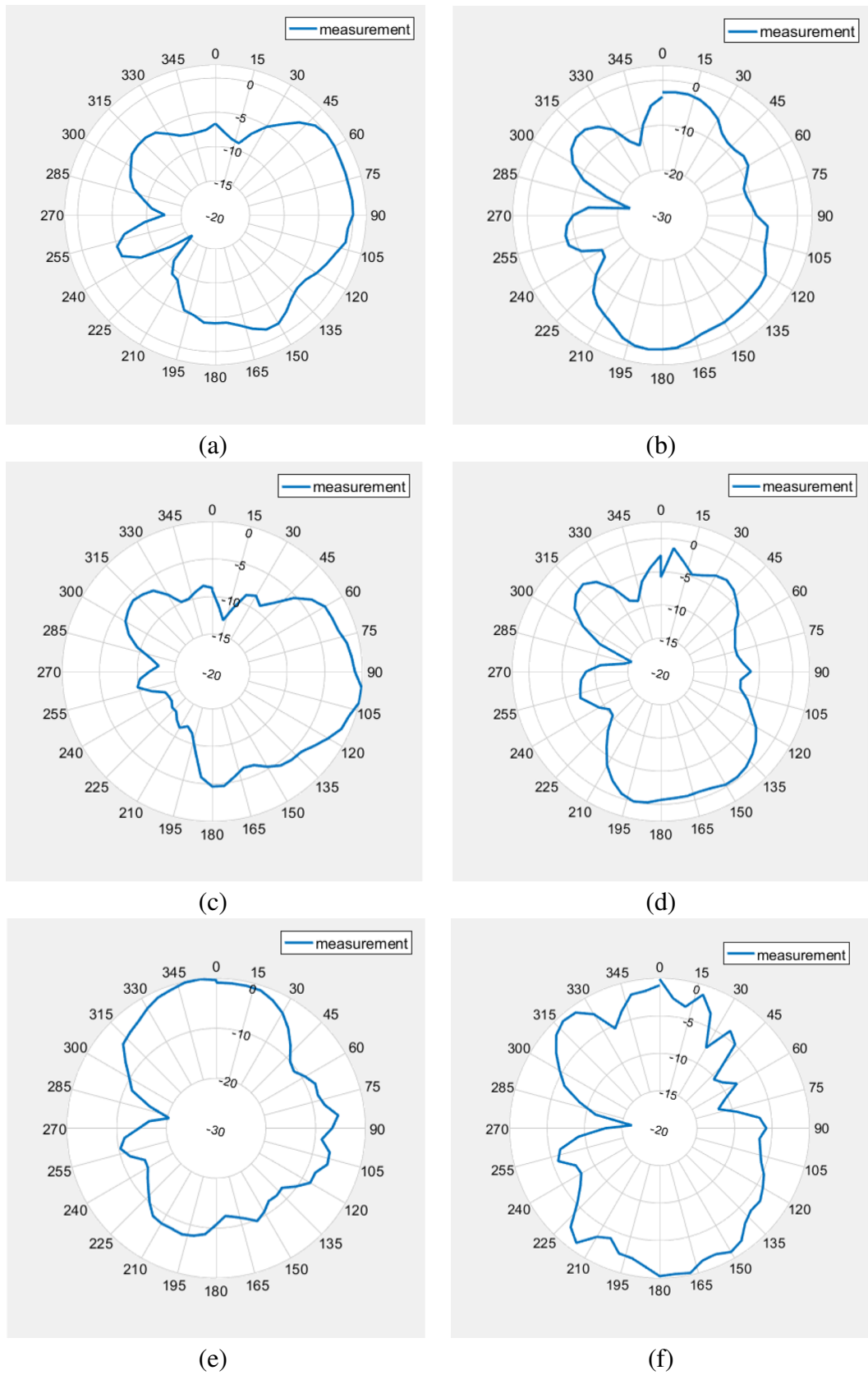
Figure 3.25. Normalized radiation patterns (a) 4.3 GHz Horizontal (b) 4.3 GHz Vertical (c) 5.0 GHz Horizontal (d) 5.0 GHz Vertical (e) 5.8 GHz Horizontal (f) 5.8 GHz Vertical
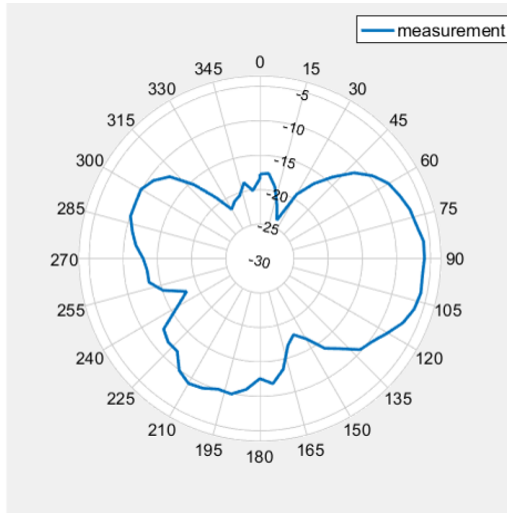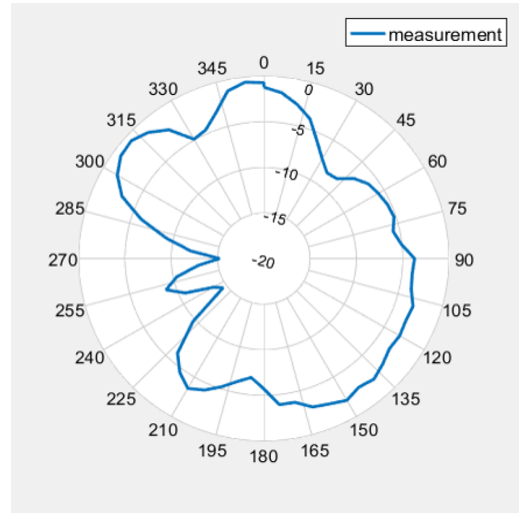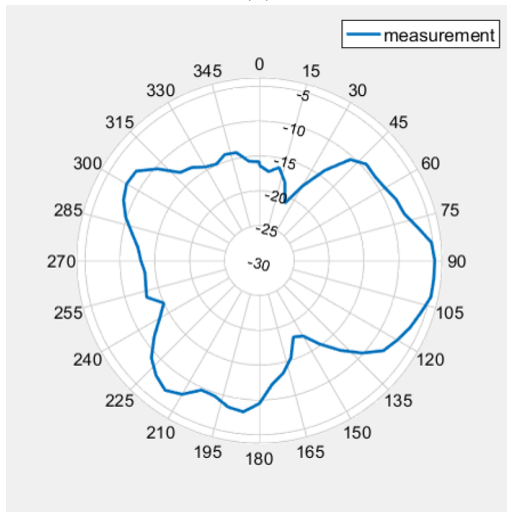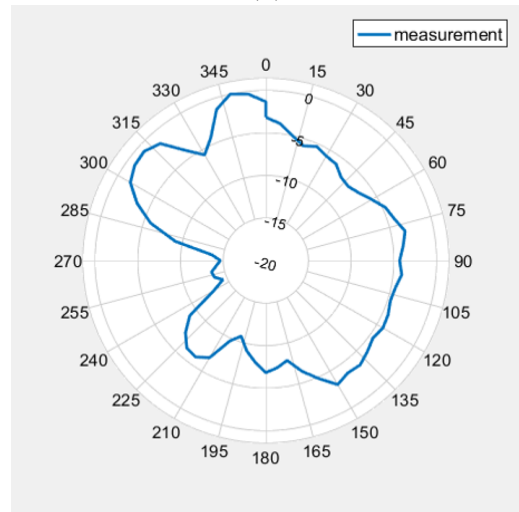
Figure 3.26. Normalized radiation patterns (a) 6.6 GHz Horizontal (b) 6.6 GHz Vertical
(c) 7.1 GHz Horizontal (d) 7.1 GHz Vertical
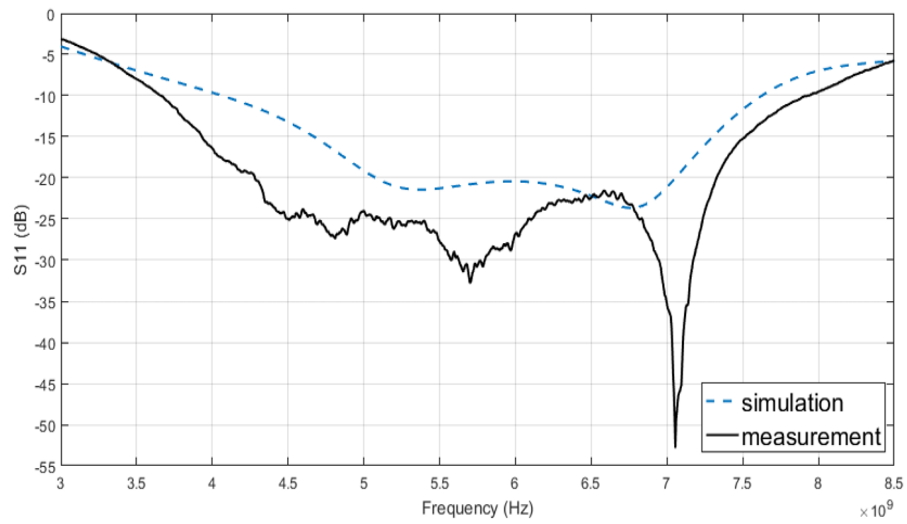
Figure 3.27. Comparison of simulation and measurement return losses
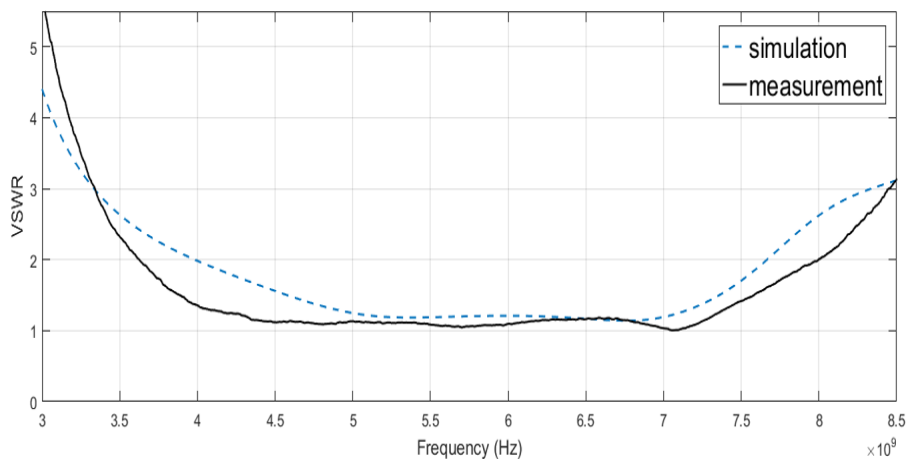
Figure 3.28. Comparision of measurement and simulation VSWR
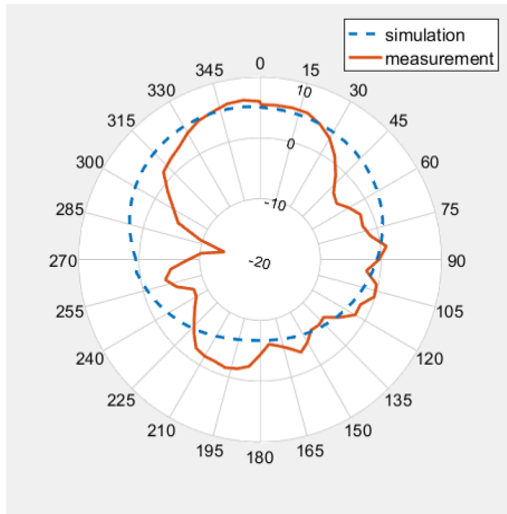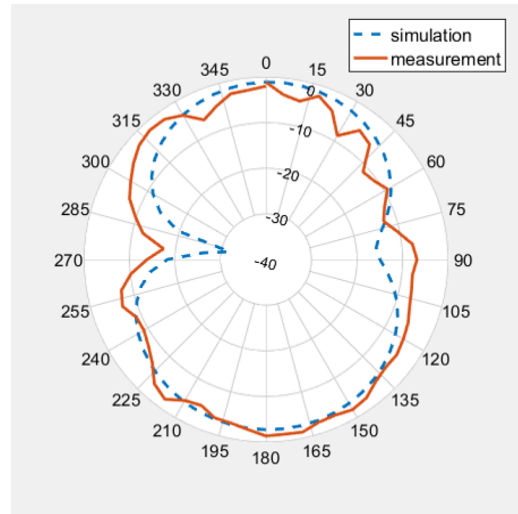
Figure 3.29. 5.8 GHz gain radiation pattern (a) Horizontal (b) Vertical
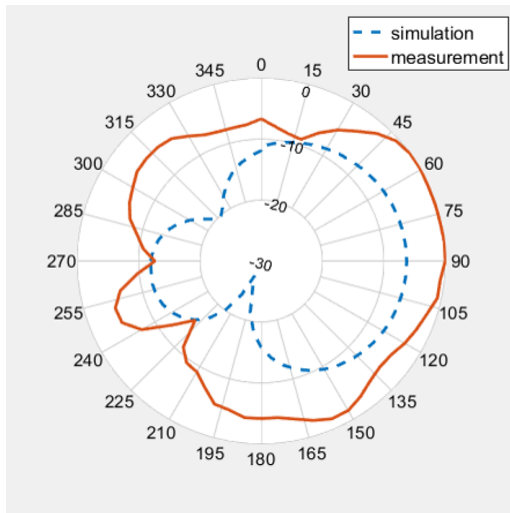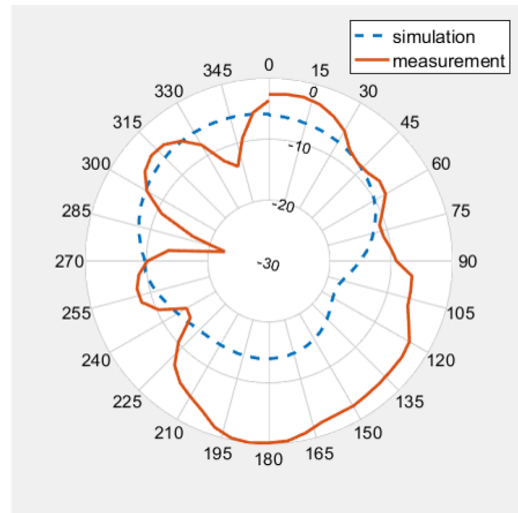
Figure 3.30. Normalized radiation patterns (a) 4.3 GHz Horizontal (b) 4.3 GHz Vertical
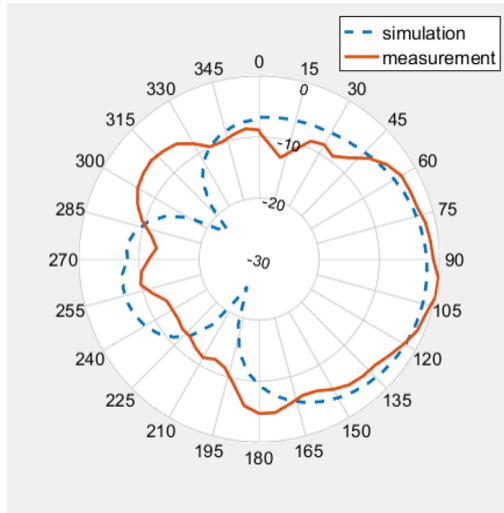
(a)
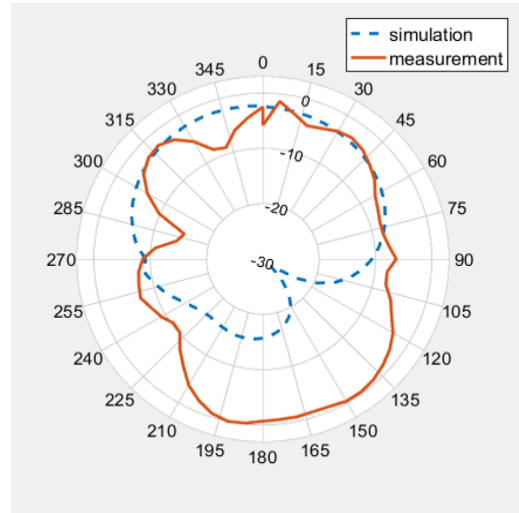
(b)
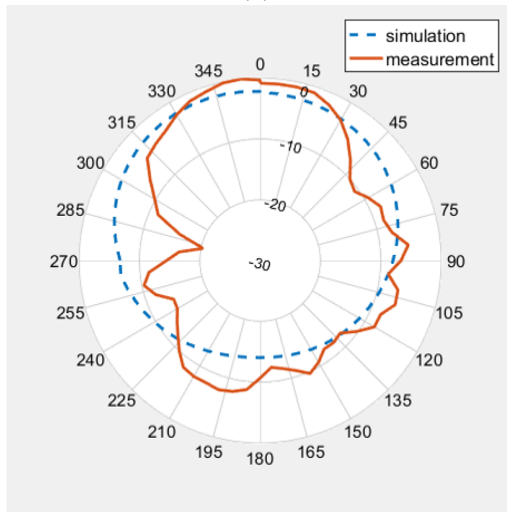
(c)
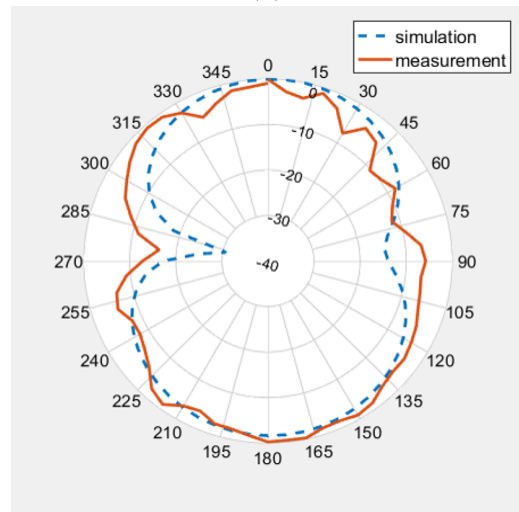
(d)

Figure 3.31. Normalized radiation patterns (a) 5.0 GHz Horizontal (b) 5.0 GHz Vertical (c) 5.8 GHz Horizontal (d) 5.8 GHz Vertical
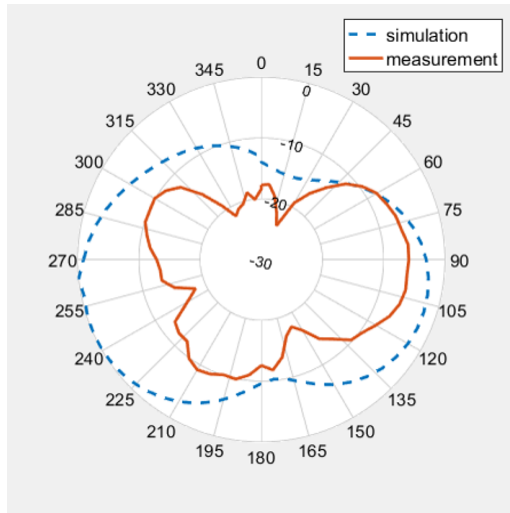
(a)
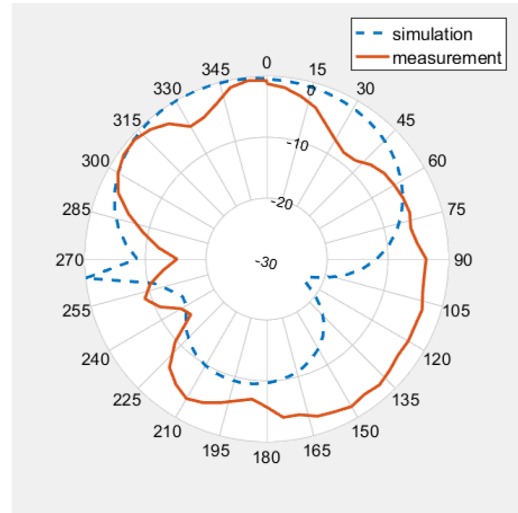
(b)
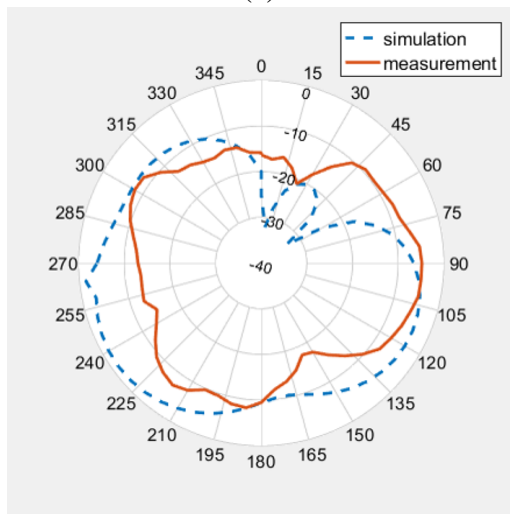
(c)
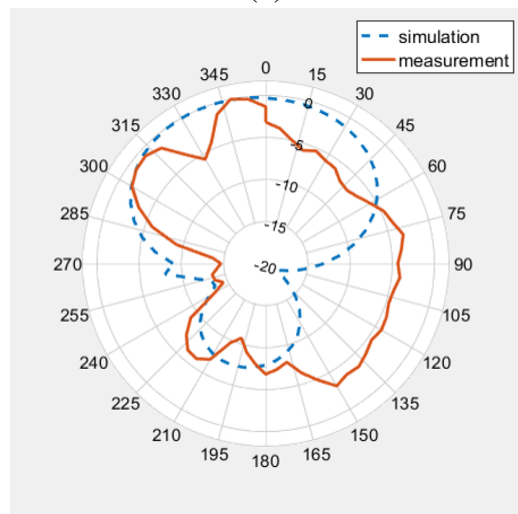
(d)

Figure 3.32. Normalized radiation patterns (a) 6.6 GHz Horizontal (b) 6.6 GHz Vertical
(c) 7.1 GHz Horizontal (d) 7.1 GHz Vertical

3.2. Receiver Antenna Design: Near-Zero Index Metamaterial Antenna

The study of Pendry et al. (J. B. Pendry and Youngs, 1996) as discussed in theoretical background chapter, about on modeling low frequency plasmon bounded by a metallic wire cage at the interface of dielectrics, opens a wide area for metamaterial structures in microwaves, terahertz and optical spectrum. According to the mentioned study, it is possible that plasma frequency can be lowered extremely by using a highly conducting thin wire lattice and a dielectric boundary structure excited by electric field. Metamaterials are engineered with the help of extremely low plasma frequency, which provide negative permittivity and near-zero permittivitiy at certain frequency band from optical to microwave spectrum. This lattice structure can be designed by using its lattice constant which is the separation between wires and radius of thin wire as given in Eq.-3.15. However, it should to be considered that these dimensions should be much smaller than the wavelength of excitation wave. This unnatural property of this certain materials can lead to many interesting phenomena and applications such as highly directive antennas as mentioned in introduction chapter. As a summary, near-zero index metamaterials enhance tunneling of uniform fields in a zero electric permittivity medium, or reflection behavior of the compressed electromagnetic wave so that they can be employed advances in shielding or cloaking technologies (Pendry, 2000; D.Schuring and D.R.Smith, 2006). Among the recent studies, high directivity antenna studies by using the metamaterial concept received big attention recently in microwave applications. As a summary of Pendry's study presented in (J. B. Pendry and Youngs, 1996), that plasma frequency of such a meta-structure given as,

$$\omega_p^2 = \frac{2\pi c_0^2}{a^2 \ln(a/r)} \tag{3.15}$$

where ω_p is the plasma frequency, c_0 is the speed of light in vacuum, a is the lattice constant and r is the radius of wire. For such a conducting material, effective permittivity ϵ_{eff} can be written as,

$$\epsilon_{eff} = 1 - \frac{\omega_p^2}{\omega(\omega + j\epsilon_0 a^2 \omega_p^2/\pi)r^2\sigma}, \tag{3.16}$$

where σ is the conductivity of metal, ω is the frequency of excitation wave, $\epsilon_0 = 8.854 \times 10^{-12} \ F/m$ is the free space permittivity. Propagation constant K,

$$K = \omega \frac{\sqrt{\epsilon_{eff}}}{c_0} = \frac{\sqrt{\omega^2 - \omega_p^2}}{c_0}. \qquad (3.17)$$

According to these equations, the effective permittivity can be negative when the frequency is below ω_p. Another fascinating situation, if excitation frequency is selected just above the plasma frequency, effective permittivity can be less than positive one. This means optical index is less than one, so it can go further very close to zero. If optical index of slab is very small, the radiated field will be concentrated around normal.

In the proposed antenna, instead of three-dimensional (3D) volumetric lattice, the slabs consist of printed planar thin wire lattice on both top and bottom, are considered due to their simplicity. It should be noted that the vertical wires have a negligible or very weak influence on the dimensions of lattice due to parallel alignment to the radiated beam direction, see (Stefan Enoch and Vincent, 2002). Accordingly, a near-zero epsilon or near-zero index structure given in Figure-3.35 is designed. Back side of the substrate has the same pattern of cross-conductor. The width of conductors ρ, and periodicity distance between them called as lattice constant, ℓ, are calculated via Eq.-3.15 to obtain a certain zero permittivity at 5.8GHz which is expected to provide plasma frequency in the desired operating frequency. Then they are optimized by using CST:MW. Afterwards, three near-zero index slabs are placed above patch antenna for the purpose of confining the radiated beam into a narrow angle in the direction of antenna plane's normal vector, whereas classical patch can provide much wider beam-width with low antenna gain. Parameters of the near-zero index slabs which are placed over patch antenna are optimized with the help of the simulator until results reach to the desired gain, bandwidth and beam-width characteristic. Number of near-zero index layers which are attached properly to each other, is increased until the simulation results reach the desired point. Although larger number of layers makes the antenna more directive and narrow beam-width, this relation is not linear and after some point, its effects on antenna become very slight. On the other hand, more layers cause a larger and bulky antenna in terms of size and practicality. Meanwhile, impedance matching must be always considered due to coupling between near-zero layers and patch, even if microstrip line is used for feeding of patch. As a result of simulations, three optimized layers are joined together and put upon, then placed above the designed typical rectangular patch antenna with parasitic components, whose substrate is Roger $4730JXR$ ($\epsilon_r = 3.00$) with $1.52mm$ thickness.

Afterwards, patch antenna without near-zero index slabs is optimized to operate at 5.8 GHz, then simulated results are recorded in order to compare with the case of placement of near-zero index layers. Figure-3.33 shows single patch antenna with parasitic

components on top view. The patch antenna is loaded by parasitic components in order to increase bandwidth and rectangular conductive strips are removed from patch part (both sides at end of microstrip line) for impedance matching by adjusting admittance of borderline. Dimensions also are indicated in the Figure-3.33, however it can be noticed that dimensions are slightly different than case of final design with placed near-zero layers. In this way, similar radiation characteristic at 5.8 GHz is obtained to realize the influences of near-zero index medium on radiation beam. Additionally, some optimizations are required to avoid impedance missmatch due to coupling effects of near-zero layers placed above 19 mm.
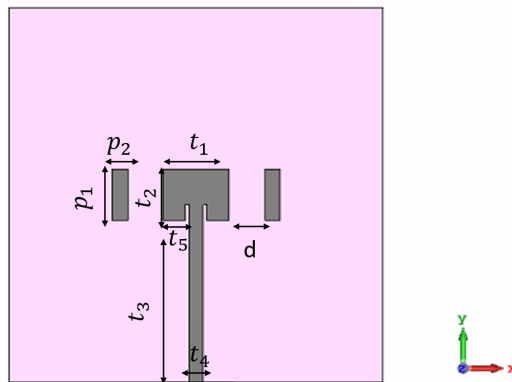
Figure 3.33. Simulated single patch part of Rx antenna (p_1 = 13.56 mm, p_2 = 3.86 mm, t_1 = 17.56 mm, t_2 = 13.56 mm, t_3 = 45.73 mm, t_4 = 3.87 mm, t_5 = 7.78 mm, d=16 mm)
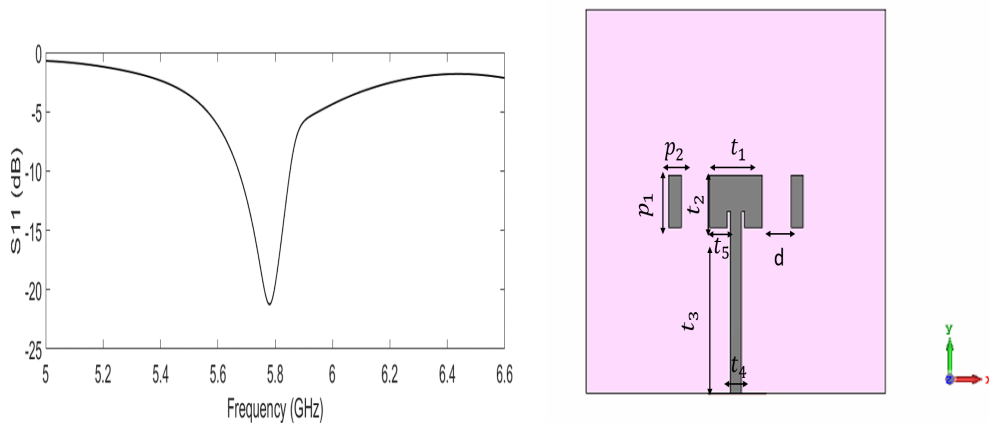
Figure 3.34. Return-loss (S11) of single patch of receiver(left) and gain pattern (right)

Return loss and gain pattern of the single patch are given in Figure-3.34, and it can be seen from gain pattern, single patch provides very wide radiation which is $\approx 100°$ 3dB beam-width and has 6.5 dB maximum gain, as expected from typical patch antenna with parasitic components, see (R.Garg and A.Ittipiboon, 2001). Afterwards, optimized three near-zero layers are attached properly and placed 19 mm above the patch. Dimensions of the patch, parasitics and near-zero layers for receiver antenna, are indicated in Figure-3.35.
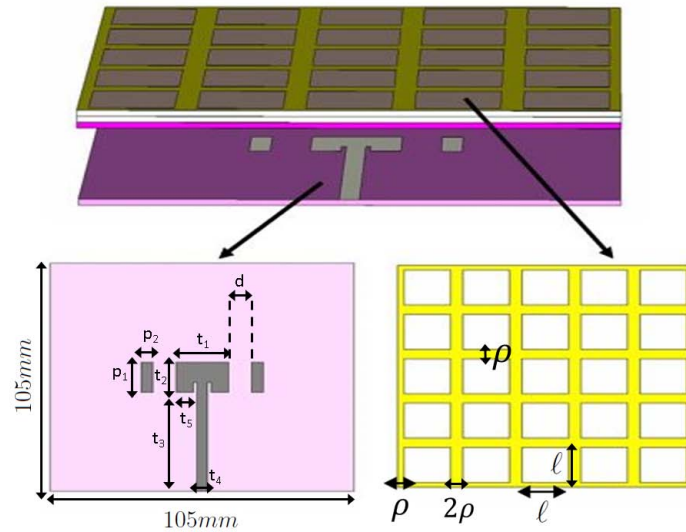
Figure 3.35. Simulated receiver (Rx) antenna ($p_1 = 13.96\ mm$, $p_2 = 4.02\ mm$, $t_1 = 17.96\ mm$, $t_2 = 13.96\ mm$, $t_3 = 45.73\ mm$, $t_4 = 3.87\ mm$, $t_5 = 7.98\ mm$, d=8 mm, $\rho = 2.2\ mm$, $\ell = 16.6\ mm$)

Height between patch and near-zero slab is determined as $19mm$ after several simulation process and considering the impedance matching. It is also observed that the closer placement, the better results in terms of directivity. According to simulation results, return-loss and voltage standing wave ratio (VSWR) are given in, Figure-3.36 and Figure-3.37. After several optimization process, the intended return-loss characteristic with minimal reflected loss at operation frequency (5.8 GHz) is acquired as clearly seen in S11 curve. Further, VSWR graph demonstrates highly acceptable performance at 5.8 GHz where the VSWR is very close to value of 1.

The same computer (HP-Z820 Workstation) which was used to characterize transmitter antenna, was used to perform the receiver simulations. Convergent curve according to number of passes and related mesh-cells curves are given in Figures-3.38. Frequency domain solver with tetrahedron meshcells are employed during the simulations.
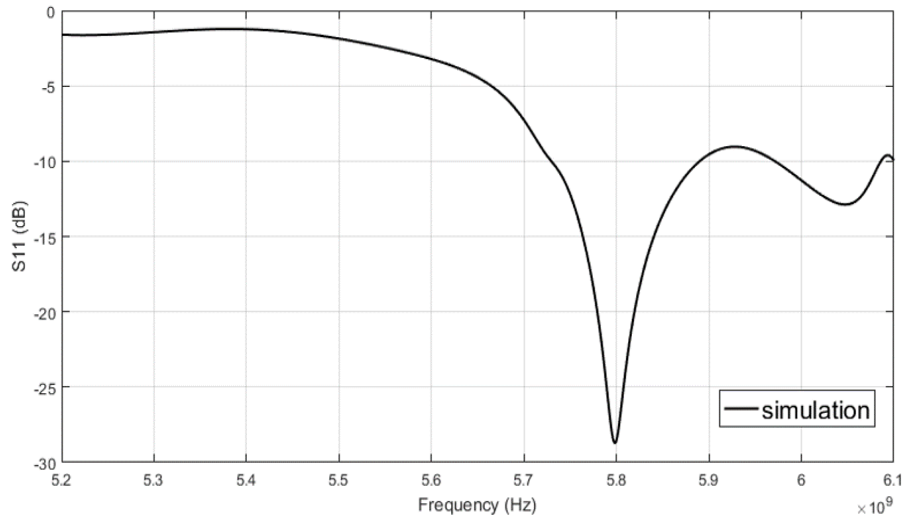
Figure 3.36. Return-loss versus frequency for simulation of receiver antenna
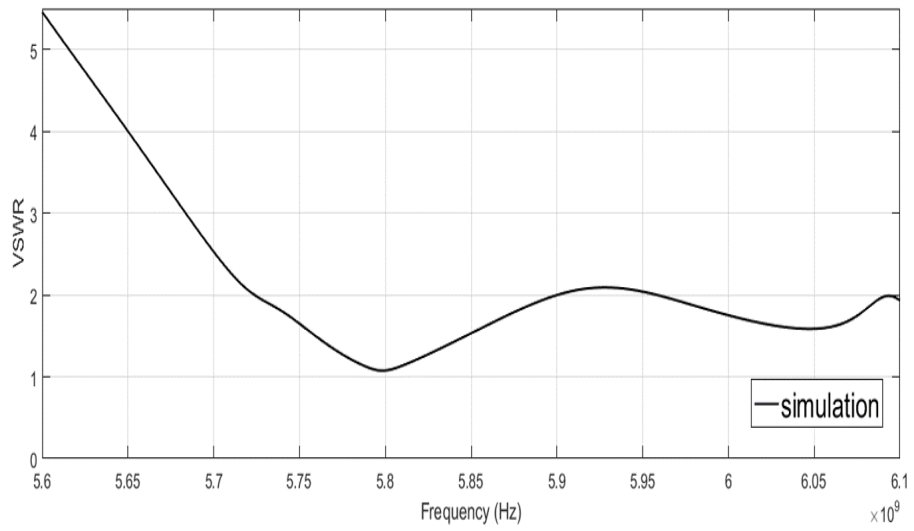
Figure 3.37. VSWR curve of receiver antenna

(a)

(b)
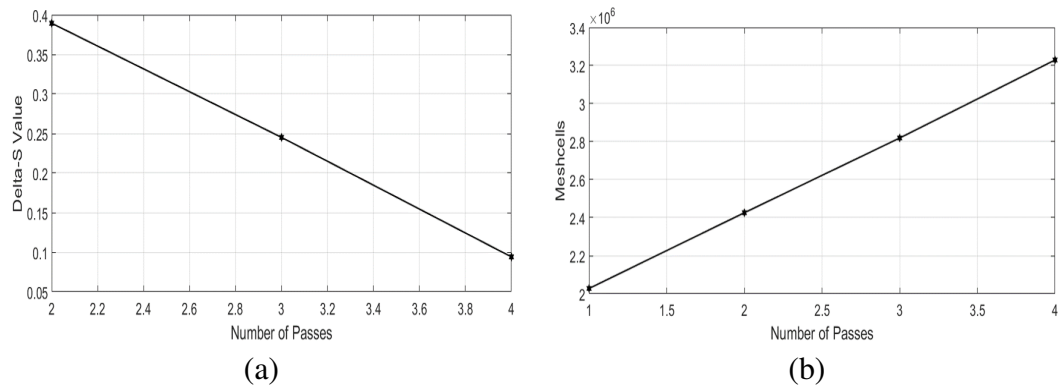
Figure 3.38. (a)Delta s value (b)Total number of meshcells

(a)

(b)
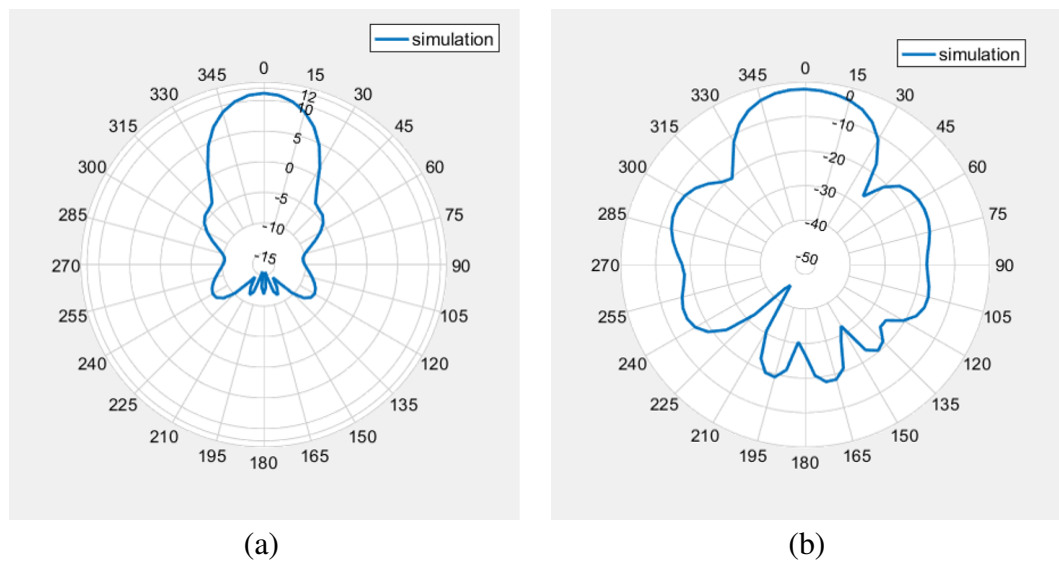
Figure 3.39. 5.8 GHz gain radiation pattern (a)Horizontal (b)Vertical

Simulated gain patterns of the receiver antenna at operating frequency 5.8GHz are shown in Figure-3.39 for horizontal and vertical polarization. If the gain characteristic of the horizontal is compared to single patch result (Figure-3.34), it can be seen that near-zero index layers tailor the radiated beam and allow electromagnetic wave propagation in a narrow incident angle according to Snell's law, see (Schwartz and Piestun, 2003). Additionally, highly directive main lobe can be seen without any significant back and side lobes. Gain can reach 11.35 dB at 5.8 GHz. However almost omni-directional characteristic is observed in the vertical polarization result with very low gain in every direction. 3D linear radiated power intensity figure is obtained via the frequency domain simulation, which signifies the directive characteristic of receiver antenna, in Figure-3.40. Maximum realized gain for the selected frequency points are given in Figure-3.41. Accordingly, the

57

designed antenna reaches maximum gain at 5.9 GHz, which is $11.8\ dB$,and it has the gain value $\approx 11.35\ dB$ at the operating frequency 5.8GHz.In addition to gain polar pattern, for 5.8GHz, cartesian graph where the x-axis refers to angle and y-axis refers to gain, is given in Figure-3.42 in order to see precisely 3-dB beam-width of receiver.
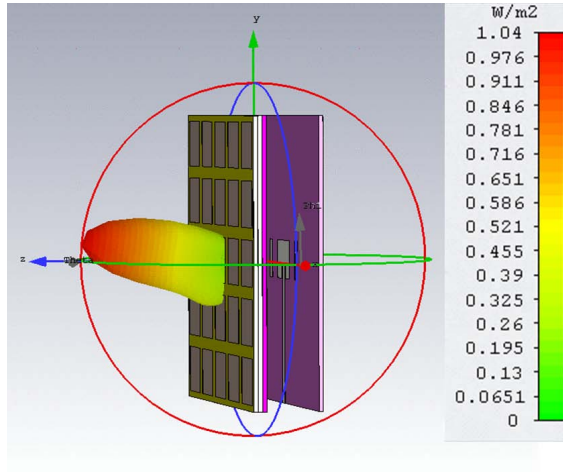
Figure 3.40. 3D power radiation pattern of Rx antenna, from (Önder Yılmaz and Yaman, 2018a)
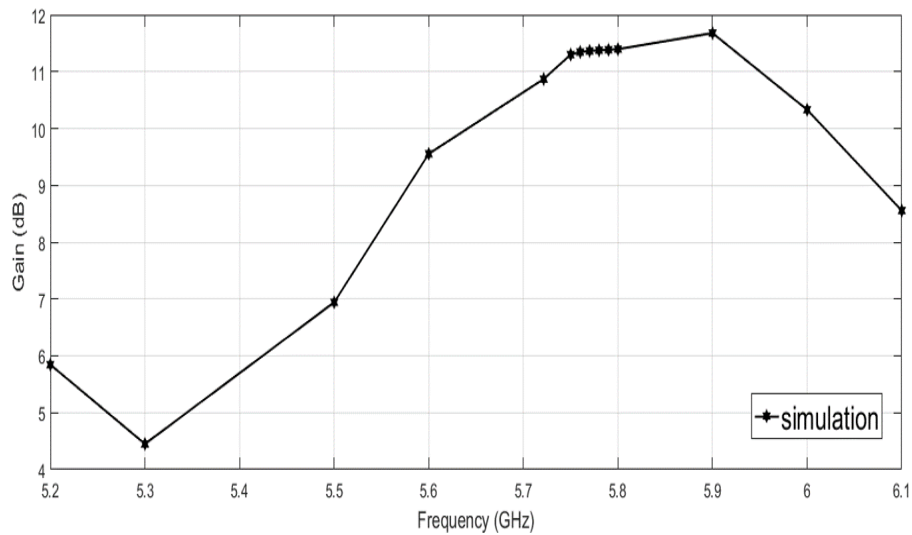
Figure 3.41. Maximum gain versus frequency

Furthermore, calculated 3dB beam-width values for frequency points are plotted in Figure 3.43. As a definition, 3dB beam-width/half power beam-width, is the angular separation in which the magnitude of the radiation pattern decrease by %50 or (-3dB) from the peak of the main beam. Lowest 3dB beam-width is the main aim in the design of the
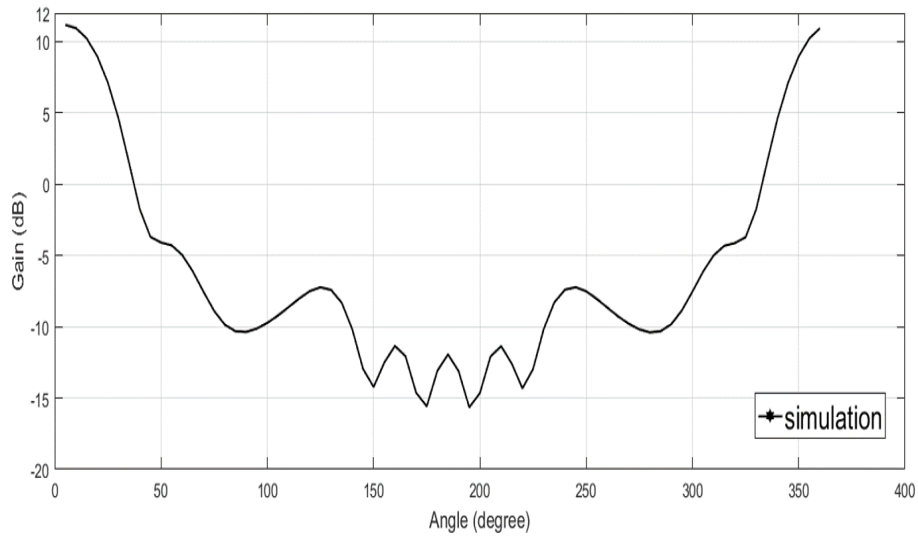
Figure 3.42. Simulation result of gain versus angle at 5.8 GHz

receiver for the proposed radar system, since a narrow beam-width increases accuracy of the information for a possible moving target position. Additionally, much smaller beam-width with low-losses i.e. reflection loss and losses due to conductivity or dielectric, generally makes antenna gain higher.
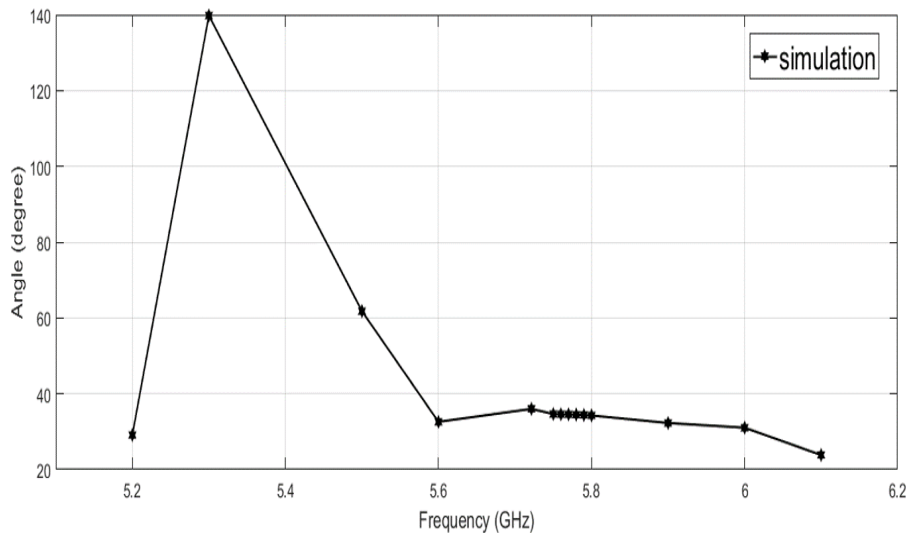
Figure 3.43. Simulation result of 3 dB beam-width

Additional results from simulation (Figure-3.44) include normalized radiation power intensity which reveals clearly polar distribution of radiation.

59

(a)   (b)
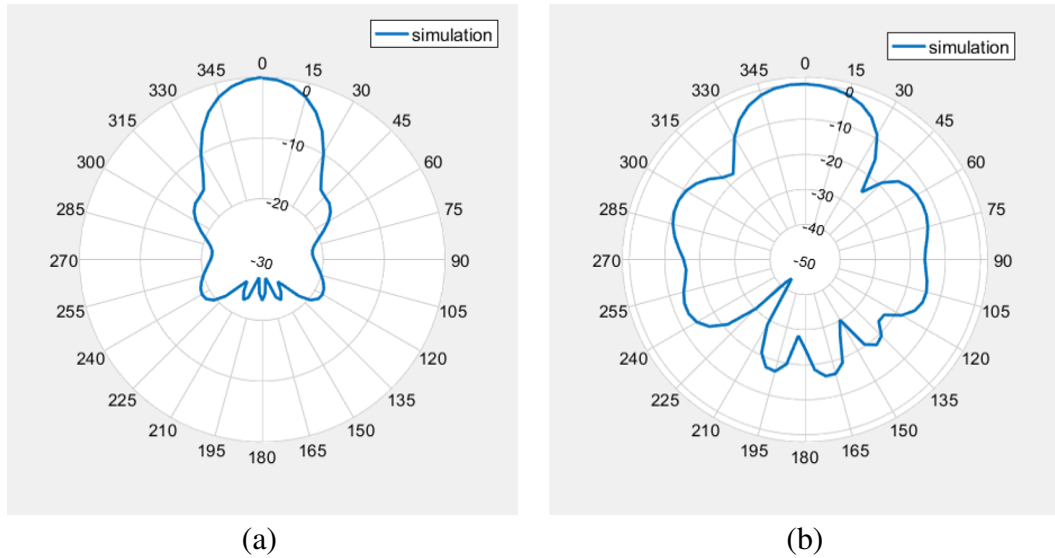
Figure 3.44. 5.8 GHz normalized radiation pattern (a)Horizontal (b)Vertical

3.2.1. Measurement Results of Realized Receiver Antenna

After designed receiver antenna results reaching the convergent criteria for the desired parameters, patch antenna portion and other three identical metamaterial slabs are manufactured and then they put in together as shown in Figure-3.45 by filling the gap between them with foam. A foam layer with the 19 mm thickness is located between patch and metamaterial layers and fixed with plastic stripes in the realized structure. Primary purpose of usage plastic stripes is to hold them in together, whereas it might be more important reason is to adjust the height between patch and near-zero slabs precisely by tighten them gradually. This process is performed while the network analyzer is measuring the return losses, in order to find exact result expected as simulation.
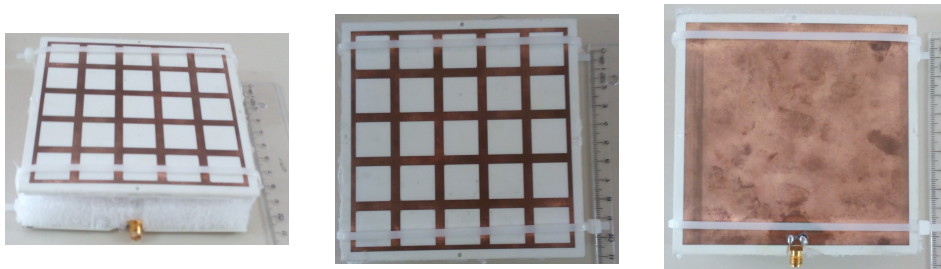
Figure 3.45. Realized receiver antenna views: perspective (left), top view of near-zero index slab(middle) and bottom ground layer of patch antenna(right)

The return loss and voltage standing wave ratio (VSWR) of the realized receiver
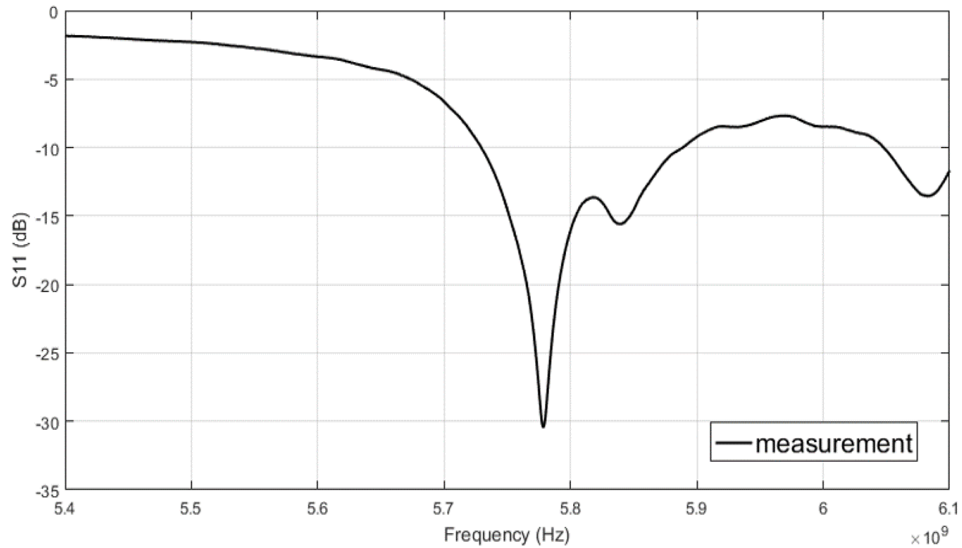
Figure 3.46. Return loss versus frequency characteristic of realized receiver antenna

antenna presented in Figure-3.46 and Figure-3.47 respectively, which were measured via vector network analyzer in the laboratory. Furthermore, realized gain calculated by three-antenna method, and radiation power patterns are performed in anechoic chamber, see Figure-3.48 and Figures-3.49-3.50.

Accordingly, bandwidth of the receiver antenna is obtained as ≈ 180 MHz and return loss can reach down to very low value ($-30dB$) at 5.8 GHz fallen within where operating frequency band proposed radar system can work. VSWR curve indicates which is demanded for the antenna design ≈ 1 in the operating frequency band.

As it was mentioned in the transmitter antenna section, measurements of realized receiver antenna radiation properties and characteristics are performed in the anechoic chamber and three-antennas method is used in order to measure gain of the receiver antenna. In Figure-3.48, the realized gain with respect to angle is depicted. This result belongs to horizontal polarization measurement of realized receiver. Gain polar pattern for both horizontal and vertical polarization results are given in Figure-3.49. Normalized radiated power pattern plots are given in Figure-3.50.

Highly directive behavior can be noticed in patterns of measurement for horizontal polarization though unwanted side lobes with very weak level occur. In the vertical measurement result, omni-directional pattern is observed, however the gain is very low and below than zero for all angles.

In order to analyze realized antenna results and simulated ones, comparison plots are given in Figures-3.51-3.55. In general, good agreements between simulation and mea-
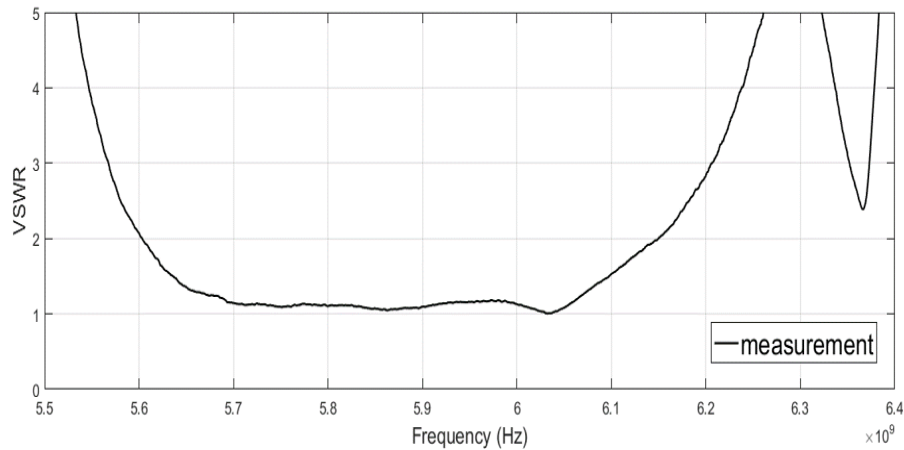
Figure 3.47. Measurement result of receiver VSWR

surements are achieved. Especially, the consistent variation in the return loss curves below -10dB is noticeable in Figure-3.46. An efficient resonance, which corresponds return loss lower than -30dB at operation frequencies 5.78-5.8 GHz. Additionally, radar can operate in 5.72-5.82 GHz and in 5.75 -5.85 GHz according to simulation and measurement, respectively.

As it is seen in Figure-3.53, radiation patterns of gain for horizontal and vertical polarization demonstrate the accordance of pattern form between simulation and measurement results, especially for horizontal one. Inconsistency for vertical result might be caused by low signal to noise ratio which can be influential when the very weak power is received during the measurement in anechoic chamber.

3dB beam-width and gain values are obtained as $(33°, 11.34dB)$ in simulation and $(\approx 32°, 11.33dB)$ in measurement. Normalized power radiation patterns for horizontal and vertical polarization of the realized receiver antenna are given in Figure-3.55. As it can be seen from this figure, the simulation and measurement results agrees more in horizontal polarization, when it is compared to the vertical one where the noise effect is more clearly seen in vertical polarization due to low received power.
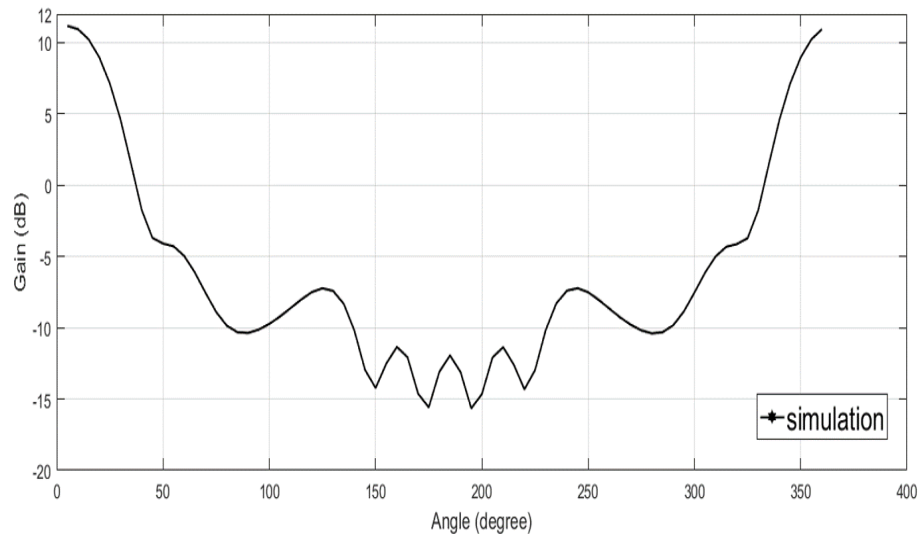
Figure 3.48. Measurement result of gain versus angle of receiver antenna

(a)

(b)
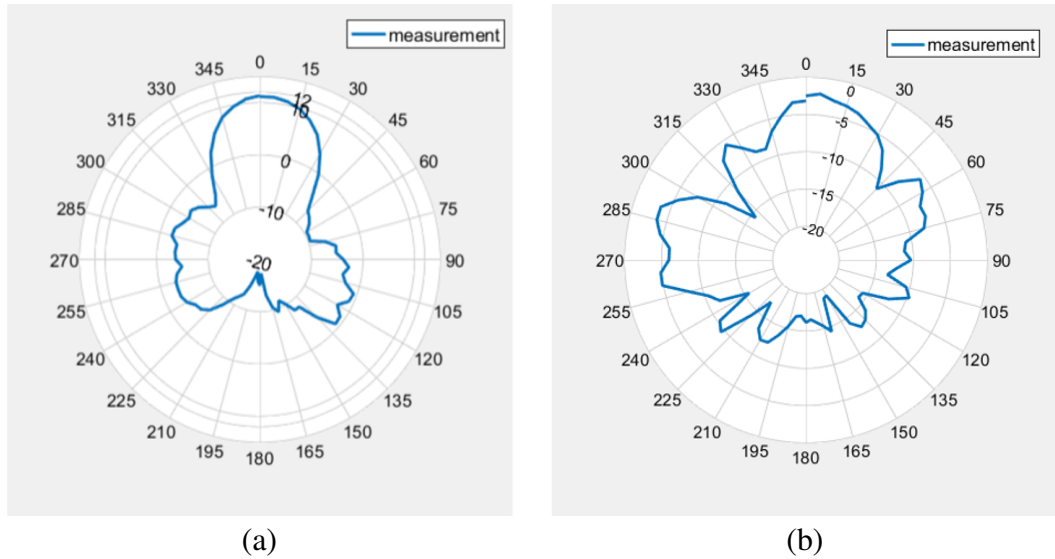
Figure 3.49. 5.8 GHz gain radiation pattern (a)Horizontal (b)Vertical
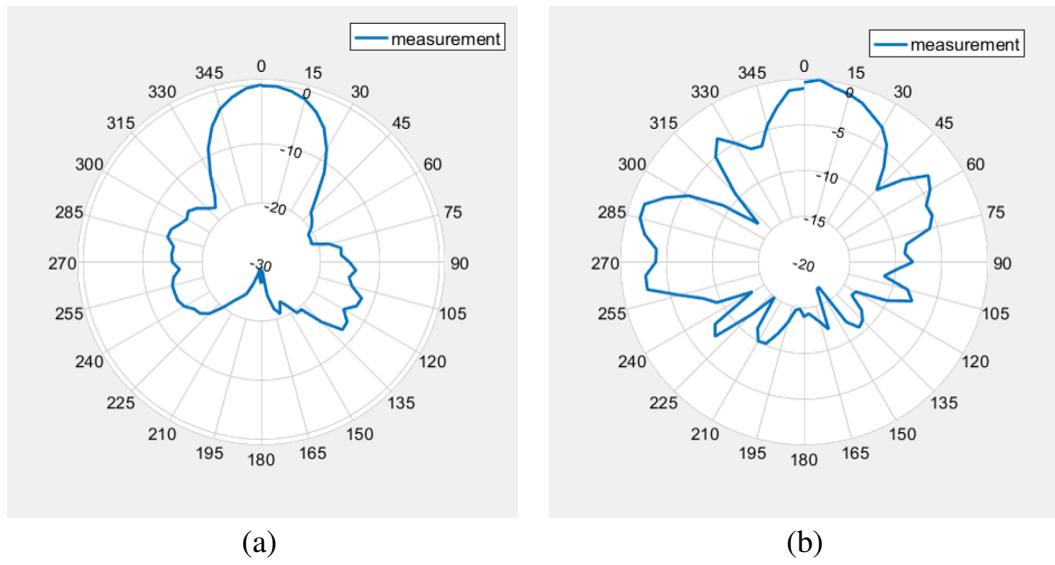
Figure 3.50. 5.8 GHz normalized radiation pattern (a)Horizontal (b)Vertical

Figure 3.51. Comparison of simulation and measurement return loss
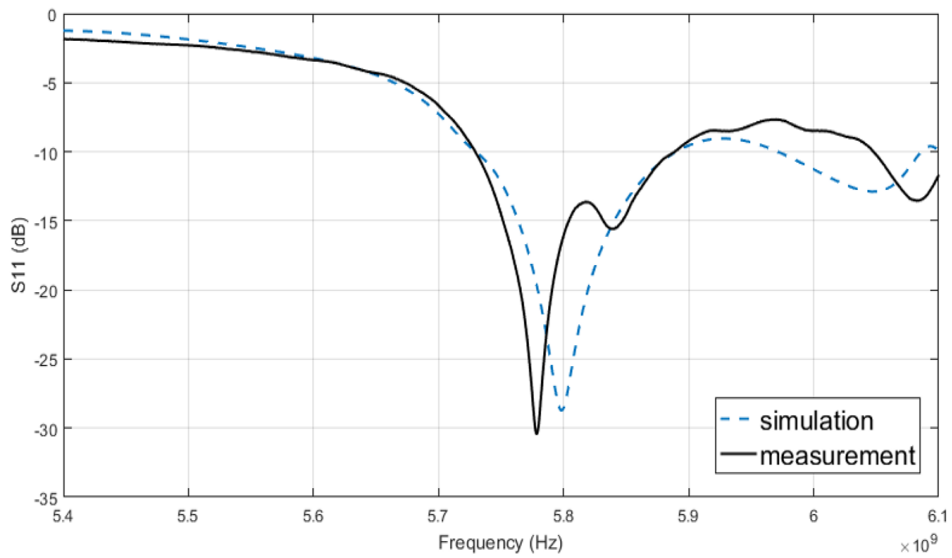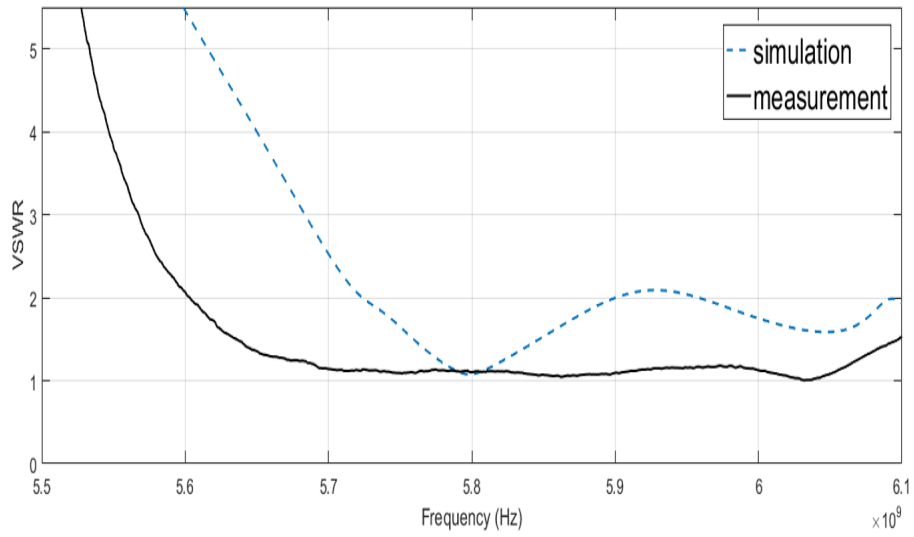
Figure 3.52. Comparision of measurement and simulation VSWR

<div align="center">(a)   (b)</div>
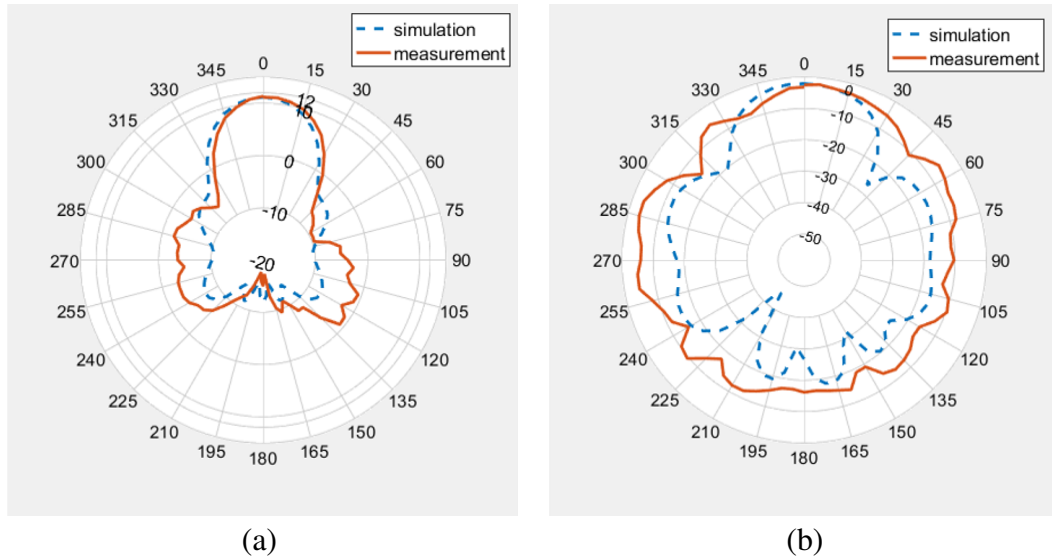
Figure 3.53. 5.8 GHz gain radiation pattern (a)Horizontal (b)Vertical
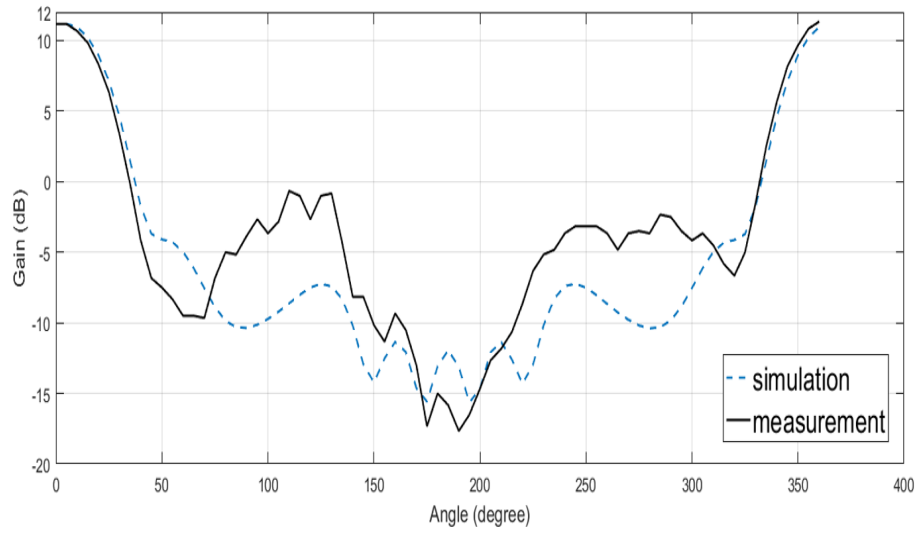
Figure 3.54. Comparison of simulation and measurement results of gain versus angle

(a)

(b)
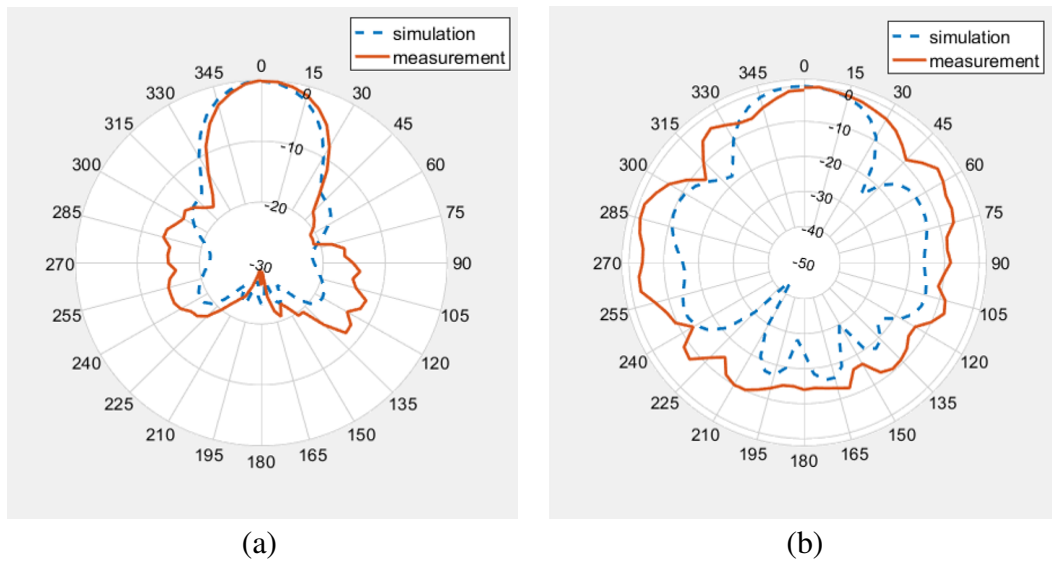
Figure 3.55. 5.8 GHz normalized radiation pattern (a)Horizontal (b)Vertical

CHAPTER 4

INTEGRATION OF THE METAMATERIAL ANTENNAS ON A SHORT-RANGE DOPPLER RADAR
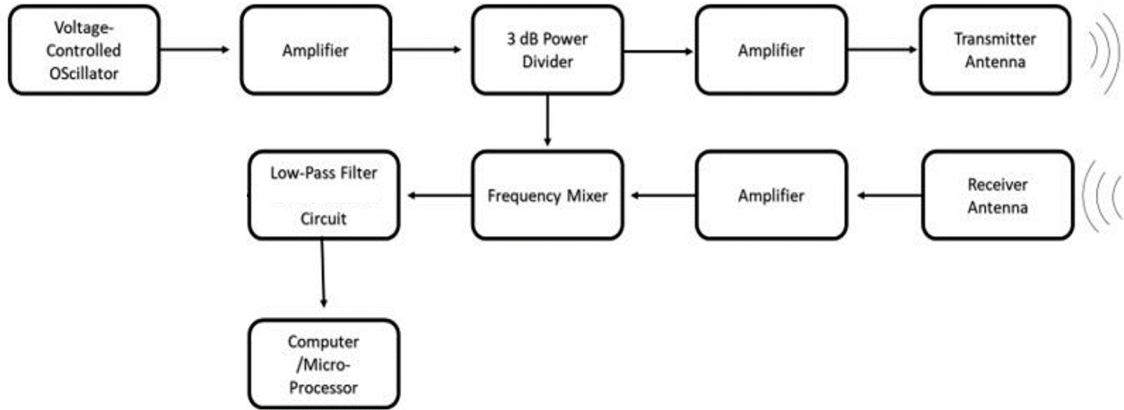
Figure 4.1. Block diagram of performed system design

In order to perform one of the main objective of this study, manufactured meta-material based transmitter and receiver antennas are integrated to the proposed short-range radar system. The block diagram of the radar is given in Figure-4.1.Given three-dimensional (3D) radiation patterns in Figure-3.10 and Figure-3.40, illustrate 3D far field power pattern of the transmitter and receiver antennas where the orientation of each antenna with respect to radiation pattern is expressed.Regarding pattern plots, mounting directions and polarization of the antennas on the radar can be easily determined. Moreover, types and product identification numbers of the SMA connecterized components such as voltage controlled oscillator (VCO), mixer, amplifiers and attenuators, which are products of Mini-Circuits Inc.. Measured and typical essential values are listed in Table-4.1. Those components and antennas are integrated according to the block diagram of the system and picture of realized system is given in Figure-4.2. The distance between antennas is found by empirically, which is $\approx 250 \ mm$. During the radar process, an amplified continuous wave (CW) is applied to the transmitter stage and to the mixer. The echo signal carries the Doppler shift is multiplied with the reference signal from the signal source in order to obtain only the frequency shifted portion of it. Afterwards, the resultant signal is filtered, amplified and processed via computer. The output is displayed using a radar interface

which is an open source code. (MIT:OpenCourseWare, 2011).

Table 4.1. Measured and typical values of components

Component	Typical Value(@5.8 GHz)	Measured value (@5.8 GHz)
VCO (ZX95-5776+)	2.23 dBm	2.35 dBm
Amplifier-1 (ZX60-83LN+)	20.58 dB	19.7 dB
Amplifier-2 (ZX60-83LN+)	20.58 dB	19.67 dB
Amplifier-3 (ZX60-24+)	24.2 dB	20.65 dB
Attenuator-1 (VAT-3+)	3.8 dB	3.51 dB
Attenuator-2 (VAT-3+)	3.8 dB	3.53 dB
Attenuator-3 (VAT-1+)	2.1 dB	1.48 dB
Wilkinson Power Divider-S21	-3.6 dB	-4.8 dB
Wilkinson Power Divider-S31	-3.6 dB	-4.6 dB
Mixer-Conversion Loss	5.85 dB	Not meas.
Mixer-Isolation	21.83 dB	Not meas.
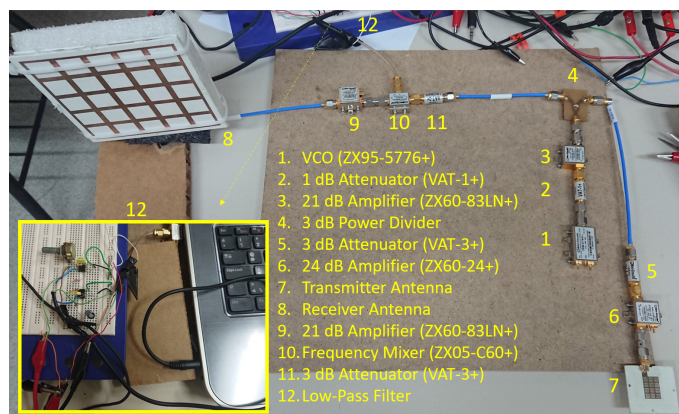
Figure 4.2. Short-range Doppler radar system with metamaterial antennas

Here it should be noted that a microstrip 3dB Wilkinson power divider is simulated and then realized for 5.8 GHz system operation. For the detailed information on the splitter design is given in references.(Pozar, 2012). Printed 3 dB Wilkinson power divider is measured at 5.8 GHz and results given in Table-4.1, are some lossy as expected, therefore second amplifier is used just before the transmitter antenna. Power delivered to transmitter is measured about to 20 dBm as expected due to saturation of solid-state amplifier. Design of Wilkinson power divider and simulation results of scattering characteristics are given in Figures-4.3-4.4, respectively. According to simulation results, return loss (S11) is very low along the entire band, as expected. S21 related with delivered power at port-2 and S31 for port-3, have same drawn curves and their value $\approx 3.6 dB$ at 5.8GHz.
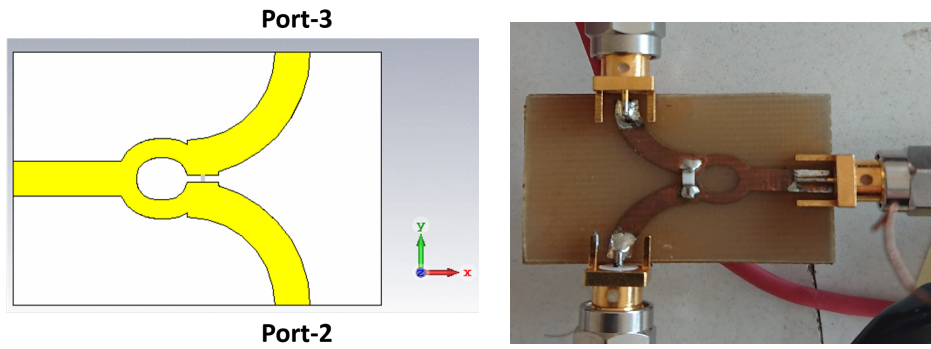
Figure 4.3. Designed (left) and realized (right) 3dB Wilkinson power divider
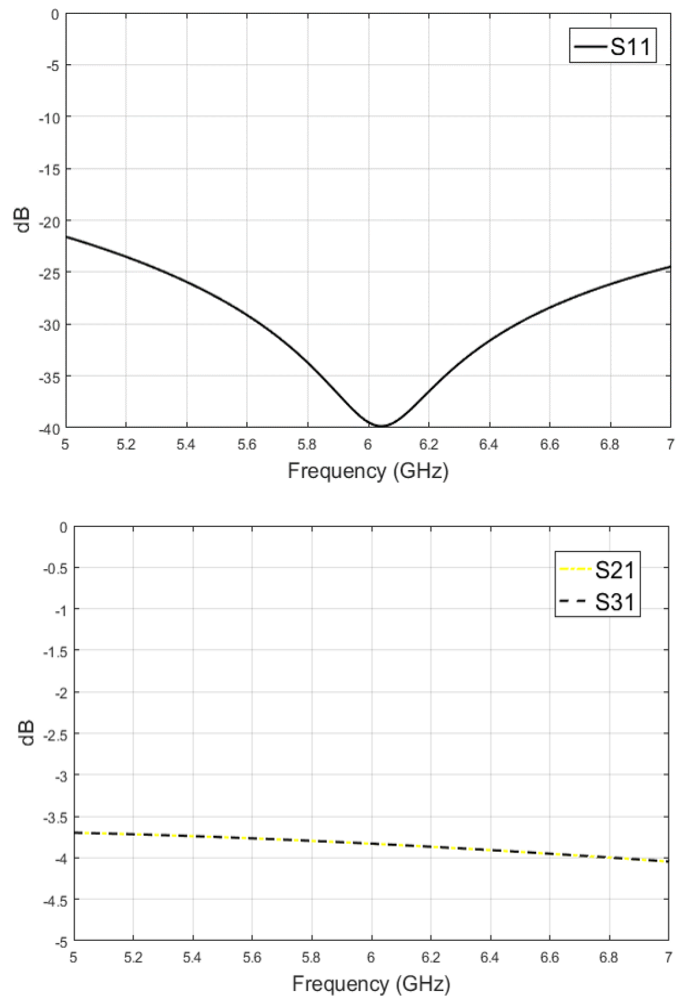
Figure 4.4. Simulation results for S-parameters of Wilkinson power divider

4.1. Measurement Results of the Doppler Radar

After the radar system is constructed, verification of velocity measurement and field experiments which are indoor/outdoor and through-wall are performed.

4.1.1. Verification of Velocity Measurement

Figure 4.5. The pendulum setup for velocity verification
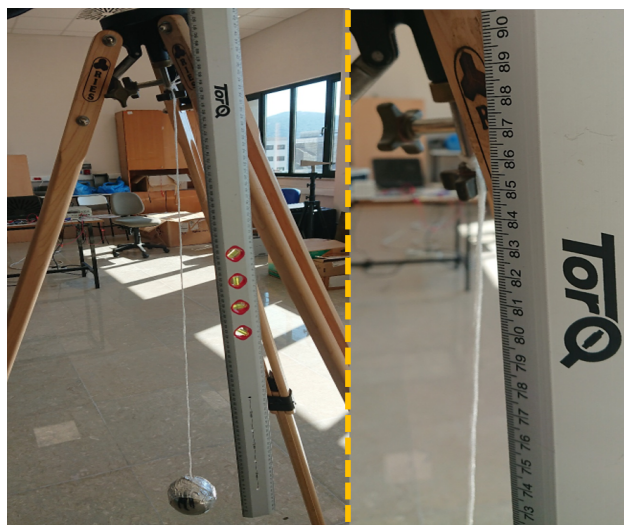
Figure 4.6. Measurement of height

In order to check verification of the Doppler performance, the pendulum with two different sized conducting spheres, is constructed as given in Figure-4.5. A regular conducting sphere ball is freed to fall free from the top then it starts accelerating and at the bottom where the rope is ended, its velocity vector becomes parallel to the antennas direction. Gravitational force causes oscillation on movement of ball with descending velocity. Neglecting the frictions, maximum velocity of the ball is calculated as,

$$v = \sqrt{2gh} \tag{4.1}$$

where v is the velocity of the ball , g is the gravitational acceleration and h is the falling height. In the experiment, falling height is adjusted as $85\ cm$ as given in Figure-4.6. The expected velocity is calculated as,

$$v = \sqrt{2 \times 9.81 \times 0.85} = 4.08\ m/s.$$
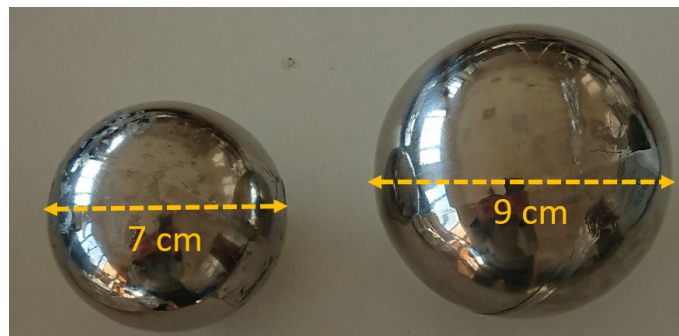
Figure 4.7. Two different size spheres which are used in pendulum performances

This experiment is performed with using two different size spheres which are given in Figure-4.7. The measured results are given in Figure-4.8 for smaller sphere and Figure-4.9 for larger one. In order to reach true maximum velocity, the experiment is repeated several times, since it is difficult to find exact free fall direction of balls which must be parallel to antenna directions. Accordingly, the same maximum speed for both ball is measured so that the air friction effects on balls are not observable during the experiment. It can be concluded that, the frictions are such weak that we can not detect the friction differences for two different size balls. The error is calculated as $\%1.68$. Additionally, in the results, pendulum oscillation with descending velocity can be noticeable.
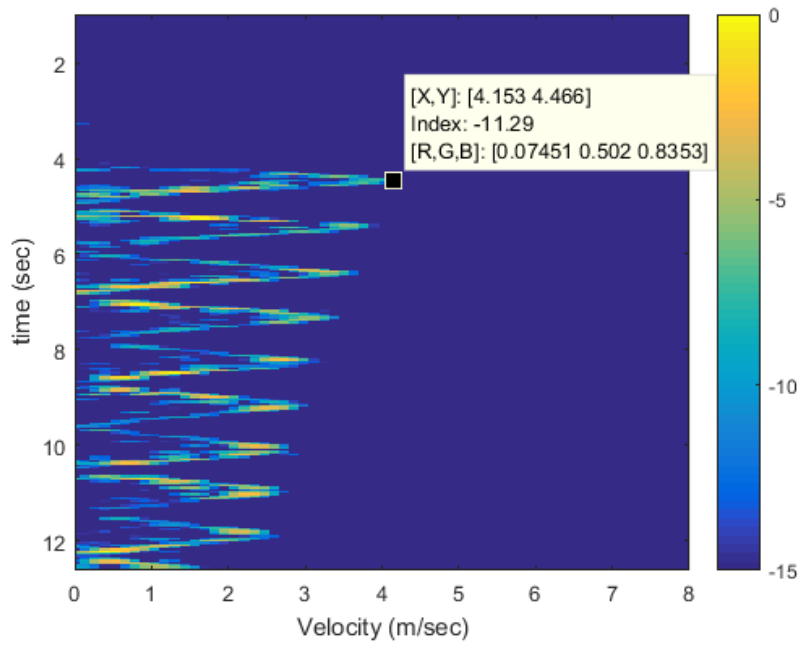
Figure 4.8. Velocity verification pendulum experiment-1 with smaller sphere
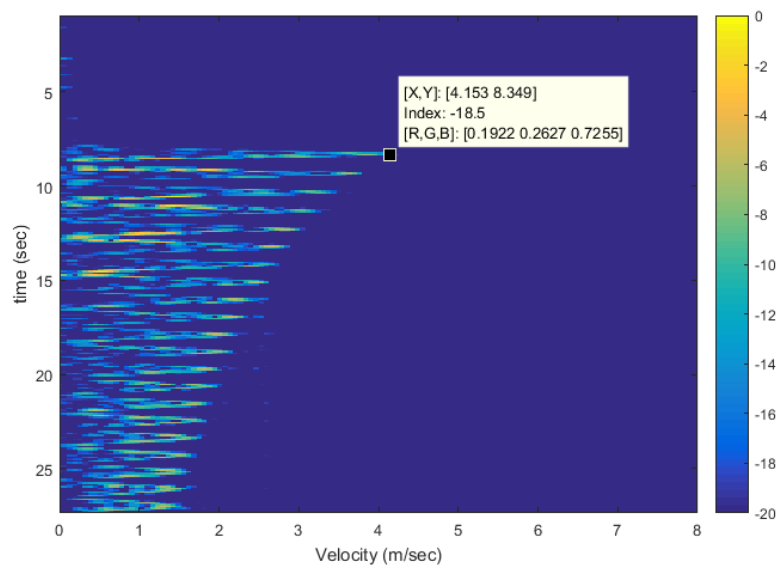
Figure 4.9. Velocity verification pendulum experiment-2 with larger sphere

4.1.2. Indoor Measurement

First experiment is performed indoor area. The measured velocity result of an average walking man in an indoor environment within the maximum radar range $\approx 15\ m$ is illustrated in Figure-4.10. The initial location of the target is $2\ m$ away from the system. Afterwards the man starts walking with constant acceleration and suddenly stops in a very short time, then waits ≈ 5 seconds again in the same way continues up to maximum distance. This scenario is repeated for reverse direction mean that this time a man starts walking from maximum distance up to front of radar system. Velocity of target in time can be followed in Figure-4.11 which proves the real movements of this scenario. Another indoor performance given in Figure-4.12, is taken from longer distance. This time, a man walks from radar position up to $25\ m$ with constant velocity, then he waits 10 seconds and he come back to the initial point. Measured ranges are consistent with the maximum range which is calculated according to Eq.-1.3, and it is approximately $\approx 30\ m$ when the radiated power is $20dBm\ (0.1W)$.

Figure 4.10. Experiment setup for indoor measurement

4.1.3. Through-Wall Measurement

The second experiment is devoted to through-wall operation hence the system is placed $4\ m$ far from an ordinary concrete wall. The same target, starts to walk with random speeds within 5 meters up to 10 distance to the system while the measurements are being taken, illustrated in Figure-4.14.
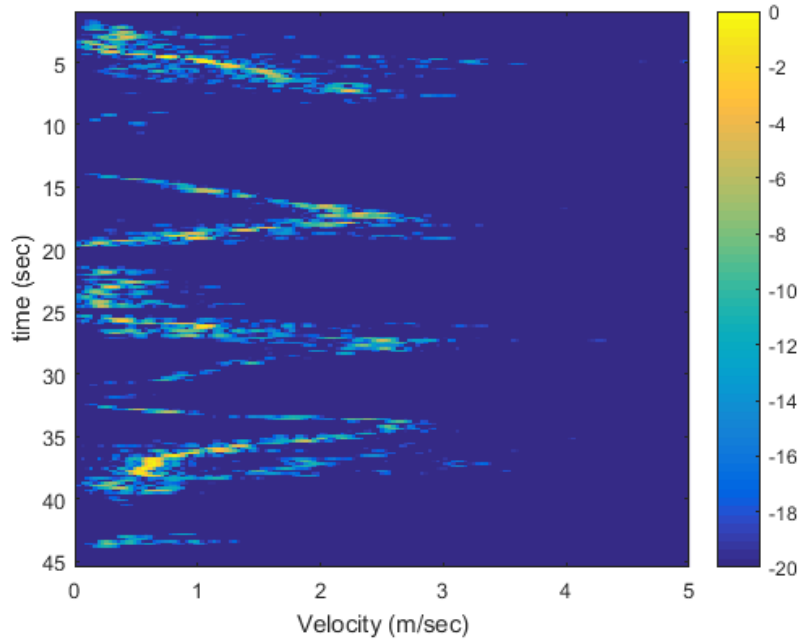
Figure 4.11. First Doppler measurement data of a walking man for velocity (m/s) and received signal amplitude(colorbar in dB) during an indoor experiment

For second through-wall performance is recorded against to another inside building wall, and this time, radar system is placed $4\ m$ away from the wall and maximum target distance to the system is about to $6\ m$ meters. Again a man starts running, then he stops suddenly and waits for 5 seconds. Afterwards, again he come back to behind the wall with running and this whole scenario is repeated multiple times which can be seen in Figure-4.15.

Thicker outer building wall compared to previous one, is used for third through-wall measurement. Likewise, a man starts running with increasing acceleration from maximum distance of 5 meters to 3 meters where is behind of the wall. This action is repeated multiple times with some standby time, which is clearly observable in Figure-4.16. When second result is compared to third one, increased wall thickness causes more attenuation on radiated wave so that some unclarity and roughness due to weak received wave, exist on third result.
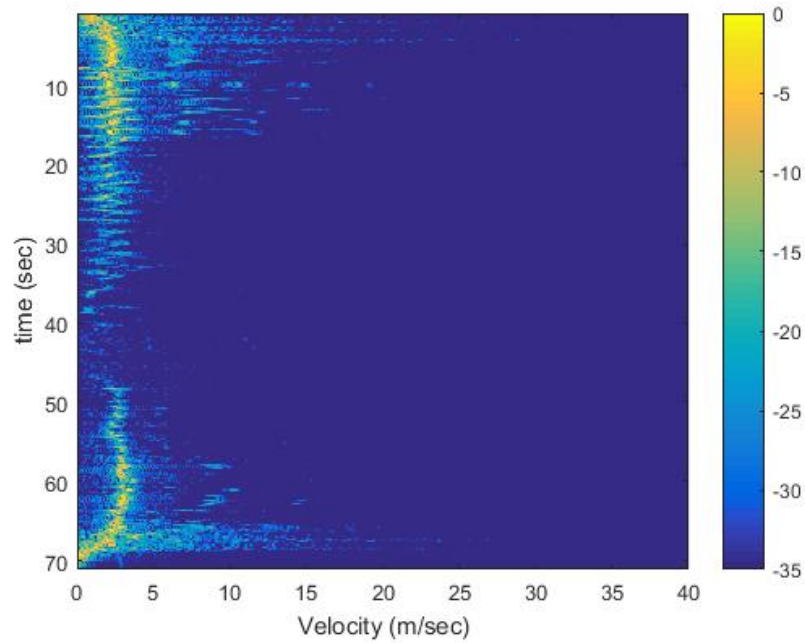
Figure 4.12. Second Doppler measurement data of a walking man for velocity(m/s) and
received signal amplitude(colorbar in dB) during an indoor experiment

4.1.4. Outdoor Measurement

In order to measure outdoor performance of the radar, system is placed against to the car direction in the field given in right side of Figure-4.17. For the first performance, the car seen in figure, initially waits stable at distance $> 100\ m$ to the system and road extends straight along the direction of antennas. First, it starts accelerating up until 34 km/h observed on display panel of the car, then it goes some distance with that velocity, and after it suddenly starts slowing down and finally stops at 2 meters front of the system.
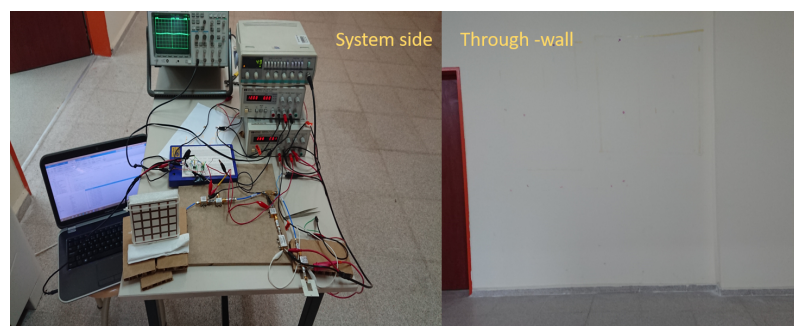
Figure 4.13. Experiment setup for through-wall measurement
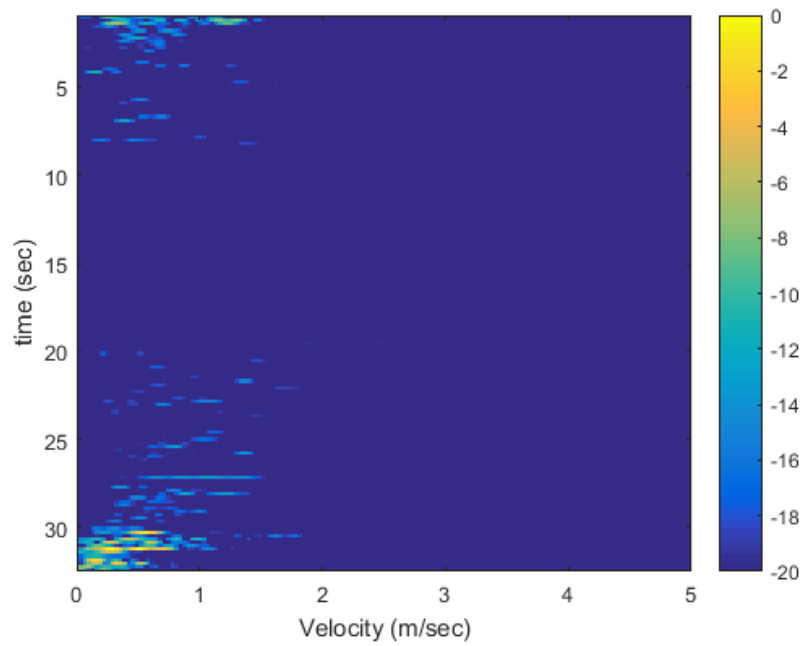
Figure 4.14. First Doppler measurement data of a walking man for velocity(m/s) and received signal amplitude(colorbar in dB) during a through wall experiment
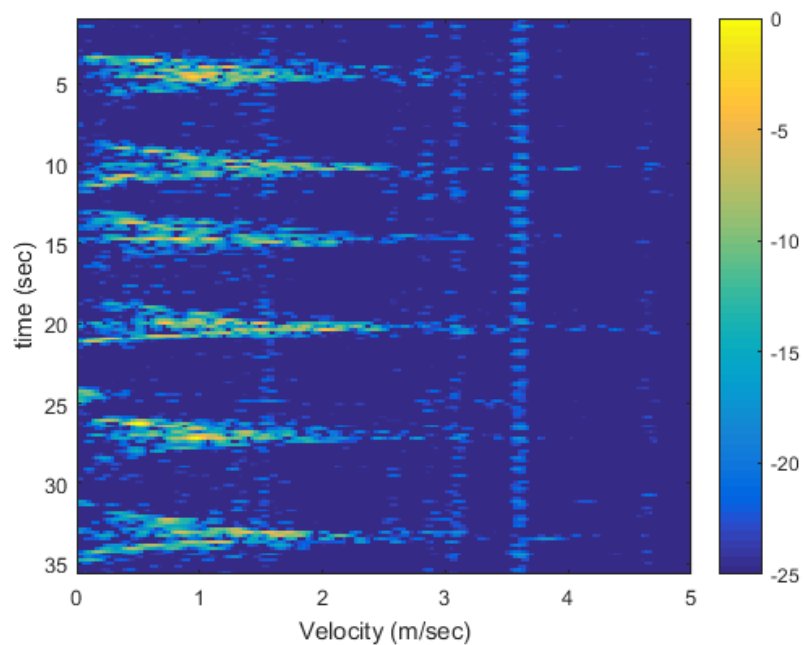
Figure 4.15. Second Doppler measurement data of a walking man for velocity(m/s) and received signal amplitude (colorbar in dB) during a through wall experiment
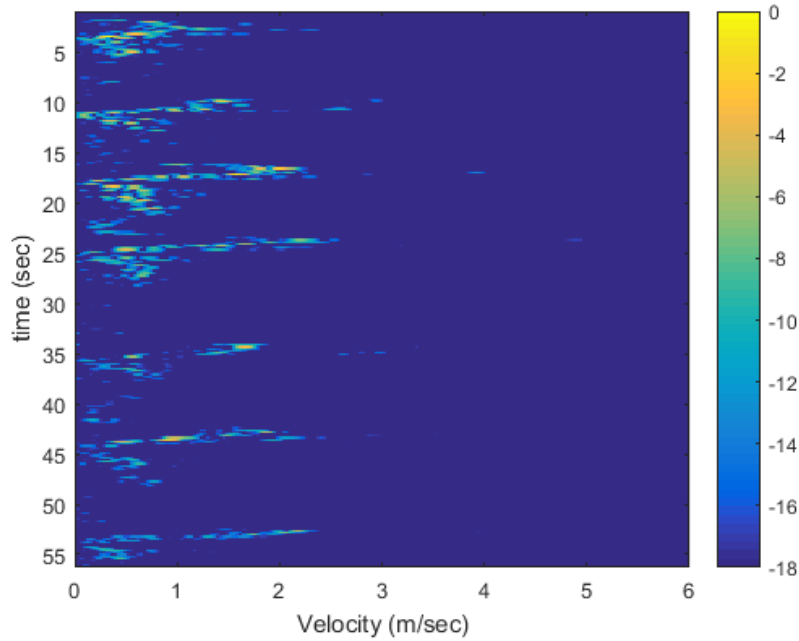
Figure 4.16. Third Doppler measurement data of a walking man for velocity(m/s) and received signal amplitude (colorbar in dB) during a through wall experiment

Figure-4.18 clearly shows this action. Maximum velocity read in result is 32 km/h (9 m/s) and regarding some delay effects and miss-match due to VCO tolerances, it agrees with the value which is seen in car display panel. According to time-velocity curve, maximum distance is calculated as $\approx 65\ m$.

Second outdoor measurement was recorded for same action, whereas this time car speeds up to $45\ km/h$. The result is given in Figure-4.18. Maximum velocity is observed in result as 42 km/h (11.71 m/sec) while 44 km/h on car display. As mentioned above, this difference might be occurred due to mismatch about frequency tolerance of VCO and some delays during the processing of circuit and computer. Accordingly, maximum distance is calculated as $72.5\ m$.

For third outdoor measurement, this time system is placed perpendicularly to the road so that velocity vector of car is not in the same direction with antenna orientation. As expected, the velocity can not be detected by radar as noticed in Figure-4.20, while the car passing by. Afterwards, for fourth experiment, system is rotated by $45°$ towards to car direction so that velocity vector now has some effects on Doppler measurement as seen in Figure-4.21. For last two measurements, car velocity is approximately around 20 km/h while the passing by front of the system.
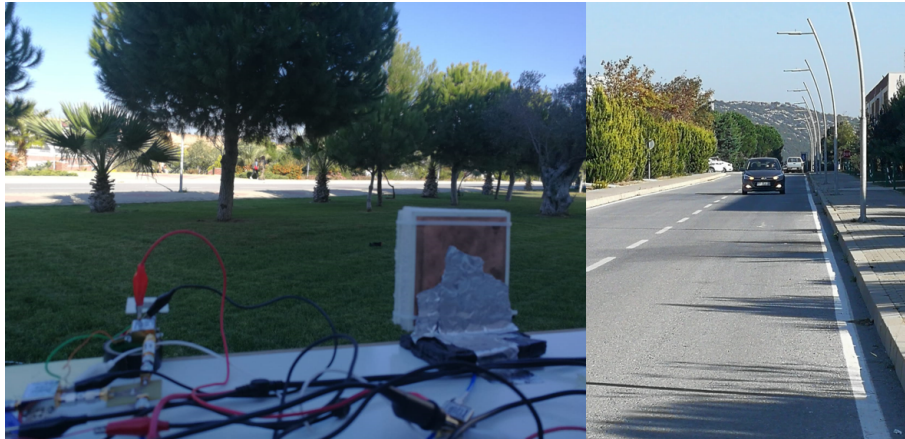
Figure 4.17. Experiment setup for outdoor measurement
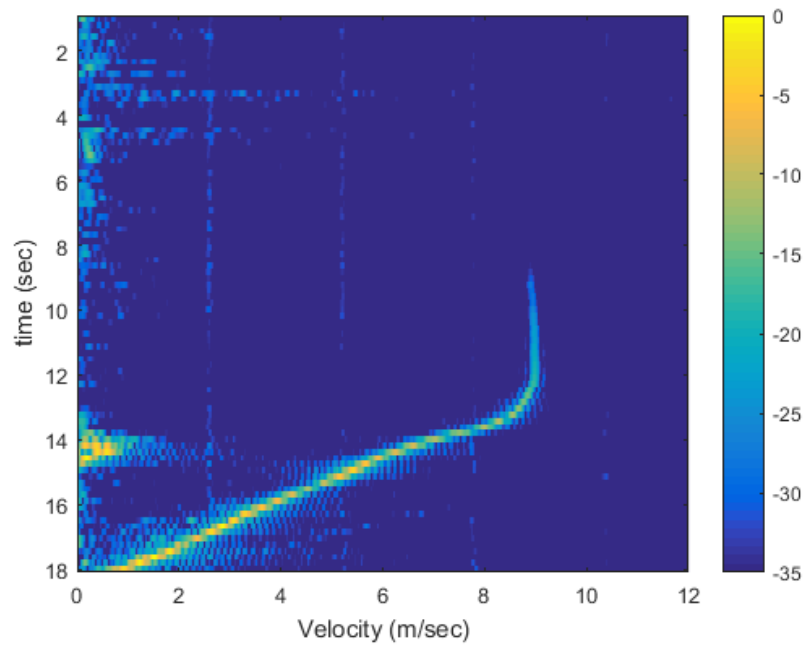
Figure 4.18. First Doppler measurement data of a car for velocity(m/s) and received signal amplitude(colorbar in dB) during a outdoor experiment
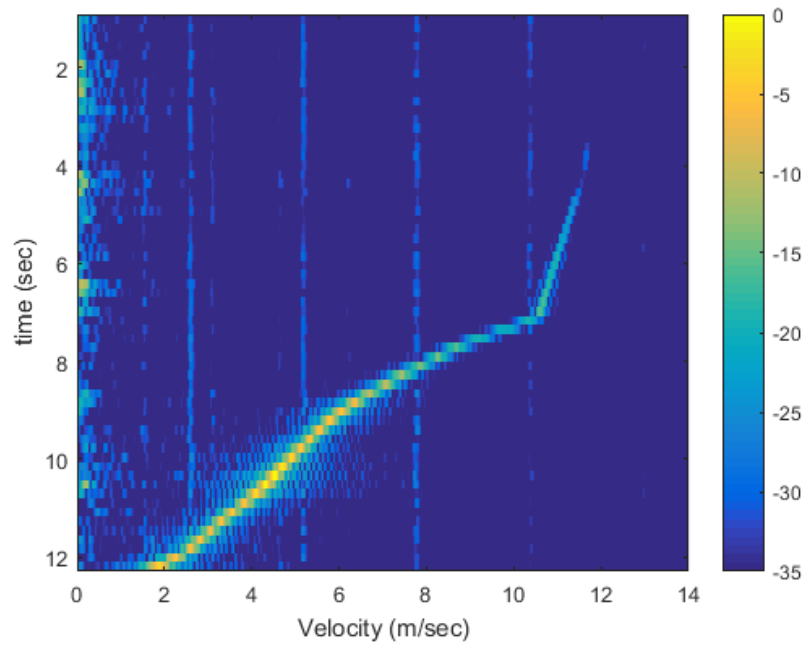
Figure 4.19. Second Doppler measurement data of a car for velocity (m/s) and received signal amplitude(colorbar in dB) during a outdoor experiment
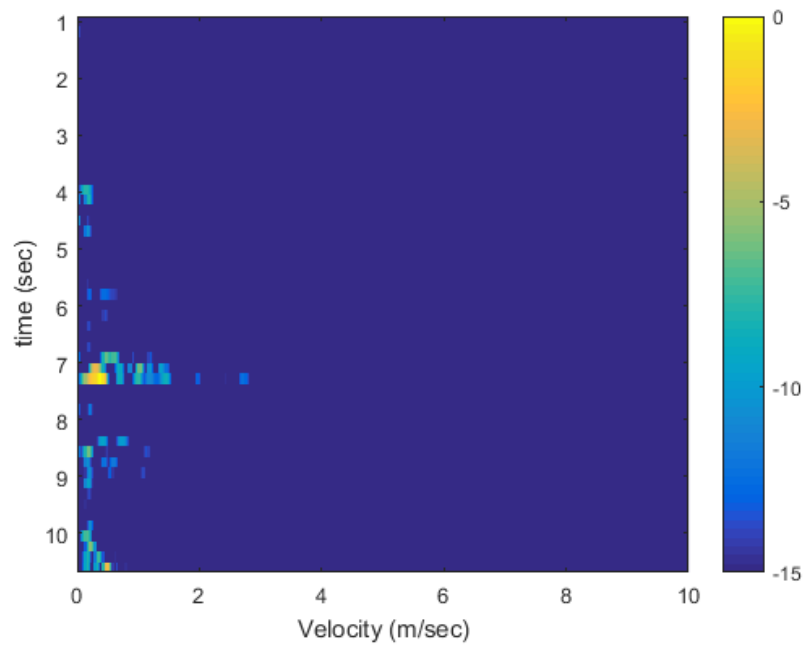
Figure 4.20. Third Doppler measurement data of a car for velocity (m/s) and received signal amplitude(colorbar in dB) during a outdoor experiment
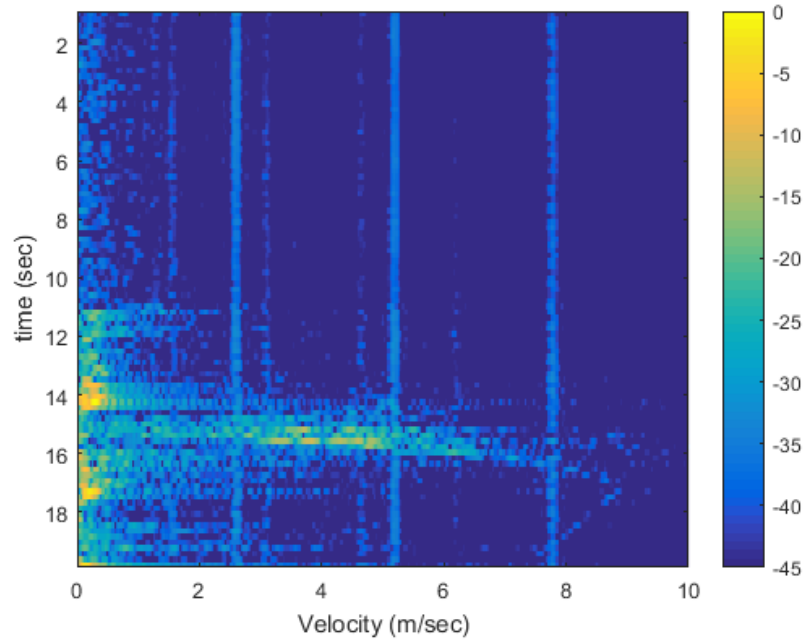
Figure 4.21. Fourth Doppler measurement data of a car for velocity (m/s) and received signal amplitude(colorbar in dB) during a outdoor experiment

Fifth measurement for outdoor scenario is performed in field as given in Figure-4.22 and recorded result is given in Figure-4.23. The scenario is occurred such that same car starts coming back by reverse gear up from front of the system up to maximum distance($35 \ m$) of the field. Then it waits for a 5 seconds and again goes through the system with high acceleration and suddenly stops at near of the system. During this performance, velocity of car can reach up to 20 km/h.

Indoor and through-wall performances present some noise and multiple velocities at the same time when comparing to outdoor results especially for result of car used as a target. Reasons might be multiple reflections and multiple moving parts of human body. Using a car as target also demonstrates accuracy and validity of the system due to the consistency between car display panel and result indicators.

Figure 4.22. Experiment setup and outdoor performance field
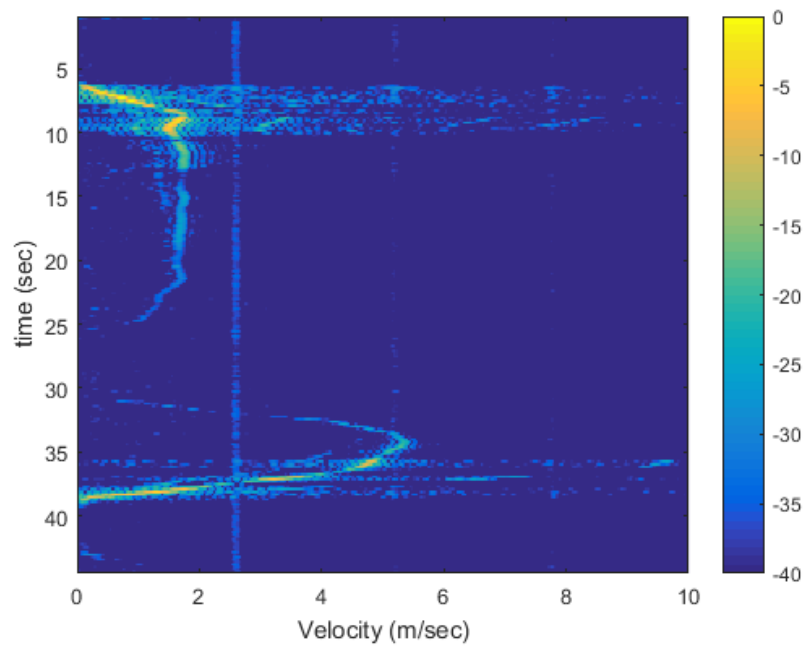
Figure 4.23. Fifth Doppler measurement data of a car for velocity(m/s) and received signal amplitude(colorbar in dB) during a outdoor experiment

CHAPTER 5

CONCLUSIONS

In the last decade, metamaterial concept is intensively investigated both from theoretical and practical point of views. Many applied studies which include meta structures showing unnatural properties, are presented and results have been discussed by physicists and engineers. In this thesis, practicality and the efficiency of metamaterial based transmitter and receiver antennas in microwave spectrum, are tested on a short range Doppler radar system due to their unique and advantageous properties. A compact radar system can give an opportunity to understand and investigate metamaterial theory and applications since antenna performances are very crucial. Result of the study yields that metamaterial antennas improve the radar characteristics via size reduction, lightweight and range. Measurement results are presented for indoor and outdoor Doppler radar experiment, transmitter and receiver vertical/horizontal radiation patterns and return losses.

Transmitter antenna basically is a microstrip patch antenna which consists of periodically aligned complementary split ring resonators (CSRRs) on the top patch part and partial grounds created by etching cross-strip lines on the bottom. This engineered medium shows a double negative index properties. According to measurement results, gain of the transmitter is 6.5dB at 5.8 GHz and it resonates at a large bandwidth which simplifies the impedance matching. Realized antenna results can be accepted to consistent with simulation for 5.8 GHz. The receiver antenna supported by near-zero epsilon metamaterial structures have gain 11.3 dB at the operating frequency as the same as the gain obtained from simulation. Consequently, metamaterial based antennas are offered to employ for radar applications since both structures designed for transmitter and receiver have unique properties which can provide for acquiring a large gain with smaller sizes as compared to a classical microstrip patch antenna. It is also successfully demonstrated the consistency between simulation and measurement results for such complex and small structures which could assure a confidence for novel antenna designs to the researchers. On the other hand, metamaterial, novel research field interested mostly in last decade gives us enthusiasm to understand and investigate for future.

According to results of field performances, it is observed that the applicability of the metamaterial based antenna concept in a Doppler radar. For such small and low powered radar system, relatively large radar range could be obtained due to efficient and

high gain characteristic of the antennas. Moreover, narrow half power beam-width of the receiver antenna can led to detect angular position of the target in more accuracy. Angular scanning of the field might be considered and it helps to confine the target in certain area. Firstly, simple pendulum system verifies the accuracy of the velocity results with $\%1.68$ error. Additionally, results of through-wall performances demonstrated that the proposed system can be employed for detection of moving targets behind the different concrete walls. In another radar performances which are performed on outdoor environment gives us a clear view about upper limits of the radar system. Herewith, typical car used as a target demonstrated how radar cross-section effects on radar performance, especially in term of maximum radar range which can reach to $\approx 72.5\ m$. When the proposed system is compared to the similar studies such as given in (Teng, 2013), the consistent and matching results are obtained, however their system is more bulky due to the usage of volumetric coffee can antennas. For future study, electronically angular scanning on the receiver side while the improving radar software are considered. Additionally, higher frequencies can led to more compact system with high resolution and accuracy.

REFERENCES

Ali, A. and Z. Hu (2008). Metamaterial resonator based wave propagation notch for ultrawideband filter applications. *IEEE Antennas and Wireless Prop. Letters 7*.

Amir Ebrahimi, Withawat Withayachumnankul, S. A.-S. and D. Abbott (May 2014). High-sensitivity metamaterial-inspired sensor for microfluidic dielectric characterization. *IEEE Sensors Journal 14*(5).

Baena, J. D. and et al. (April 2005). Equivalent-circuit models for split-ring resonators and complemantary split-ring resonators coupled to planar transmission lines. *IEEE Transactions on Microwave Theory and Techniques 53*.

Balanis, C. A. (2005). *Antenna Theory Analysis and Design* (3rd ed.). John Wiley & Sons, Inc.

Charvat, G. L. (2014). *Small and Short-Range Radar Systems* (1st ed.). Taylor and Francis Group CRC Press.

Cheng, D. K. (1983). *Field and Wave Electromagnetics* (1st ed.). Addison-Wesley Publishing Company.

D. R. Smith, Willie. J. Padilla, D. C. V. N.-N. and S. Schultz (May 2000). Composite medium with simultaneously negative permeability and permittivity. *Pyhsical Review Letters 84*(18).

Davide Ramaccia, Francesco Scattone, F. B. and A. T. Daly (June 2013). Broadband compact horn antennas by using eps-enz metamaterial lens. *IEEE Transactions on Antennas and Propagation 61*(6).

Doviak, R. J. and D. S. Zrnic (1993). *Doppler Radar and Weather Observations* (2nd ed.). Elsevier Inc, Academic Press.

D.Schuring, J.J.Mock, B. S. J. A. and D.R.Smith (October 2006). Metamaterial electromagnetic cloak at microwave frequencies. *Science Express*.

Erentok, A. and R. W. Ziolkowski (March 2008). Metamaterial-inspired efficient electrically small antennas. *IEEE Transcations on Antennas and Propagation 56*.

Falcone, F. and et al. (November 2004). Babinet principle applied to design of metasurfaces and metamaterials. *Physical Review Letters 93*(19).

Floyd, T. L. (2012). *Electronic Devices* (9th ed.). Pearson.

George V. Eleftheriades, A. K. I. and P. C. Kremer (December 2002). Planar negative refractive index media using periodically l-c loaded transmission lines. *IEEE Transactions on Microwave Theory and Techniques 50*(12).

Hosseini, S. M. A. T. and H. Amindavar (2017). A new ka-band doppler radar in robust and precise cardiopulmonary remote sensing. *IEEE Trans. on Inst. and Meas. 66*.

J. B. Pendry, A. J Holden, D. J. R. and J. Stewart (November 1999). Magnetism from conductors and enhanced nonlinear phenomena. *IEEE Transactions on Microwave Theory and Techniques 47*.

J. B. Pendry, A. J. Holden, W. J. S. and I. Youngs (1996). Extremely low frequency plasmons in metallic mesostructures. *Pyhsical Review Letters 76*.

Jenn, D. (accessed in October 2018). Lecturer notes: Radar fundamentals. *nps.navy.mil/faculty/jenn, Naval Postgraduate School*.

Karaaslan, M. (2009). *Negatif Kırılma indisli Meta-malzemeleri Elde Edilmesi*. Çukurova Üniversitesi.

Le-Wei Li, Ya-Nan Li, T.-S. Y. J. R. M. and O. J. F. Martin (April 2010). A broadband and high-gain metamaterial microstrip antenna. *Applied Physics Letters 96*.

Lijuan Su, Jordi Naqui, J. M.-C. and F. Martin (2016). Modeling and applications of metamaterial transmission lines loaded with pairs of coupled complementary split-ring resonators (csrrs). *IEEE Antennas and Wireless Prop. Letters 15*.

Mali, A. (2012). *X Band Uygulamaları için Metamateryeller ile Anten Parametresi*

iyileştirilmesi. Süleyman Demirel Üniversitesi.

Merih Palandoken, A. G. and H. Henke (February 2009). Broadband microstrip antenna with left-handed metamaterials. *IEEE Transcations on Antennas and Propagation 57*.

MIT:OpenCourseWare, . (2011). Mit : Build a small radar system capable of sensing range, doppler, and synthetic aperture radar imaging.

Munoz-Ferreras, J.-M. and et al. (2016). Short-range doppler-radar signatures from industrial wind turbines: Theory, simulations, and measurements. *IEEE Trans. on Inst. and Meas. 65*.

Nader Engheta, R. W. Z. (2006). *Metamaterials Physics and Engineering Explorations* (1st ed.). John Wiley & Sons, Inc.

Önder Yılmaz, H. and F. Yaman (2018a). Meta-material antenna design for 5.8 ghz doppler radar. *IEEE Trans. on Instrumentation and Measurement under review*.

Önder Yılmaz, H. and F. Yaman (2018b). Meta-material antenna design for 5.8 ghz doppler radar. *Book of Abstracts,Turkish Pyhsical Society 34(th) International Pyhsics Congress 113*.

Pasakawee, S. (2012). *Left-handed Metamaterials Realized by Complementary Split-ring Resonators for RF and Microwave Circuit Applications , PHD Thesis*. The University of Manchester.

pasternack.com (accessed in October 2018). Microstrip line and patch antenna images. *pasternack.com*.

Pendry, J. B. (October 2000). Negative refraction makes a perfect lens. *Physical Review Letters 85*(18).

Pozar, D. M. (2012). *Microwave Engineering* (4rd ed.). John Wiley & Sons, Inc.

radartutorial.eu (accessed in October 2018). Angular beam-width resolution image. *radartutorial.eu*.

R.Garg, P.Bhartia, I. and A.Ittipiboon (2001). *Microstrip Antenna Design Handbook* (1st ed.). Artech House INC.

Ricardo Marques, F. M. and M. Sorolla (2008). *Metamaterials with Negative Parameters* (1st ed.). John Wiley & Sons, Inc.

Schwartz, B. T. and R. Piestun (December 2003). Total external reflection from metamaterials with ultralow refractive index. *J. Opt. Soc. Am. B/20*.

Shanyue Guan, Jennifer A. Rice, C. L. and C. Gu (2014). Automated dc offset calibration strategy for structural health monitoring based on portable cw radar sensor. *IEEE Trans. on Inst. and Meas. 63*.

Sondaş, A. (2011). *Metamateryal Altyapılı ve Halka Yüklemeli Mikroşerit Anten Tasarımları ve Gerçeklenmesi*. Kocaeli Üniversitesi.

spectrum.ieee.org (accessed in October 2018). Radar on autonomus car image. *spectrum.ieee.org*.

Stefan Enoch, Gerard Tayeb, P. S. N. G. and P. Vincent (November 2002). A metamaterial for directive emission. *Pyhsical Review Letters 89*(21).

Sungjoon Lim, C. C. and T. Itoh (January 2005). Metamaterial-based electronically controlled transmission-line structure as a novel leaky-wave antenna with tunable radiation angle and beamwidth. *IEEE Transcations on Microwave Theory and Techniques 53*.

Teng, K. C.-M. (2013). *The Design and Evaluation of a 5.8 GHz LaptopBased Radar System, MS Thesis*. Purdue University.

thedrive.com (accessed in October 2018). Through-wall radar application image. *thedrive.com*.

theteamasterix.wordpress.com (accessed in October 2018). Radar classification according to applied waveform image. *theteamasterix.wordpress.com*.

Turpin, J. P. and et al. (December 2012). Low cost and broadband dual-polarization

metamaterial lens for directivity enhancement. *IEEE Transactions on Antennas and Propagation 60*.

Veselago, V. G. (1968). The electrodynamics of substances with simulatenously negative values of ϵ and μ. *Soviet Physics Uspekhi 10*.

Watson, R. C. (2009). *Radar Origins Worldwide: History of Its Evolution in 13 Nations Through World War II* (1st ed.). Trafford Publishing.

Withayachumnankul, W. and D. Abbott (August 2009). Metamaterials in the terahertz regime. *IEEE Photonics Journal 1*(2).

Yahong Liu, Xiaojing Guo, S. G. and X. Zhao (2013). Zero index metamaterial for designing high-gain patch antenna. *International Journal of Antennas and Propagation, 215681*.

Yang, F. and Y. Rahmat-Samii (2009). *Electromagnetic Band Gap Structures in Antenna Engineering* (1st ed.). Cambridge University Press.

Zhao, Y. and Y. Su (2018). Cyclostationary phase analysis on micro-doppler parameters for radar-based small uavs detection. *IEEE Trans. on Inst. and Meas. 67*.

Zhu, J. and G. V. Eleftheriades (2009). A compact transmission-line metamaterial antenna with extended bandwidth. *IEEE Antennas and Wireless Propagation Letters 8*.

Ziolkowski, R. W. and E. Heyman (October 2001). Wave propagation in media having negative permittivity and permeability. *PHYSICAL REVIEW E, 64*.